OPTICAL, MECHANICAL, AND DETECTOR DEVELOPMENTS FOR THE PRIME-CAM 850 GHZ MODULE

by

ANTHONY I. HUBER
Bachelor of Science, Physics, University of Lethbridge, 2019
Master of Science, Physics, University of Lethbridge, 2021

A Dissertation Submitted in Partial Fulfillment of the
Requirements for the Degree of

DOCTOR OF PHILOSOPHY

in the Department of Physics and Astronomy

University of Victoria

We acknowledge and respect the Lək̓ʷəŋən (Songhees and Esquimalt) Peoples on whose territory the university stands, and the Lək̓ʷəŋən and W̱SÁNEĆ Peoples whose historical relationships with the land continue to this day.

OPTICAL, MECHANICAL, AND DETECTOR DEVELOPMENTS FOR THE PRIME-CAM 850 GHZ MODULE

BY

ANTHONY I. HUBER
Bachelor of Science, Physics, University of Lethbridge, 2019
Master of Science, Physics, University of Lethbridge, 2021

Supervisory Committee

Dr. Scott C. Chapman, Dissertation Supervisor
Department of Physics and Astronomy, University of Victoria

Dr. Justin Albert, Departmental Member
Department of Physics and Astronomy, University of Victoria

Dr. Michael L. McGuire, Outside Member
Department of Electrical and Computer Engineering, University of Victoria

Abstract

Prime-Cam is a first-generation instrument designed for the Fred Young Submillimeter Telescope (FYST) in the Cerro Chajnantor Atacama Telescope (CCAT) Facility, which will be sited on Cerro Chajnantor in the Chilean Atacama Desert at an elevation of 5600 m. Among the instrument modules being developed for the Prime-Cam receiver, the 850 GHz module will probe the highest frequency and presents unique challenges in optical design, coupling, detection, and readout. The 850 GHz module is of particular importance to the astronomical community due to the absence of near-future proposals for instruments at similar wavelengths and at equivalent sites. This work describes the parameter space of the 850 GHz optical system between the Fλ spacing, beam size, pixel sensitivity, and detector count. The optimization of an optical design for the 850 GHz instrument module for CCAT-prime is also presented.

Success of the 850 GHz module hinges on the development of state-of-the-art, photon-noise-limited kinetic inductance detector (KID) arrays which will facilitate quality single-frequency, dual-polarization measurements in the given atmospheric windows. The 850 GHz module will consist of approximately 45,000 titanium-nitride, polarization-sensitive, lumped-element kinetic inductance detectors, meaning the module will field more microwave kinetic inductance detectors than any other millimeter-wave receiver to date. We present the critical aspects of the detector design and discuss solutions to the challenges of efficient optical coupling and a multi-octave readout band. The detectors are being designed to be read out using a multi-octave readout architecture, allowing for approximately double the multiplexing of other Prime-Cam modules. The parameter space in the development of these detectors is explored, including testing a means of shorting inductors to modify the resonance with minimal changes to the absorber architecture and testing different volumes of the inductor. Results and optical characterization of the prototype pixels for the 850 GHz instrument module are presented. The results of this work will directly inform the design of microwave KIDs for the multi-octave readout architecture as part of the development of densely packed arrays for the Prime-Cam instrument. The 850 GHz module is expected to be observing in 2026.

Also included is a report on a blind, millimeter-wave redshift survey of the brightest, unlensed submillimetre galaxies from the SCUBA-2 Cosmology Legacy Survey. The 14 brightest submillimetre galaxies (S_{850} >11 mJy) identified as single sources by the SMA were selected from the Lockman Hole, AEGIS, and CDF-N fields. 12 of these 14 sources were observed using the IRAM NOEMA interferometer, where at least one strong emission line was detected in each galaxy. Redshifts are assigned to each of the observed galaxies, unambiguously in five cases with two or more detected lines, and guided by photometric redshifts for the seven single line cases. The luminosities and widths of the CO lines, as well as the flux density, are used to probe the properties of these hyper-luminous infrared galaxies. The extreme nature of these galaxies is then contrasted with the results of previous surveys.

Table of Contents

Supervisory Committee ii

Abstract iii

Table of Contents v

List of Tables viii

List of Figures ix

Acknowledgments xii

Dedication xiv

1 Introduction 1
- 1.1 Far-infrared and Submillimeter Astronomy . . . 1
- 1.2 The Fred Young Submillimeter Telescope . . . 4
  - 1.2.1 Prime-Cam . . . 5
- 1.3 Kinetic Inductance Detectors . . . 6
- 1.4 A Blind Survey of Bright Submillimeter Galaxies . . . 7
- 1.5 Dissertation Overview . . . 8

2 Prime-Cam: The 850 GHz Module 9
- 2.1 Introduction . . . 10
- 2.2 Requirements and Constraints . . . 11
- 2.3 Optical Design and Analysis . . . 16
  - 2.3.1 Aberration Theory . . . 17
  - 2.3.2 Simons Observatory Instrument Module Design . . . 19
  - 2.3.3 Finalized 850 GHz Module . . . 20
  - 2.3.4 Module Systematics . . . 28
- 2.4 Integration and Testing . . . 28
- 2.5 Conclusion . . . 29

3 Microwave Kinetic Inductance Detectors 30
- 3.1 Introduction . . . 30
- 3.2 Superconductivity . . . 31
  - 3.2.1 Charge Carrier Density . . . 32
  - 3.2.2 Surface Conductivity . . . 34
  - 3.2.3 Superconducting Resonators . . . 39
- 3.3 Microwave Kinetic Inductance Detector Theory . . . 42
  - 3.3.1 Thermal Properties . . . 43

3.3.2 Optical Responsivity . . . 45
3.3.3 Sensitivity . . . 47
3.4 Conclusion . . . 51

4 A Cryogenic Testbed for MKIDs 52
4.1 Cryogenic Facility . . . 52
4.2 Prototype Test Box . . . 54
4.2.1 Specifications . . . 54
4.2.2 Feedhorn Block . . . 55
4.2.3 Assembly . . . 60
4.3 RF Chain Design . . . 62
4.3.1 Scattering Parameters . . . 63
4.3.2 Characterization and Noise . . . 64
4.3.3 Cascaded Noise Temperature . . . 67
4.3.4 Prime-Cam 850 GHz Module . . . 69
4.4 Readout . . . 72
4.4.1 Firmware Procedure . . . 73
4.5 Conclusion . . . 75

5 Design and Characterization of Prototype 850 GHz MKIDs 76
5.1 Introduction . . . 77
5.2 Kinetic Inductance Detector Design . . . 78
5.2.1 Resonator Design . . . 78
5.2.2 Shorting Inductor Lines . . . 80
5.2.3 Array Design . . . 81
5.3 Preliminary Results from a MKID Test Array . . . 83
5.3.1 Dark Testing . . . 84
5.4 850 GHz Prototype MKIDs . . . 85
5.5 Prototype MKID Characterization . . . 86
5.5.1 Experimental Setup . . . 87
5.5.2 Two-Octave Prototype Array . . . 91
5.5.3 Experimental Responsivity . . . 92
5.5.4 Noise Analysis . . . 96
5.5.5 Discussion . . . 98
5.6 Conclusion . . . 103

6 A Blind ^{12}CO Redshift Survey of Bright Submillimeter Galaxies 104
6.1 Introduction . . . 104
6.1.1 The NOEMA Interferometer . . . 106
6.1.2 The Submillimeter Array . . . 107
6.2 Observations . . . 107
6.2.1 NOEMA Observations . . . 107
6.2.2 SMA observations . . . 109
6.3 Redshift Determination . . . 109
6.4 Results . . . 113
6.5 Gas dynamics . . . 118
6.6 Redshift Distribution . . . 119
6.7 Conclusion . . . 123

7 Conclusion **124**
7.1 Dissertation Summary 124
7.1.1 Optical Design 125
7.1.2 Detector Design 126
7.1.3 Shorting Inductor Lines 127
7.1.4 Survey of Bright Submillimeter Galaxies 128
7.2 Future Directions 129
7.3 Conclusion 130

Bibliography **132**

List of Tables

2.1 Values for the power coupling constant of the 850 GHz module across a representative sample of possible maximum tilt angles. 15
2.2 General tolerances with noted exceptions for position, decenter, and tilt for the optical design. 28

4.1 Comparison of predicted thermal loading for RF chain components in the 850 GHz module compared with the overall thermal budget at each stage based on preliminary values for Prime-Cam. 71

5.1 Frequency plan of the 850 GHz array based on the two IDC finger sizes and either shorted or non-shorted inductors 83
5.2 Detector parameters for the eleven pixels included in the witness chips. 86

6.1 Observation details and derived metrics for each of the sources in the fields 108
6.2 Parameters derived from the lines measured for each of the sources 115
6.3 Median redshift and measured gradient of the relation between 850 μm flux densities and redshift for each of the fields 118
6.4 Simulation results of the measured gradient of the relation between S_{850} and redshift for each of the fields 121

List of Figures

1.1 Opacity of the atmosphere across the electromagnetic spectrum. 2
1.2 Test assembly of the Fred Young Submillimeter Telescope 4
1.3 Comparison of band coverage between Prime-Cam and Herschel-SPIRE across increasing redshift galactic continua 6

2.1 Rendering of Prime-Cam highlighting the modular nature of the instrument. 11
2.2 Simulations of the Strehl ratio across variations in the field curvature represented by the maximum allowable tilt. 14
2.3 Angle of incidence of the chief ray across the radius of the focal plane. The system was optimized to have a maximum angle of incidence less than 3°. 15
2.4 Shapes of the Seidal aberrations compared against a perfect reference wavefront. . 19
2.5 Optical design and simulated Strehl ratio across the FoV for the baseline SO design. 20
2.6 Mapping speed as a function of detector count across varying optical designs. . . . 21
2.7 Ray trace model of the four-lens design of the 850 GHz module for Prime-Cam and simulation of the Strehl ratio across the FoV. 22
2.8 Cutaway model of the Prime-Cam 850 GHz module depicting the four lens design. 22
2.9 Ray trace of a three-lens equivalent to the four-lens design with greater edge thickness to effectively combine lenses three and four. 23
2.10 Position, decenter, and tilt tolerancing for the four-lens, 850 GHz optical design generated using the inverse increment technique. 25
2.11 Best and worst Strehl ratios on the image plane as found for a single trial using 1000 Monte Carlo simulations. 26
2.12 Histogram of the mean Strehl ratio across the image plane for a single trial using 1,000 Monte Carlo simulations. 27

3.1 Measurement of resistance as a function of temperature for TiN around the critical temperature. 32
3.2 Model of the frequency-dependence of the surface impedance of a superconducting thin film made of titanium nitride. 38
3.3 Circuit diagram of a kinetic inductance detector. 40
3.4 Circuit diagram demonstrating an array of lumped element kinetic inductance detectors. 41
3.5 Sample resonance shape with asymmetry. The resonator was simulated using empirical results from the BLAST-TNG experiment for an 850 GHz LEKID. 42
3.6 Theoretical magnitude of the shift in resonance frequency as a function of temperature for a TiN MKID in parts per million. 45
3.7 Theoretical magnitude of the shift in resonance frequency as a function of absorbed optical power for a TiN MKID in parts per million. 47
3.8 Simulated NEP as a function of the absorbed power for total NEP and individual noise sources. 51

4.1 Cryogenic stages of the Bluefors LD250 cryostat. 53
4.2 Rendering of the aluminum feedhorn block for the test box. 56
4.3 Line impedance as a function of air gap for two widths of microstrip lines. 58
4.4 Simulated S-Parameters for the test box feedhorns. 59
4.5 Simulated S-Parameters for the test box feedhorns with an offset in the absorber line. 60
4.6 Rendering of the assembled test box including coaxial flanges. 61
4.7 Final machined test box assembly. 62
4.8 Schematic of the RF chain design for the 850 GHz module as it is to be incorporated into the cryogenic testbed. 63
4.9 Simulated S-parameters through the 850 GHz cryogenic testbed, including two detector resonances. 64
4.10 High-level diagram of a proposed cryogenic TRL test configuration for measuring S-parameters of RF components. 65
4.11 Simulated equivalent noise temperature across the detector array readout bandwidth from the cryogenically cooled MKID array to the output of the room-temperature amplifier. 68
4.12 Prototype flexline for the 850 GHz module by CryoElec. 71
4.13 First light results in the cryogenic test facility showing a multi-detector sweep on a sample detector package using the RFSoC design. 74

5.1 Design of a prototype 850 GHz pixel consisting of two orthogonal kinetic inductance detectors 79
5.2 Sample inductor design for for two polarization-sensitive kinetic inductance detectors with sample designs of non-shorted and shorted inductor lines 80
5.3 Simulations of the absorption efficiency for MKIDs which are either shorted or unshorted 82
5.4 Schematic of an 850 GHz witness chip 84
5.5 Sample results of a TiN prototype kinetic inductance detector probing thermal responsivity 85
5.6 A fabricated witness chip and 144-pixel two-octave array prototype 87
5.7 Setup of a two-octave test array and dark test of a prototype chip 88
5.8 Transmission band of the test box setup and the incident optical power based on blackbody temperature 89
5.9 Setup for optical tests inside the NIST LDR 90
5.10 Misalignment of feedhorn block holes with the detectors 91
5.11 VNA sweep of a two octave array using the shorted inductor technique 91
5.12 Measured Q_i and T_c of the TiN prototype arrays. 93
5.13 Measured thermal response in frequency and Q_i. 94
5.14 Optical response for the high-volume prototype resonator 95
5.15 Q_i as a function of input power for loading levels expected for the 850 GHz module 95
5.16 Power spectral density as a function of optical loading with low-frequency noise slopes. 96
5.17 NEP with increasing optical loading for different volumes of resonator 99
5.18 White noise equivalent power as a function of incident power for the high volume resonator showing the fitted optical efficiency 100
5.19 VNA sweep of a two octave array emphasizing the parasitic resonances 101
5.20 Measured Q_i based on the different grounding plane materials 102

6.1 The NOEMA and SMA interferometers . . . 106
6.2 Sample multi-wave cutout of one of the sources: CDFN-1 . . . 109
6.3 Spectral scans and zoomed in lines of lowest transition of CO detected in the spectral scans for Lockman sources . . . 110
6.4 Spectral scans and zoomed in lines of lowest transition of CO detected in the spectral scans for CDF-N sources . . . 111
6.5 Spectral scans and zoomed in lines of lowest transition of CO detected in the spectral scans for AEGIS sources . . . 112
6.6 Quantized redshift possibilities and their probabilities for the seven sources with only one line detection . . . 113
6.7 CO FHWM as a function of $L'_{CO}(1-0)$ . . . 116
6.8 Median redshift of each of the sources as a function of their 850 μm flux densities distinguished by field. . . . 117
6.9 Sample fields used for a simulation . . . 120
6.10 Median redshift of each source as a function of S_{850} distinguished by fields across four different simulations . . . 121
6.11 Median redshift of each source as a function of S_{850} for all potential simulated sources 122

7.1 VNA sweep of a two octave array using the shorted inductor technique . . . 127

Acknowledgments

First, I would like to thank my supervisor, Professor Scott Chapman, for his unceasing support and encouragement for myself and my family. We have undergone a fair share of struggles, and you have advocated for me doing what I need to take care of my family. You are truly a great educator and inspire me to share my knowledge and love of learning with those around me.

I would like to thank Professor Locke Spencer for sponsoring me to stay in Lethbridge. Your generosity allowed my wife to be near her mother during the precious little time they had before Alzheimer's claimed her mind. For that we are forever grateful. You have been a good friend and mentor far beyond what would be expected from a professor. You have advised me on my classes, experiments, academic writing, and raising a family as a student. Thank you for everything you have done for me these last seven years.

I would like to thank Adrian Sinclair, James Burgoyne, and Matt Xie, my teammates throughout my doctoral degree. You have supported my many efforts in designing and testing detectors with your readout hardware and software. You were also incredibly patient in answering my many software questions. I would also like to thank Matt in particular for his help in organizing the CAD files and preparing the assembly procedure for the module. We were also supported by many co-op students, and I thank them for their support as well. I would also like to thank my collaborators at Cornell University, the University of Chicago, and Simon Fraser University for their time, resources, and aid as I have navigated my way through my degree. I would like to especially thank the mm-lab group at the NRC-HAA for the aid, supplies, training, and support as we have set up up our lab. In particular I would like to thank Doug Henke, who was a vocal advocate of our efforts and a staunch supporter and idea generator.

I would like to thank my parents, Curtis and Susan Huber, and my parents-in-law, Roger and Joanne Jensen, for keeping me motivated, supporting me, and pretending to be interested whenever I talked about physics. Thank you to my numerous siblings and siblings-in-law, as well as my horde of nieces and nephews.

Thank you to Soren, my first born, whose passion for learning rivals my own. I love your creativity and enthusiasm, and you are an example of the best kind of learner. You have always been supportive of my studies, even when we moved away from your friends. You have been a constant study partner, gym bro, and hunting buddy. Thank you for being both my son and my friend.

Thank you to Reuben, my second born, the most creative and loving person I know. I love that you never hesitate to do anything you can to make people laugh. There is nothing that brightens my days more than your laughs. I love your ability to make new best friends wherever you go. You have been my biggest cheerleader and supporter in everything I do. Thank you for being such an amazing son, supporter, and artist.

Thank you to Nox, my third born, and living proof that there can never be too much chaos in your life. I love your passion and determination in doing everything your own way, of being unafraid to try something even if your plans may fail. You are an amazing problem solver and mischief maker who somehow always knows where I hide my treats and how to get them. You are also sweeter than a cherub and an absolute daddy's boy. Thank you for being my son and playmate.

Lastly, and most importantly, I owe everything to my beautiful wife, Tessa. From the moment seven years ago that I decided to go back to school you have supported me and never faltered. We have had more than our fair share of struggles, but you have always exuded great personal strength, patience, and a bit of stubbornness. None of this would have been possible without you. Thank you for being my companion through life.

Dedication

To Soren, Reuben, and Nox

I can bare all the weight of the world with you on my shoulders.

To Tessa

You're are the reason for me, that I can do this consistently.

Chapter 1

Introduction

I will travel the distance in your eyes
Interstellar light years from you
Supernova; we'll fuse when we collide
Awaking in the light of all the stars aligned

Telescope

STARSET

This chapter briefly explores the justification of the Prime-Cam 850 GHz module for the Fred Young Submillimeter Telescope. An introduction to far-infrared/submillimeter astronomy is presented together with some challenges faced by making observations in this wavelength range. Meeting these challenges requires careful consideration and execution of the optical and mechanical design of the module. This requires the development of state-of-the-art kinetic inductance detectors with never-before-seen pixel densities in the far-infrared/submillimeter regime. Included in this is the development of a technique to produce two-octave kinetic inductance detectors. Lastly, a blind survey of bright submillimeter galaxies is introduced.

1.1 Far-infrared and Submillimeter Astronomy

Far-infrared (FIR) astronomy plays a crucial role in our understanding of the Universe due to the fact that roughly half of all radiation incident from the Universe is observed on Earth within the FIR and submillimeter wavelength range[1] (30 - 1000 μm). This is the result of two mechanisms: the Universe is full of cool dust and gas clouds which absorb radiation with a shorter wavelength and re-radiate at longer wavelengths (i.e., as infrared radiation), which is able to pass through the interstellar medium without being absorbed, and the accelerating expansion of the Universe results in a redshift in the emitted radiation from the distant Universe such that shorter wavelength radia-

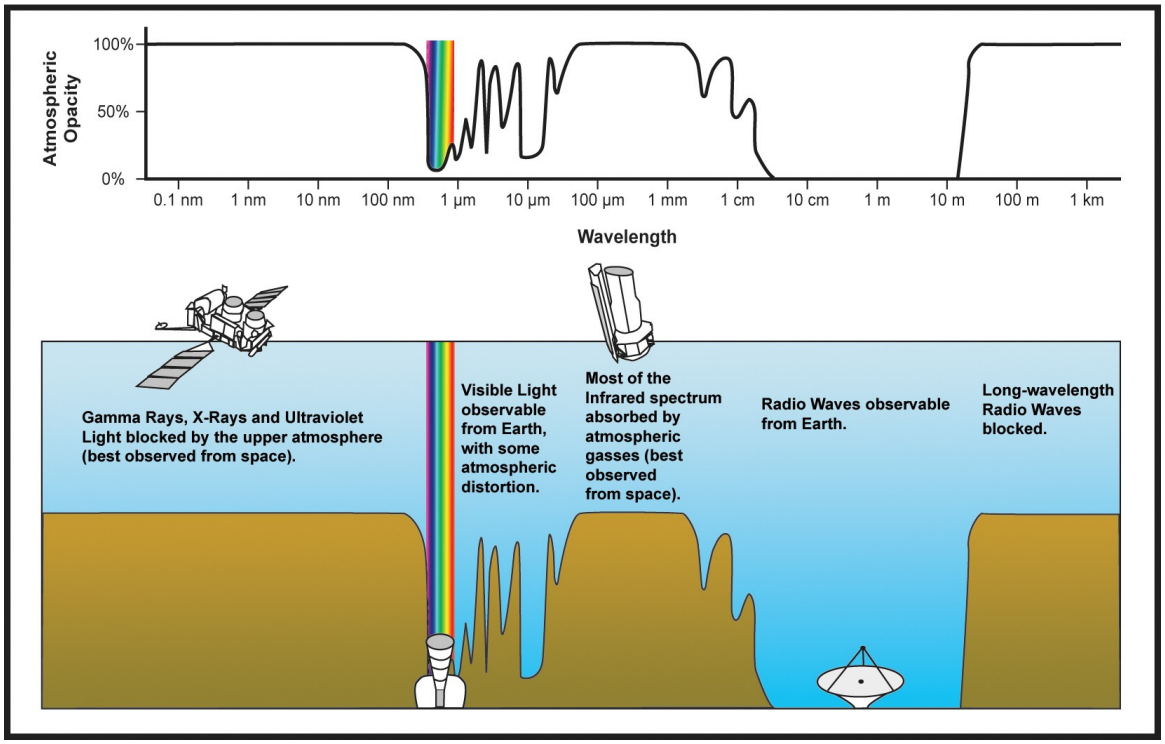

Figure 1.1: Opacity of the atmosphere across the electromagnetic spectrum. Visible light is represented by the rainbow. Note that with few exceptions the Earth's atmosphere is opaque to far-infrared and submillimeter radiation.[6]

tion is shifted to longer wavelengths.[2] In the decadal plans of both the National Aeronautics and Space Administration (NASA) and the European Space Agency (ESA), a series of questions was put forth.[3,4] This series includes questions such as: What are the conditions for planet formation and the emergence of light? How does the Solar System work and how did we get here? How does the Universe work and what is it made of? FIR observations are well suited to address each of these questions as they provide powerful diagnostics and are highly complementary to other types of observations.[5]

In astronomy there are two general forms of spectral features: continua and lines. A spectrum is formed from any combination of these features, which may be observed as either emission or absorption. Continua are features associated with condensed matter or synchrotron radiation which are observed over a broad range of wavelengths, thus the spectra appear smooth and continuous.[7] On the other hand, spectral lines arise from gas (molecular, atomic, or ionic) which experiences a change in its net configurational energy (rotational, vibrational, or electronic) from one energy state to another, ΔE.[7] This change in energy corresponds to a particular frequency of light, $\Delta E = h\nu$,

where h is Planck's constant The net energy of a system increases when radiation is absorbed, and decreases when radiation is emitted. The energy levels of a given atom or molecule are unique to that entity, and transition between them can be used to identify their existence in an astronomical source. For example, emission lines in a molecular cloud reveal the cloud's composition and can provide further information, such as the temperature, pressure, and velocity of particles in the cloud. These features are commonly used to characterize star-forming regions.[7]

Continuum features arise when the interaction of a large number of particles spread out the discrete emission lines such that they are no longer distinguishable. In general, continuum features are observed in warm dust and dense gas clouds, which emit blackbody radiation. Such clouds are generally warmed through collisional excitation or absorption of short wavelength radiation, and radiation is then emitted as the particles cool. The intensity per unit wavelength, B_λ, is defined by the Planck distribution:[8]

$$B_\lambda(\lambda, T) = \frac{2hc^2}{\lambda^5} \frac{10^{-6}}{e^{hc/\lambda k_B T} - 1}, \tag{1.1}$$

where k_B is Boltzmann's constant, and T is the absolute temperature. The wavelength of the peak emission, λ_{peak}, is defined by the Wien displacement law, which is given as

$$\lambda_{peak} = \frac{b}{T}, \tag{1.2}$$

where b is Wiens's displacement constant (2898 μm K).

Understanding these features of a spectrum, the questions put forward in the decadal survey may be addressed through FIR and submillimeter observations as they provide powerful diagnostics and are highly complementary to other types of observations.[5] To this end, the Cerro Chajnantor Atacama Telescope (CCAT) Observatory was organized with the following goals::[9]

- Explore the process and large scale structure of both re-ionization and the galaxy assembly process during the epoch of re-ionization.
- Understand the process of galaxy assembly and track the evolving structure of the Universe from the epoch of re-ionization to Cosmic Noon.
- Constrain models of cosmic inflation by decoupling CMB B-mode emissions from foreground emissions.

Figure 1.2: Test assembly of the Fred Young Submillimeter Telescope (FYST). FYST will be cited on Cerro Chajnantor at an elevation of 5600 m.

- Observe polarization of dust to observe small- and large-scale magnetic field structures and their role in regulating star formation in galaxies.
- Trace mass, spatial distribution, and peculiar motion of galaxy clusters through observations of the Sunyaev-Zel'dovich (SZ) effect.
- Search for the first detection of Rayleigh scattering during the epoch of recombination.
- Expand time domain astrophysics into FIR by exploring very energetic transients such as supernovae and gamma-ray bursts; will be particularly beneficial for dust-enshrouded sources.

1.2 The Fred Young Submillimeter Telescope

Success in FIR/Submillimeter astronomy demands high-sensitivity polarimetric, photometric, and spectroscopic mapping at several frequencies across the relevant band of the electromagnetic spectrum.[10] To meet this challenge, the Fred Young Submillimeter Telescope (FYST) was developed (see Figure 1.2). The 6-m primary mirror and crossed-Dragone optical design of FYST provide high angular resolution and image quality with a large field of view (8° at 3 mm).[11] FYST will operate in the millimeter to submillimeter range (100 GHz – 1.5 THz) with a nominal lifetime of 15 years and is capable of housing up to 3 instruments. However, the key feature of the facility is the site: the Cerro Chajnantor site in the Chilean Atacama Desert has an elevation of 5600 m. The high and

dry site is suitably positioned to negate much of the atmospheric effects, such as absorption due to atmospheric water vapor, that plague terrestrial infrared observatories, providing better transmission than any other site, particularly for the 850 GHz window.[12] CCAT will provide unrivalled mapping speeds in these windows,[10] and be able to observe beyond the confusion limited depth of previous terrestrial and spaceborne observatories.[9]

1.2.1 Prime-Cam

The upcoming generation of terrestrial observatories and accompanying astronomical instrumentation are designed around the concept of modularity. Instruments consist of different modules, such as a camera or spectrometer, which can be easily deployed, utilized, and swapped with a new module. Each module consists of optical components (lenses, filters, etc.), detector arrays, readout, and cryogenic components. The Prime-cam instrument is designed to incorporate independent modules, similar in design to the modules developed for ACTPol,[13,14] developed in collaboration with the Simons Observatory (SO). Similar cameras have been previously developed for astronomical observations,[13] but the unique capability of exploring the 850 GHz (350 μm) band makes this instrument crucial, as there are no immediate proposals for another instrument with this capability.[15] The designs of the 850 GHz instrument module require opto-mechanical structures, filtering, silicon lenses, readout electronics, control and data processing software, and cryogenics.

The 850 GHz module is of critical importance to extract astrophysical properties such as infrared luminosities and dust-obscured star formation rates in dusty star forming galaxies.[9] This module may therefore be used to constrain the peak of galactic dust spectral energy distributions, enabling precision estimates of source luminosity in the context of the evolution of these galaxies.[16] 850 GHz surveys will explore fainter sources than Herschel, and greater volumes than ALMA, increasing the likelihood of revealing rare sources.[9,10] Figure 1.3 show the current bands being designed for Prime-Cam: 280 GHz, 350 GHz, and 850 GHz. For the 280 and 350 GHz bands, the observed flux remains nearly constant due to the rise-up of the Rayleigh-Jeans tail, countering the cosmological dimming. This effect is great for selecting galaxies over this vast redshift range, but it fails to provide any information about the temperature of the blackbody, and therefore the total infrared luminosity of the galaxy. To achieve such a measurement one must sample the peak of the blackbody, for which the 850 GHz module is ideal over the expected range of redshifts.

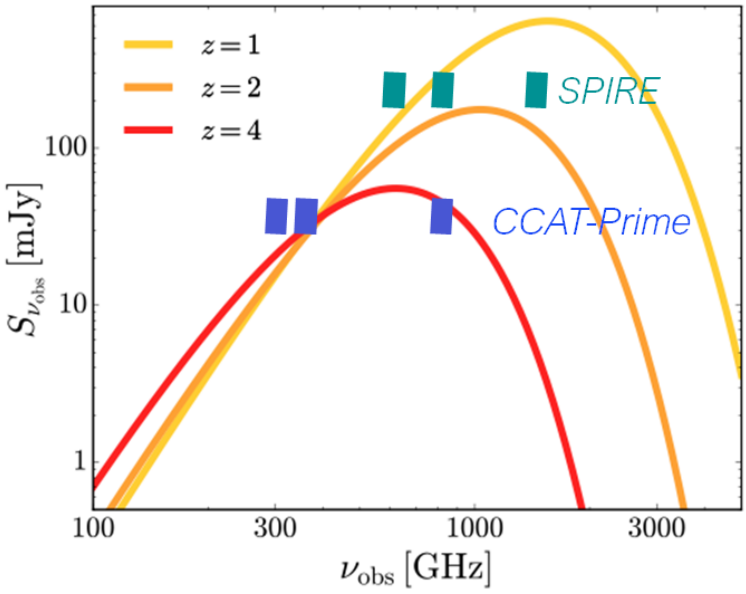

Figure 1.3: The current bands to be measured by Prime-Cam (280 GHz, 350 GHz, and 850 GHz) in blue compared against the bands measured by Herschel-SPIRE (600 GHz, 850 GHz, and 1200 GHz). A series of blackbody continua are included at increasing redshift. The 280 GHz and 350 GHz modules capture the Rayeigh-Jeans tail over the range of redshifts, and the 850 GHz module samples the peak of the blackbody in the expected range of redshifts.

The requirements placed by the key science drivers for Prime-Cam demand an instrument module with a large FoV and exceptional spatial resolution. Given the vital science achievable with this instrument, the 850 GHz module will occupy the privileged central position in Prime-Cam to aid in preserving the image quality. However, as the highest frequency module there are additional design considerations which must be made beyond the other instrument modules. Details of contribution around varying aspects of the design, fabrication, and characterization of components at cryogenic temperatures for instrument modules will be discussed throughout this work. The 850 GHz module is expected to be observing in 2026.

1.3 Kinetic Inductance Detectors

Since their invention in 2003,[17] there have been thousands of microwave kinetic inductance detectors (MKIDs or KIDs) used on sky in the mid-infrared to microwave regime across many instruments. Prime-Cam will include roughly 70,000 MKIDs; of that number, roughly 45,000 MKIDs will be used for the 850 GHz instrument module, which represents the most MKIDs on a single instrument module to date in the mid-infrared regime and beyond. Success of the 850 GHz module

hinges on the development of state-of-the-art detector arrays.

The combination of detector design and readout limitations has typically limited the number of detectors per line to approximately 500, which is taken as the baseline design for Prime-Cam,[18] meaning that the proposed 45,000 detectors for the 850 GHz module will require 180 coaxial cables and 90 cryogenic low noise amplifiers (LNAs). A single board handles up to four channels, meaning 23 Xilinx Radio Frequency System on a Chip (RFSoC) boards minimum are required. These exceptional hardware requirements can easily overwhelm both a fiscal and thermal budget. Extensive work has gone into expanding the readout to handle two[19] or more[20] octaves of readout (doubling or even tripling the number of detectors read) in a single channel with a minimum goal of halving the cryogenic radio frequency (RF) design.

Beyond hardware challenges are extensive software challenges. A single RFSoC will transmit data at a rate of roughly 128 Mb/s: a high data rate which will require careful setup of multi-gigabit networking equipment. Furthermore, control of each RFSoC with optimized tone powers and tuning for each detector is required in short time frames for rapid re-calibration of detectors, with overall integration with the facility control software as a whole. The software developed to achieve the ambitious detector count in the 850 GHz array is currently undergoing demonstrations on other modules.[21]

Development and application of a novel design to introduce a multi-octave MKID which would halve the required readout hardware without impacting performance is presented in Chapter 5.

1.4 A Blind Survey of Bright Submillimeter Galaxies

Blank-field millimeter and submillimeter continuum surveys have discovered hundreds of dusty, star-forming SMGs over the past decade. A technique is has been developed where one can determine the precise redshift of a distant dust-obscured galaxy given at least one strong emission line and photometric measurements.[22] A portion of this dissertation explores 12 SMGs measured by both the IRAM NOEMA interferometer and *H*erschel-Spire. The IRAM-NOEMA observations searched for the ^{12}CO and [CI] lines in these 12 SMGs, and SPIRE observations provided the results for photometric analysis in the 850 GHz band. The survey targets some of the brightest unlensed SMGs ever discovered in the northern CLS fields with $S_{850\mu\mathrm{m}} > 11$ mJy in a single SMA-identified source.[23] The faintness of most of these SMGs at near-IR/optical wavelengths precluded optical

spectroscopic observations despite lying in these well studied fields.

The proposed technique relies on determining the quantized redshift possibilities based on their probabilities based on the redshift determined from single line detection and from the photometric analysis. The probability of the possible redshift is relative to the redshift determined from photometry; a nearly even probability indicates the photometric redshift lies midway between two CO redshift values. Once spectroscopic redshifts have been assigned to each of the 12 SMGs, we can begin to constrain relevant metrics for each of these hyper luminous infrared galaxies (HyLIRGs). A particular metric of interest is the relationship between the flux at 350 GHz and the redshift, the gradient of which is compared against simulations as part of this survey.

1.5 Dissertation Overview

This chapter presented the motivation for FIR/Submillimeter astronomy, as well as for the 850 GHz module of Prime-cam. Then a detailed description of the optical and cryogenic design of the 850 GHz module for Prime-Cam is given in Chapter 2, with added emphasis on the design parameters considered in the optical design. Chapter 3 outlines the relevant theory MKIDs, including a brief foray into principles of superconductivity through noise performance of MKIDs. The cryogenic testbed for characterizing MKIDs is presented in Chapter 4, including details on the cryogenic system, the test box developed to characterize the prototype MKIDs, the radio frequency (RF) chain used to obtain signals from the detectors, and a summary of the readout. The design and performance of high-density, photon-noise-limited, multi-octave submillimeter kinetic inductance detectors for the Prime-Cam 850 GHz module are presented in Chapter 5. Finally, the results from a blind ^{12}CO redshift survey of bright SMGs are given in Chapter 6, and a summary of the dissertation is provided in Chapter 7.

Chapter 2

Prime-Cam: The 850 GHz Module

> If you want to find the secrets of the Universe,
> think in terms of energy, frequency and vibration.
>
> NIKOLA TESLA

The CCAT-prime observatory utilizes a 6 m telescope designed for submillimeter to millimeter wavelengths,[13] called the Fred Young Submillimeter Telescope (FYST). The optical design of FYST consists of a novel off-axis crossed-Dragone design, allowing for high throughput and a large diffraction-limited field-of-view (FoV).[11] Situated near the Cerro Chajnantor summit high in the Atacama Desert in Chile, CCAT-prime will be sited 5600 meters above sea level. With its high, dry site, CCAT-prime will be suitably positioned to negate much of the atmospheric effects, such as absorption due to atmospheric water vapor, which plague terrestrial infrared observatories.[24] The telescope optics are designed with high surface accuracy and low emissivity for superior surface brightness sensitivity in the submillimeter and millimeter atmospheric windows. Thus, particularly with the Prime-Cam instrument, CCAT-prime will provide unrivalled mapping speeds in these windows,[10] and be able to observe beyond the confusion limited depth of previous terrestrial and spaceborne observatories.[9]

The CCAT-prime observatory has been designed to answer fundamental astrophysical questions ranging in scope from Big Bang cosmology and the large-scale structure of the Universe down to the formation of stars and planetary systems in our own Galaxy. Such studies require high-sensitivity polarimetric, photometric, and spectroscopic mapping at several frequencies across the relevant band of the electromagnetic spectrum.[10] As these observations are based around the exploration of a 100 square degree field, field depth, mapping speed, and FoV are crucial considerations for every instrument module. The Prime-Cam instrument has been designed to explore several science goals

while considering these parameters.[9]

Chapter 2 details the designs of the Prime-Cam 850 GHz module. The requirements and constraints for the module are presented in Sec. 2.2. An analysis of the designs is presented in Sec. 2.3, highlighting both a preliminary design (Sec. 2.3.2) and the final design (Sec. 2.3.3) for the optics. Plans for integrating and testing the 850 GHz instrument module are presented in Sec. 2.4. As detailed below, the Prime-Cam 850 GHz module was optimized for the largest FoV and highest mapping speed possible.

Many of the details in Chapter 2 have been published in Huber, A. I. et al. "CCAT-prime: optical and cryogenic design of the 850 GHz module for Prime-Cam." In *Millimeter, Submillimeter, and Far-Infrared Detectors and Instrumentation for Astronomy XI*, Proc. SPIE, 2022 (Ref. 25).

2.1 Introduction

The Prime-cam instrument is designed to incorporate independent modules, similar in design to the modules developed for ACTPol,[13,14] developed in collaboration with the Simons Observatory (SO). Similar cameras have been previously developed for astronomical observations,[13] but the unique capability of exploring the 850 GHz (350 μm) band makes this instrument crucial, as there are no immediate proposals for another instrument with this capability.[15] The designs of the 850 GHz instrument module require opto-mechanical structures, filtering, silicon lenses, readout electronics, control and data processing software, and cryogenics.

Of the 8° diameter field-of-view (FoV) from FYST, roughly 4.9° is filled by Prime-Cam. This is achieved by incorporating a series of distinct instrument modules, as shown in Figure 2.1, with six instrument modules arranged around a seventh central module. Each of these modules fills a 1.3° diameter FoV, with 1.8° separation.[9,13] The baseline designs for Prime-Cam incorporate two imaging spectrometer modules utilizing Fabry-Perot Interferometers for line intensity mapping from 210 to 420 GHz,[26] and five polarization-sensitive modules at frequencies of 220 GHz, 280 GHz, 350 GHz, 410 GHz, and 850 GHz.[27] Each of these modules will incorporate kinetic inductance detector (KID) arrays due to ease of fabrication and readout while achieving the fundamental background limits required for Prime-Cam.[28] The overall configuration of Prime-Cam is shown in Figure 2.1.

The 850 GHz module is of critical importance to extract astrophysical properties such as infrared luminosities and dust-obscured star formation rates in dusty star forming galaxies.[9] This module

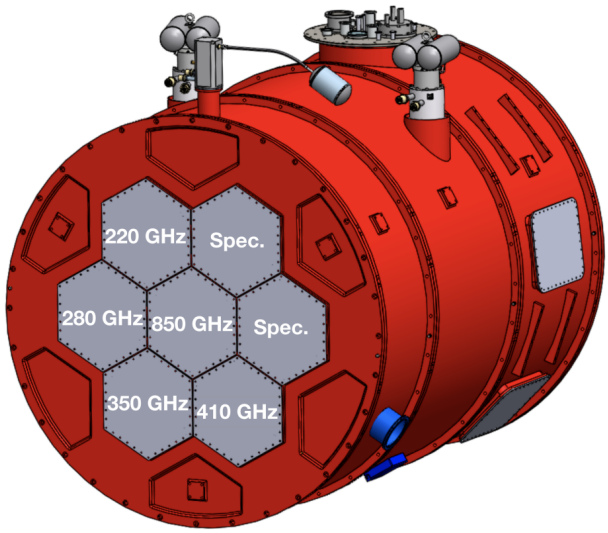

Figure 2.1: Rendering of Prime-Cam highlighting the modular nature of the instrument. The 850 GHz module occupies the central position. The baseline design for each module incorporates three silicon lenses, MKID arrays cooled to $\sim$ 100 mK, and a complex readout system. Image taken from Ref. 27.

may therefore be used to constrain the peak of galactic dust spectral energy distributions, enabling precision estimates of source luminosity in the context of the evolution of these galaxies.[16] The module will observe three times deeper than Herschel – a crucial feature that will not be matched until a 30-m submillimeter facility is developed. Additionally, the mapping speed is projected to be 1000 times that of SCUBA-2 while exploring greater volumes than the Atacama Large Millimeter/-submillimeter Array (ALMA), overall increasing the likelihood of revealing rare sources.[9,10] These requirements, which will be described in detail in Sec. 2.2, demand an instrument module with a large FoV and exceptional spatial resolution, both of which are possible thanks to FYST. Given the vital science achievable with this instrument, the 850 GHz module will occupy the privileged central position in Prime-Cam to aid in preserving the image quality.[12] However, as the highest frequency module there are additional design considerations which must be made beyond the other instrument modules.

2.2 Requirements and Constraints

The requirements for achieving high spectral resolution across a large FoV without degrading mappings speeds create a tradeoff between Fλ spacing, beam size, pixel sensitivity, and detector count. To an extent, both the efficiency and sensitivity increase with Fλ, while resolution and map-

ping speed decrease. Furthermore, decreasing Fλ results in an increase in detector count and decrease in beam size, which impacts both the RF chain considerations (Chapter 4) and feedhorn coupling efficiency and design. The high-level parameters around the design of each Prime-Cam instrument module stipulate that each module should: 1) have a 1.3° diameter FoV, 2) have high image quality, which is assessed based on the Strehl ratio across the FoV with a goal of >0.8 across the majority of the focal plane, and 3) achieve the maximum possible mapping speed. To achieve the minimum Fλ required for the 850 GHz module, the baseline design must include roughly 20,000 kinetic inductance detectors (KIDs), while a detector count as high as 50,000 is attainable. However, additional detectors require considerations to the thermal loading of the instrument, which will be discussed in Chapter 4. Each of the Prime-Cam instrument modules are designed to provide diffraction-limited image quality across the wide FoV provided from FYST.

From the outset of this study there were constraints to be considered in the design of the system. One constraint in the 850 GHz optical design is the choice of silicon for the lens material. The choice of cryogenic silicon was due to its excellent optical performance at the Prime-Cam frequencies and thermal conductance at cryogenic temperatures. Since silicon is unparalleled in terms of its optical properties and thermal conductivity, no other lens materials were explored, though with ongoing supply-chain issues and rising costs other alternatives may need to be explored for future modules. Note the exclusive use of silicon lenses prevents configurations of lenses with mixed indexes of refraction, such as the Cooke triplet.

A second constraint arises from the process of applying the anti-reflection (AR) coating to the lenses and the physical length of the Prime-Cam instrument itself. The application of the AR coating to the lens requires that the sagitta of the lens be less that 14 mm, else the manufacture time and difficulty increase and some losses in the effectiveness of the AR coating can occur.[29] Since the index of refraction may be, to first order, taken as proportional to the frequency, the 850 GHz module contends with the most extreme index of refraction in Prime-Cam. From the outset of this study it became apparent that there are two issues: 1) the available instrument module space in Prime-Cam prevents thinner lenses to be used in the 850 GHz module for longer focal lengths, and 2) each additional lens reduces the overall throughput of the system by 4%, setting a constraint on the number of lenses possible in the system. Thus, this study explored a range of systems using three to five lenses, resulting in the FoV ranging from 0.7°-1.3°, depending on the number of lenses used.

Throughout the design work for the 850 GHz module, several variations were explored to cover the parameter space of the instrument. Of particular interest were the length of the optics, number of lenses, and field curvature at the image plane. The first of these, length, was simple to constrain. It was clearly shown that any length beyond the $\sim$1000 mm limit of Prime-Cam resulted in both increased Strehl and FoV. When the system was optimized without constraining length for a four-lens system it was found that the ideal length was $\sim$1200 mm, which exceeds the maximum limit of the Prime-Cam design by $\sim$200 mm and is well beyond what can be conceivably accommodated. At shorter lengths it is clear that the Strehl ratio and FoV become, to an extent, competing variables. With a reduction in length, faster - and therefore thicker - lenses are required to the point that the limits imposed by the AR coating are exceeded.

In order to reduce the lens thicknesses and compensate for the reduced optical length of the 850 GHz module, a fifth lens was added to the designs. With a fifth lens included, the designs were able to achieve a 1.3° FoV. However, this design was unable to completely reduce the thickness of all the lenses to avoid fabrication issues for the AR coating. This confirms that having one lens exceeding the sagitta limit for the AR coating is unavoidable. Additionally, the inclusion of a fifth lens reduces the throughput of the instrument module by 4%, which results in a significant reduction in the mapping speed of the module.[12] It is clear that unless the number of the detectors is pushed higher, roughly 50,000 and beyond, there is no real advantage to the inclusion of a fifth lens.

The final variable explored in this work is the degree of allowable field curvature at the image plane of the system. This idea is being explored as an alternate means of compensating for the reduced optical length of the instrument module, which can be represented to first order as a tilt effect introduced at the detector array with the degree of tilt increasing radially across the array. As shown in Figure 2.2, increasing the maximum tilt, or angle of incidence, in the design results in a wider FoV and improvements to the Strehl ratio.

However, inclusion of tilt at any angle θ results in losses in the coupling efficiency of the feed-horns as the symmetry of the Gaussian beams is broken.[30] The overall effect of tilt is summarized in the power coupling coefficient, K'_{tilt}, which is defined as

$$K'_{tilt} = \exp\left[-2\left(\frac{\theta}{\theta_t}\right)^2\right], \tag{2.1}$$

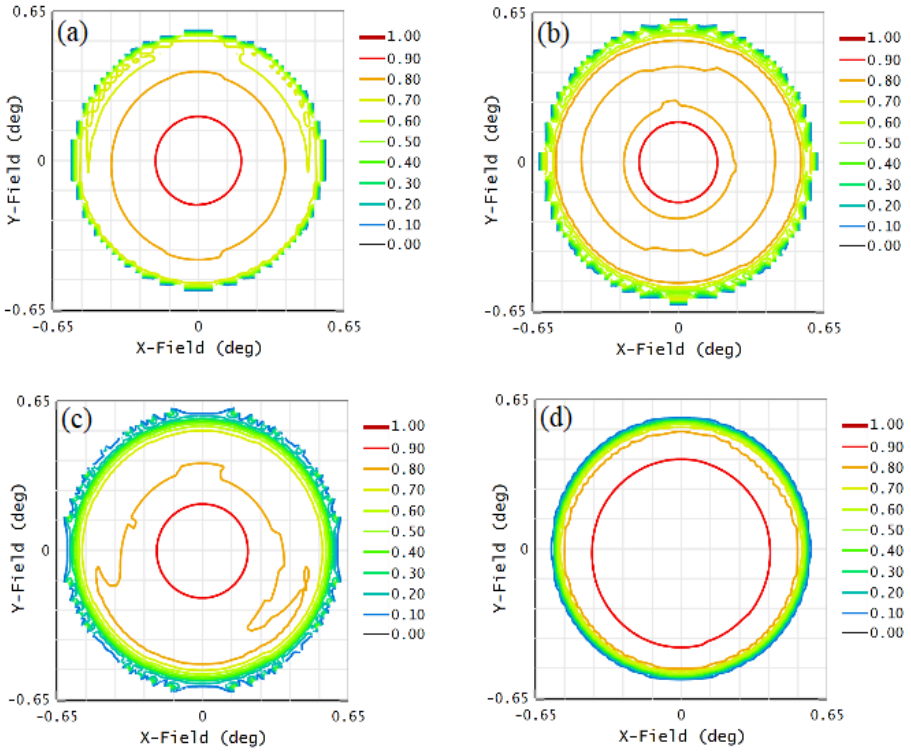

Figure 2.2: Simulations of the Strehl ratio across variations in the field curvature represented by the maximum allowable tilt: (a) 2°, (b) 4°, (c) 5°, and (d) 8°. Note that the Stehl ratio clearly improves as the field curvature increases, but at the cost of a potential reduction in detector sensitivity and increased cross-polarization.

where the θ_t is the tilt tolerance angle (where tilt results in a factor of e reduction) which, for the special case of tilt occurring at the beam waist is defined as

$$\theta_t = \frac{\lambda}{\pi}\sqrt{\frac{1}{\omega_{0a}^2} + \frac{1}{\omega_{0b}^2}}. \tag{2.2}$$

Here ω_{0a} and ω_{0b} are the beam waist radii of the incident beam and feedhorn respectively.

Based on the optical design, the beam waist radius of the incident beam, ω_{0a}, can be approximated as $\omega_{0a} \approx 0.84\lambda N$, where N is the f-number, for a value of $\sim$0.82 mm. Furthermore, assuming a feedhorn aperture radius of 1.35 mm and using a rough approximation of $\omega_{0b}/r_{fh} \approx 0.53$,[‡] ω_{0b} has an approximate value of $\sim$0.36 mm. The resulting values for the power coupling constant are given and Table 2.1, and indicate that the for the 850 GHz module the tilt should be less than 3° to keep the relative loss to the coupling power a maximum of $\sim 4\%$. Recall that the tilt is not eliminated

[‡]Value provided from collaboration with Doug Henke and assumes 55% coupling efficiency, which is a reasonable estimate for a system with $N \approx 1.5$.[31]

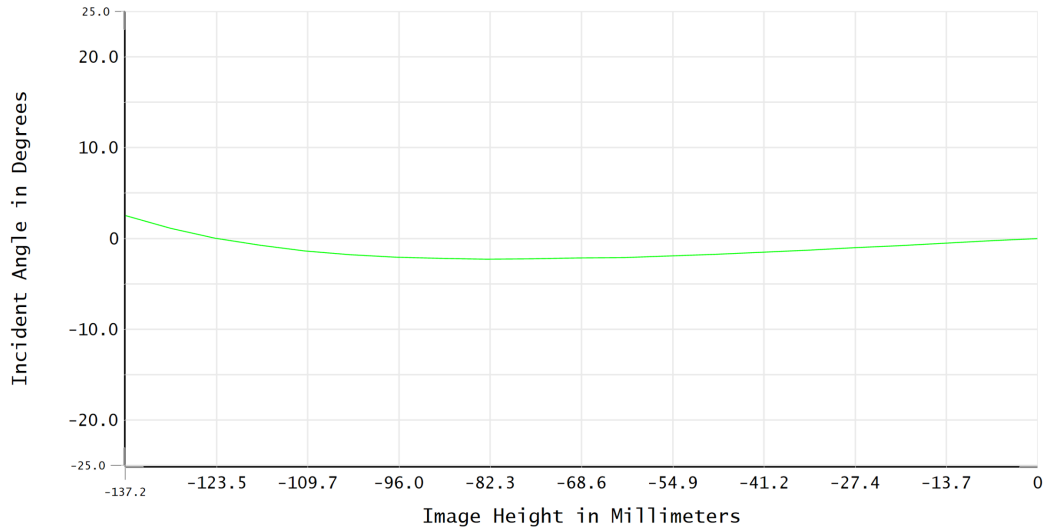

Figure 2.3: Angle of incidence of the chief ray across the radius of the focal plane. The system was optimized to have a maximum angle of incidence less than 3°.

entirely due to the improvements to the Strehl ratio and FoV. The limit of 3° was chosen as this ensures a significant margin between the absolute 4% loss that would follow from incorporating a fifth lens into the system.

Table 2.1: Values for the power coupling constant of the 850 GHz module across a representative sample of possible maximum tilt angles.

Tilt (°)	2.0	3.0	4.0	5.0	8.0
K'_{tilt}	0.979	0.954	0.919	0.877	0.715

There are two considerations gleaned from this study: the effects of tilt are dominated by beams with smaller waist radii - evident from Equation 2.2, and systems with smaller beams have a greater tolerance to the effects of tilt. Thus a reduction in coupling efficiency can be partially mitigated by having a system with smaller Fλ spacing, corresponding to a higher detector count over a given FoV. While increasing the detector count results in more spillover losses,[31] more detectors results in a net increase in mapping speed in the ranges considered in this work (see Ref. 12 for a full analysis). However, high detector counts present challenges to readout design and thermal budgeting (see Chapter 4). Figure 2.3 shows the angle of incidence or tilt at focal plane, where it is clear that the tilt is not constant across the detector arrays. The largest impact of field curvature lies on the edge of the FoV where there are fewer detectors.

Note that all of the issues presented in the parameter space are exacerbated at higher frequencies, an important consideration for proposed high-frequency instrument modules such as the 1500 GHz module.[10]

2.3 Optical Design and Analysis

This section will detail the first full optical design of the 850 GHz instrument module following a discussion of the parameter space considered in this work. The optical configurations presented are extensions of the three-lens cameras proposed for the SO[32] presented above. While they do share basic architecture, the designs across all the instrument modules for Prime-Cam have been modified to accommodate the shorter wavelengths and stringent requirements for the Strehl ratio across the FoV.[14] However, each of the designs benefit indirectly from the thoroughly studied systematics of these designs.[33,34]

Each optics module shares several basic components: filters, lenses, Lyot stop, baffles, and feedhorn coupled detectors. For the 850 GHz module, the filters include IR blockers, an alumina absorption filter, low pass filters and a bandpass filter to define the band, rather than relying solely upon the feedhorn cutoff to define the lower range of the band. Lenses will be made of cryogenic silicon to reduce thermal gradients across lenses, provide a consistent index of refraction across the band, and for its machinability in the case of the metamaterial AR coating.[35] Instrument modules are also intended to incorporate absorbers within the 4K volume to reduce stray light. In the case of the lower frequency modules, metamaterial tiles have been selected. However, these tiles have not been tested at the higher frequencies of the 850 GHz module and will require testing before they are accepted or rejected.

Development of the 850 GHz module for Prime-Cam will require careful consideration and planning as the system will be custom-designed for a single frequency. The first task will be to first model and optimize the optics to the 850 GHz band, then begin the opto-mechanical design of the system. Additionally, a cryogenic testbed must also be designed for developing and testing the 850 GHz module. A Bluefors LD250 dilution refrigerator[36] has been selected for this purpose.

The analysis of the designs below are based primarily on the FoV and Strehl ratio: the former is defined as the solid angle through which a given detector may observe,[37] and the latter is defined as the ratio of peak diffraction intensities of an aberrated wavefront to a perfect wavefront.[38] Both

values are calculated using Zemax OpticStudio software.[39] However, understanding the nature of these parameters, particularly the Strehl ratio, guides the optical design procedure.

2.3.1 Aberration Theory

The Strehl ratio quantifies the deviation of an optical system from the perfect Gaussian model, being limited by aberrations. In order for a system to be considered diffraction-limited, the Strehl ratio must be greater than 0.8. Aberrations describe deviations of light from the predictions of Gaussian theory, resulting in defocusing and blurring of images. In general, aberrations are not caused by manufacturing flaws, but rather from lens designs - there is no 'perfect' lens.[40] Descriptions of aberrations have existed for well over a century;[41] this work presents the simplified form of the Seidal or primary aberrations used to calculate the Strehl ratio.[39] Seidal aberrations deviate from chromatic aberrations in that the Seidal aberrations are determined by the shape of the lens, whereas chromatic aberrations arise due to variations in the index of refraction with wavelength.

Assuming rotational symmetry for an optical system, the aberration function $W(r,\theta;h')$ is dependent upon the image height from the optical axis, h', and pupil coordinates (r,θ). These variables provide three rotational invariants:[42] h'^2, r^2, and $h'r\cos\theta$. The order of an aberration term is equal to the sum of the powers of h' and r. The Seidal aberrations are defined as the aberration terms of degree four, giving the primary aberration function as the sum of five terms:

$$W(r,\theta;h') = {}_0W_{40}r^4 + {}_1W_{31}h'r^3\cos\theta + {}_2W_{22}h'^2r^2\cos^2\theta + {}_2W_{20}h'^2r^2 + {}_3W_{11}h'^3r\cos\theta \tag{2.3}$$

where the aberration coefficients are represented as ${}_iW_{jk}$, and the subscripts i, j, k represent powers of h', r, and $\cos\theta$, respectively. There is no h'^4 term in the Seidal aberrations since the aberration of the chief ray, defined as $r = 0$, must be zero.[42] The coefficients ${}_0W_{40}$, ${}_1W_{31}$, ${}_2W_{22}$, ${}_2W_{20}$, and ${}_3W_{11}$ represent the spherical aberration, coma, astigmatism, field curvature, and distortion, respectively. Aberrations are positive if they lead the reference sphere, and negative if they lag.

The best way to mitigate aberrations is to design a system with multiple elements.[40,43] If chosen correctly, the lenses will include positive and negative Seidal coefficients which, when summed, result in low total aberration of the system. While it is impossible to completely eliminate all aberrations, a well designed system will consider what level of aberration is acceptable and which aber-

rations to minimize. The best method to solve for aberrations is ray tracing, which may be done simply using commercial software packages. What follows below is a brief description of the Seidal aberrations, their impact on image quality (see Figure 2.4), and methods to reduce their impact.

2.3.1.1 Spherical Aberration

Spherical aberrations occur all over the image plane,[44] and are completely independent of the FoV. As seen in Equation 2.3, the spherical aberration increases with the fourth power on the aperture and exhibits axial symmetry. This aberration may be, in part, mitigated through the use of aspheric lenses. Additional methods include reducing errors in the distance between lenses[44] and using two different materials cemented together,[43] the latter of which cannot be used for the 850 GHz module as cryogenic silicon is the only material considered for the lenses.

2.3.1.2 Coma

Coma is not found at the center of the image plane but increases linearly with the FoV. From Equation 2.3, aberrations from coma increase with the third power on the aperture. The result in not axially symmetric, but rather has mirror symmetry about the meridional plane.[44] The result is a series of off-axis points akin to the tail of a comet with a head at the intended focus of the system,[43] similar to the effect of tilting a magnifying glass. Coma may be reduced by reducing errors in tilt or decentering of lenses in the system.

2.3.1.3 Astigmatism

Astigmatism is not found in the center of the image plane, but does show a quadratic relationship with the FoV. Furthermore, astigmatism increases with the second power on the aperture (Equation 2.3). Rather than having axial symmetry or meridional symmetry, astigmatism has mirror symmetry about both the meridional and sagital planes.[44] The result is different focal lengths in the two orthogonal planes.[40]

2.3.1.4 Field Curvature

Closely related to astigmatism is the field curvature, which is likewise not found at the center of the image plane and increases quadratically with both the FoV and on the aperture. However, field curvature is axially symmetric,[44] and arises since a spherical lens images spherical wavefronts onto

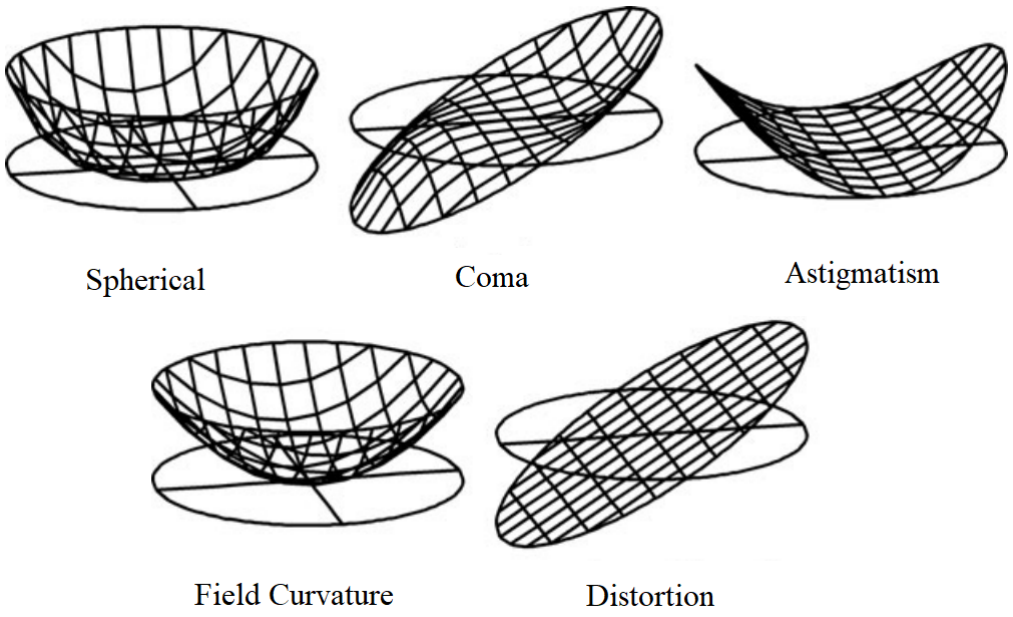

Figure 2.4: Shapes of the Seidal aberrations compared against a perfect reference wavefront. Image taken from Ref. 44.

another spherical surface, rather than imaging a plane to a plane.[43] The result is a system that shifts progressively further out of focus as the distance from the center of the image plane increases. A common method of reducing field curvature is to include a lens near the image plane known as a field flattener. Another method being explored is the use of curved detector planes.[40]

2.3.1.5 Distortion

Distortion is not found at the center of the image plane. This aberration arises when the magnification depends on the distance from the center of the image plane and has mirror symmetry about the meridional plane.[43] It is characterized as a rigid tilt in the wavefront.[44] Distortion is shown to increase cubically with FoV, and linearly on the aperture. The overall impact of distortion is that points are imaged without blur, but straight lines become curved in the image.[40]

2.3.2 Simons Observatory Instrument Module Design

The initial design of the 850 GHz module attempted to match the designs of the SO instrument modules in Prime-Cam. As can be seen in Figure 2.5, one can incorporate the SO design into the Prime-Cam instrument modules to include three cryogenically cooled lenses, a collimated beam at a 1 K Lyot stop, and wide FoV focused onto a densely populated detector array. While for the

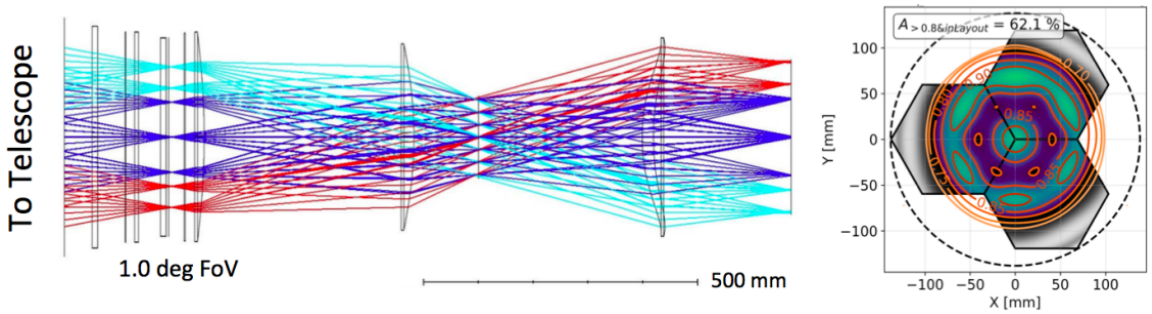

Figure 2.5: Left: Optical design of the 850 GHz instrument module utilizing the base SO design. Right: Simulation of the Strehl ratio across the FoV for the SO instrument module design for 850 GHz. The initial three-lens design resulted in low image quality across the focal plane as well as reduced FoV (1°) compared to other instrument modules. Image taken from Ref. 14.

lower frequency instrument modules this configuration proves effective, for the 850 GHz module this design results in a significantly reduced FoV (1°), as shown in the right panel of Figure 2.5, with only 62.1% of the FoV within the acceptable limit for the Strehl ratio. This motivates the need for additional study beyond the work done for the SO instrument module design to develop a system capable of achieving the Prime-Cam requirements for the 850 GHz module in terms of the instrument sensitivity, mapping speed, image quality, and FoV. The preliminary SO design serves as the baseline for comparison with the 850 GHz instrument module.

2.3.3 Finalized 850 GHz Module

To maximize the mapping speed of the instrument module, a four-lens design was selected over a five-lens design. This decision stems from a study of the trade-off between adding lenses to increase the field of view of the module with a reduction in throughput due to additional losses from the lenses (see Figure 2.6). Furthermore, the FoV was reduced to 1.1° to achieve the highest possible Strehl ratio over the largest area of the FoV possible. The result is a system with a Strehl ratio > 0.8 across nearly the entire FoV. This is accomplished in part by allowing a maximum angle of incidence of 4°. The design includes roughly 45,000 MKIDs across three silicon feedhorn arrays, which corresponds to a pixel pitch of 1.45 mm and an Fλ spacing of 1.48. Since the value of Fλ is reduced from the baseline value of 2.0, the system will be less susceptible to the effects of field curvature. Thus the design is a robust solution to the complex parameter space and constraints described above.

The optical design and simulated Strehl ratio of the 850 GHz module for Prime-Cam is presented in Figure 2.7. This optical design has undergone a design review chaired by third-party researchers.

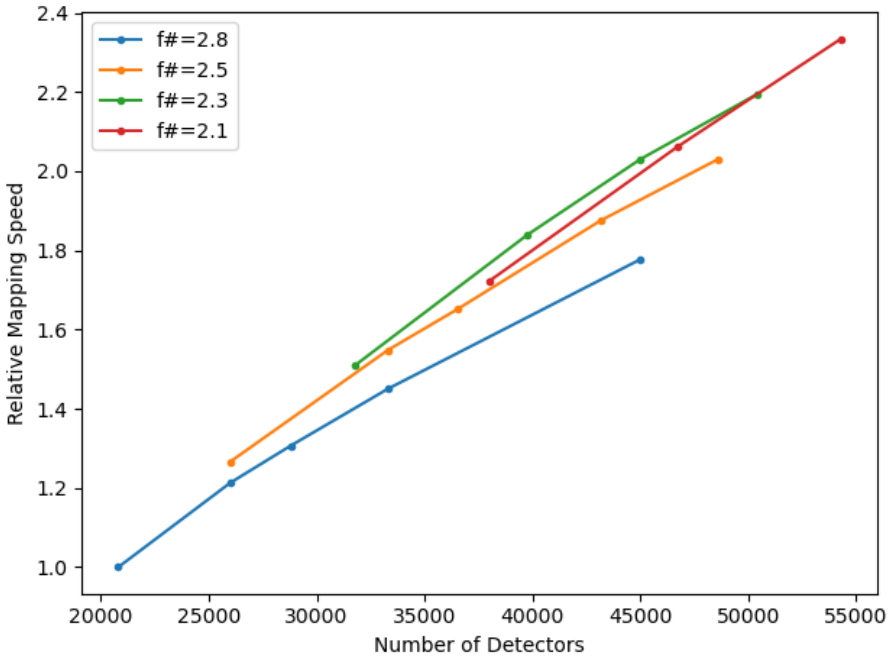

Figure 2.6: Mapping speed as a function of detector count across varying optical designs. To achieve the requisite FoV (F/# = 2.1, red) a fifth lens was added, resulting in a 4% loss in throughput and therefore mapping speed. Unless the detector count exceeds 50,000 it is clear that a four-lens design provides higher mapping speed than a larger FoV five-lens design.

From this design review, the decision to utilize a four-lens design rather than a three- or five-lens design was confirmed and upheld. While this design fails to achieve the desired instrumental field of view (1.3°) and introduces a loss to the throughput (and therefore the mapping speed), these losses can be mitigated by greatly increasing the pixel density on the focal plane. For the Prime-Cam 850 GHz module, a detector count of roughly 45,000 detectors - corresponding to 22,500 pixels - was selected to maximize the mapping speed for the four-lens design.

A 3D rendering of the 4-lens design is shown in Figure 2.8. Each of the lenses were designed as aspheric lenses to reduce spherical aberrations as much as possible. The lenses will be fabricated cryogenic silicon and will include a metamaterial AR with expected loss better than 2% per face of each lens. The second lens was designed with a narrower diameter to decrease the overall sag of the lens to within the soft limit of 14mm for the AR coating. This same technique did not result in enough of a reduction in sag for the third lens, so it remains thicker than the soft limit with the expectation that the AR coating will not perform as well for this lens but will still provide ideally 2% loss per face, whereas the AR coating for the other lenses may exceed expectations with losses

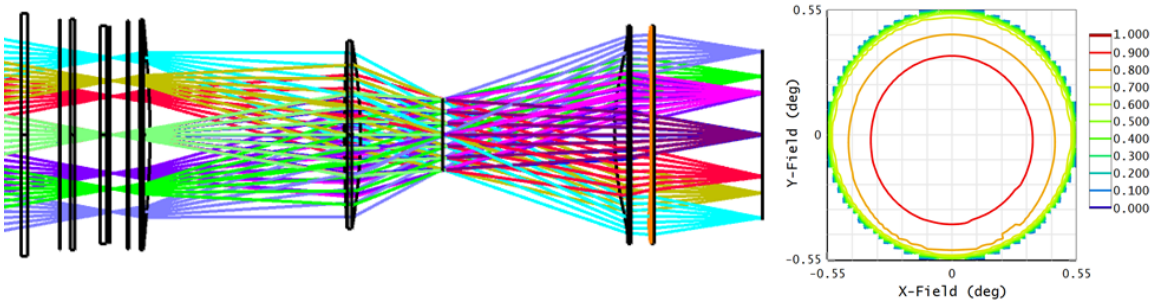

Figure 2.7: Ray trace model of the four-lens design of the 850 GHz module for Prime-Cam and simulation of the Strehl ratio across the FoV. The four-lens system results in high image quality across a 1.1° diameter FoV.

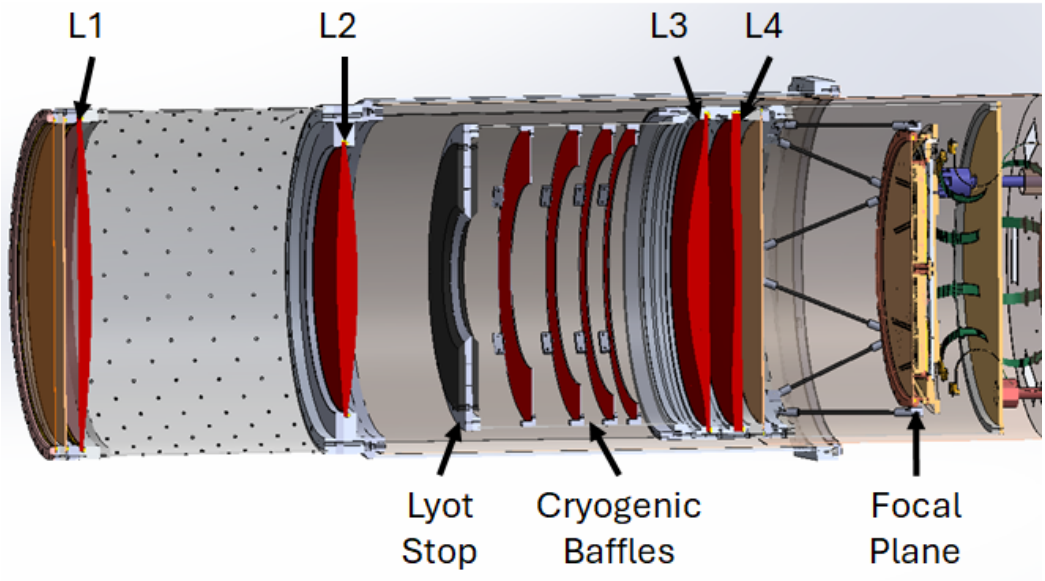

Figure 2.8: Cutaway model of the Prime-Cam 850 GHz module depicting the four lens design. Of the four lenses (labelled L1-L4), two are mounted in both the 4K and 1K volumes. The focal plane will be held at a constant temperature of roughly 100 mK. Also depicted are the Lyot stop and cryogenic baffles which limit the field size and limit the effects of dispersion. The structure of the module will be supported by a carbon fiber shell and carbon fiber reinforced polymer (CFRP) trusses.

closer to 1% or even sub-percentage performance. The inclusion of the fourth lens provides a field-flattening effect and serves to further reduce other aberrations as well. As will be shown below, the relationship between lenses 3 and 4 are crucial to the overall performances and represent the tightest tolerances for the optical design.

The four-lens design for the optics underwent a design review. Minor changes to the lens shapes were recommended due to machinability factors, which were achieved with minimal change to the optical quality, and the final parameters for the acceptable degree of tilt were defined at 2.5%. An attempt was made to incorporate the third and fourth lenses into a single thick lens to reduce a potential tolerancing issue between the two lenses. The idea was to produce an optically equivalent 3-lens design with a greater thickness (the distance between the two lenses divided by the index of the silicon). The result, shown in Figure 2.9, was a 30-mm thick meniscus lens with lens saggita (sag) of $\sim$61 mm and $\sim$48 mm for the convex and concave sides respectively. These are substantially beyond the sag limit for effective AR coating, especially for the concave side, given the soft limit of 14 mm. This design also saw an increase in vignetting, meaning overall loss of throughput in the module. Overall, the study further justified the inclusion of a fourth lens for the optical design.

With the finalization of the optical design, progress towards finalizing the opto-mechanical design of the module may proceed. A model including mounts for the four lenses, filters, and baffling has been designed and an assembly procedure has been drafted. The remaining major design chal-

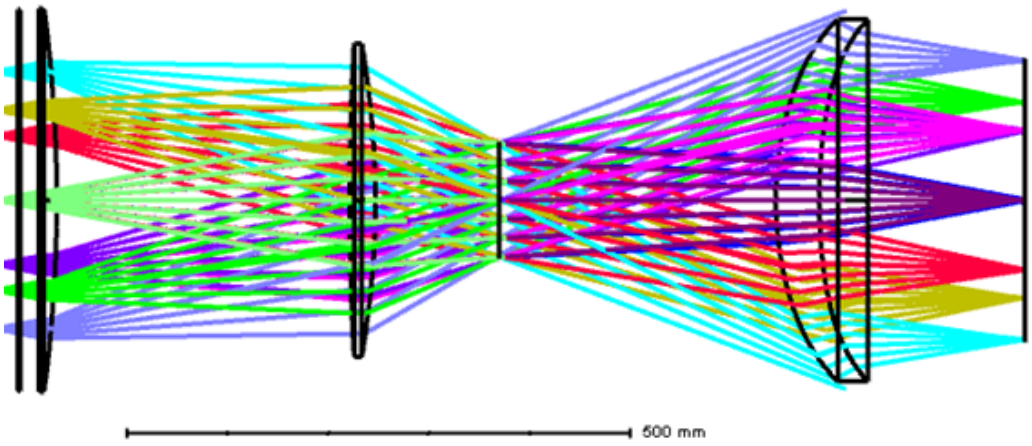

Figure 2.9: Ray trace of a three-lens equivalent to the four-lens design with greater edge thickness to effectively combine lenses three and four. The design resulted in a thick meniscus lens with prohibitively large lens sag and poor performance compared to the four-lens design.

lenge with the opto-mechanical design of the 850 GHz module is the design of the internal baffling to eliminate stray light, a process that is well understood.[34] A cutaway of the opto-mechanical design, presented in Figure 2.8, gives a complete view of the model, though the focal plane is currently subject to change as work to finalize the detector arrays continues. The Lyot stop determines the focal length of the system module and will include an absorptive material to aid in reducing stray light. This is true as well of the cryogenic baffles, which will reduce the impact of dispersion. The optical radius of the baffles is $\lambda/2$ larger than the field, wide enough to block the majority of stray light but not so narrow as to become the field stop of the module. A factor considered in these designs is the impact of thermal contraction on the required lengths for the shielding, which are variously made from aluminum, carbon fiber reinforced polymer (CFRP), and copper, each with their own coefficient of thermal contraction. The final system will be designed such that the optics will be properly aligned at cryogenic temperatures.

Fabrication of components for the readout chain will be carried out by both commercial vendors and within the NRC. The detector arrays will be fabricated by NIST,[45] and RF chain components by CryoElec.[46] Lenses and AR coatings will be manufactured by the University of Chicago,[35] and the infrared metal-mesh filters will be provided by Cardiff University.[47]

2.3.3.1 Tolerancing

To finalize the optical design before fabrication, the optical design underwent a tolerancing analysis. The analysis procedure utilized software included in the OpticStudio package.[39] Tolerancing the 850 GHz module was performed in two steps: an inverse increment method and Monte Carlo simulations. The entire system is defined by the merit function, which provides a single number for the overall performance of the design given the user-defined parameters and weights. For tolerancing the system configuration, the computationally determined Strehl ratio was used as the sole parameter in the merit function for multiple fields across the input plane, each with a weight of one. The analysis of the 850 GHz optical design assumes that the shapes and finishes of the lenses do not contribute to the tolerancing budget. Tolerancing is therefore limited to tilt, decentering, and position.

The inverse increment technique was used to develop baseline tolerances for the design. This technique determines value for each tolerance based on a given change in the merit function. The

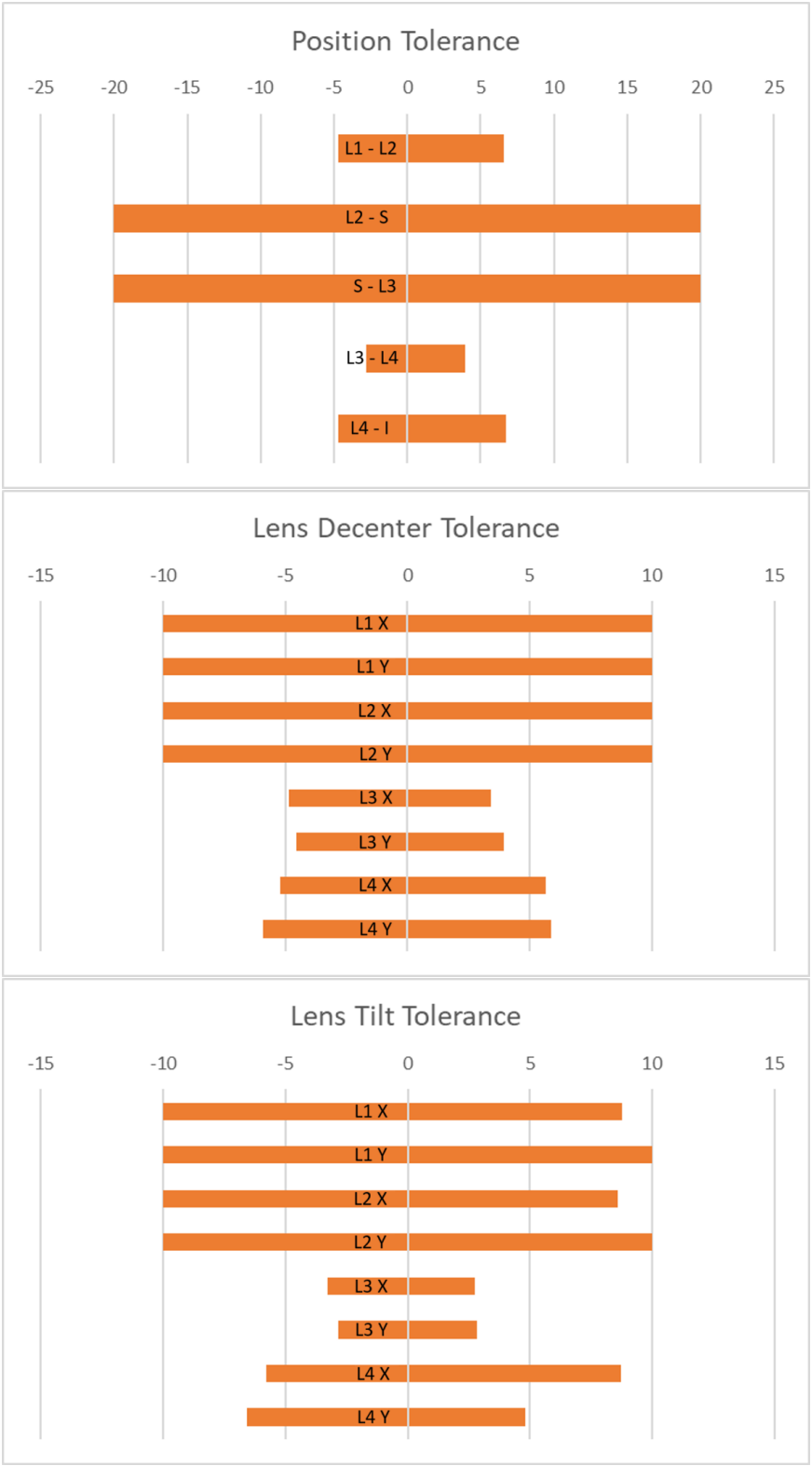

Figure 2.10: Position, decenter, and tilt tolerancing for the four-lens, 850 GHz optical design generated using the inverse increment technique. The tolerance labels are reference lenses with L, S for the Lyot stop, and I for the image plane. The tightest tolerances are between lenses 3 and 4.

perturbation of the variable is linear with the change in the system calculated simply as $\Delta = P - N$, where P is the the perturbed merit function value and N is the nominal value. The function iterates on the specified parameter until δ is equal to a user-defined shift in the merit function, commonly some percentage of the desired Strehl ratio. This proceeds until minimum and maximum values for each parameter, as shown in Figure 2.10. The resulting tolerances are relatively large, but fail to capture the effect of multiple shifts at once. The tolerances generated using this method are divided by the squareroot of the degrees of freedom, $\sqrt{\text{dof}}$, where the dof are the number of variables being toleranced: 21 for the four-lens design. As seen from Figure 2.10, the tightest tolerances are between lenses 3 and 4, meaning the relationship between lenses 3 and 4 is crucial for achieving diffraction-limited performance.

Once calculated, the values generated by the inverse increment method are used to limit the variables for the Monte Carlo simulations. Unlike the inverse increment method, a Monte Carlo simulation is able to explore perturbations in all variables simultaneously. A Monte Carlo simulation assigns each variable a random value with a certain standard deviation of the nominal value. The model is rerun using these values, and a value for the model is obtained. This process is repeated assigning new random values to the variable for a large number of samples. Once completed, the results are averaged to give a statistical estimate of the system.

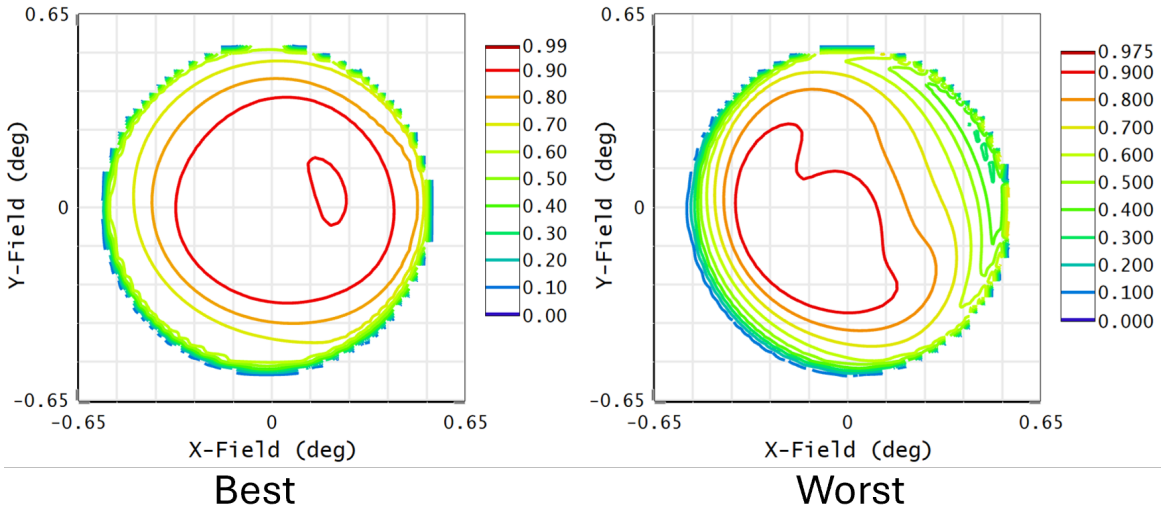

Figure 2.11: Best and worst Strehl ratios on the image plane as found for a single trial using 1000 Monte Carlo simulations. The deviations of the Strehl ratio across the image plane emphasize the importance of measuring the Strehl across the whole plane rather than just near the center. Compare with Figure 2.7.

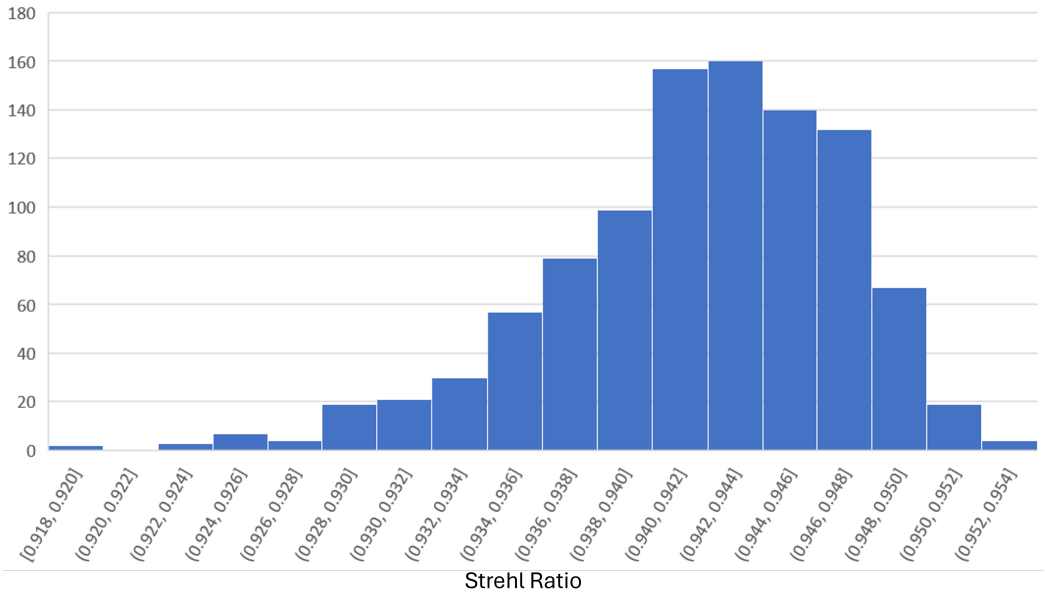

Figure 2.12: Histogram of the mean Strehl ratio across the image plane for a single trial using 1,000 Monte Carlo simulations.

For the 850 GHz optical design, 1000 Monte Carlo simulations were performed for each trial. To observe the overall effect on the image plane, the best and worst simulations were recorded for each trial (Figure 2.11). While the initial values for the tolerances provided an adequate starting point, for simplicity the tolerances for each type of variable were set to the lowest value of that class. For example, if the position tolerance of L1 is 1 mm, L2 is 4 mm, L3 is 4 mm, and L4 is 0.8 mm, the general position tolerance for all lenses is set to 0.8 mm. The results for the simulations are combined into a histogram shown in Figure 2.12, which depicts the mean Strehl ratio for the given fields and weights generated from the Monte Carlo simulations. In the case that the mean Strehl ratio for all the simulations is greater than a user-defined target, the chosen tolerances are deemed sufficient else the tolerances are tightened and the simulations iterated again. As mentioned above, the sensitivity of Strehl ratio to deviations lenses 3 and 4 was relatively high compared to other variables. To avoid increasing fabrication costs to meet exceptionally tight tolerances, general tolerances were found for the system and tighter constraints were found for lenses 3 and 4. The results after multiple iterations are summarized in Table 2.2. Analysis of the optical design concluded that great care needs to be taken in coupling lenses 3 and 4, while the remaining variables may be relatively lax. For this reason the opto-mechanical design for the system rigidly couples lenses 3 and 4 with a monolithic tube of aluminum to be fabricated with the requisite tolerances.

Table 2.2: General tolerances with noted exceptions for position, decenter, and tilt for the optical design. Values were found after multiple iterations of the Monte Carlo tolerancing method.

	General	Exception
Position	$\pm$0.5 mm	L3-L4: $\pm$0.4 mm
Decenter	$\pm$0.5 mm	L3: $\pm$0.4 mm
Tilt	$\pm0.16^{\circ}$	None

2.3.4 Module Systematics

In preparation for deployment, it is proposed that the system undergo a review of systematics prior to testing the integrated module. A portion of this work will be dedicated to an analysis of the optical design, including a study of optical distortions, beam ellipticity, sidelobe pickup, and ghosting. This has been performed for a three-lens module,[33] so the existing procedure may be trivially expanded and generalized for the four-lens design. This will be linked to a study on the systematic uncertainties of the finalized detector arrays, exploring features such as polarization leakage, non-linearity in detector response, readout crosstalk, and coupling efficiency.[27,48]

Additionally, the components will undergo a spectral response analysis to determine the overall response of the module to incoming radiation. This analysis is generally performed by measuring the passband or transmission of the components using a Fourier transform Spectrometer (FTS),[49,50] and is generally provided by suppliers for components such as filters and windows. Once the spectral response of the system has been measured, a series of simulations including atmospheric models to predict how the MKID arrays will perform in situ, using the skydip responsivity as a metric for comparison.[51] This will allow for simulations of results expected upon deployment, including the atmospheric transmission, spectral response of the module, and an astronomical calibration source for 850 GHz.

2.4 Integration and Testing

As detailed above, as components are fabricated they will be characterized and integrated into the module. Once fabrication is complete, the entire 850 GHz module will undergo a final assembly check to ensure the components fit, maintain alignment, and are properly fastened and coated. The system will then be dissembled and shipped to Cornell, where a cryostat, Mod-Cam,[52] has been designed to accommodate an entire instrument module, assuming Prime-Cam is installed on FYST.

In Mod-Cam, the 850 GHz module will undergo a series of tests to compare the systematics predicted with experimental results. The total system will also undergo tests to characterize the polarization angle and grid,[53,54] the final crosstalk of the fully integrated detector arrays and RF system,[55] the thermal properties of the module, the detector responsivities, and noise parameters.[56] Instrumentation for these tests will exist within the collaboration for commissioning other modules.

The timing for this portion of the project is uncertain. Manufacturing of FYST and Prime-Cam have already introduced delays in the proposed first light of CCAT-Prime, and deployment of the 850 GHz module of Prime-Cam is predicted to be deployed in the year 2026. Thus the integration and testing of the 850 GHz module represents a significant project for the future which will include integration and commissioning the 850 GHz module, analysis of first-light results, and preliminary science using the Prime-Cam instrument.

2.5 Conclusion

Chapter 2 described the optical designs of the Prime-Cam 850 GHz module. Sec. 2.2 outlined the requirements and constraints for the module which drive the decisions made for the optical design. Sec. 2.3 presented an analysis of the optical designs, focusing on the final design, which has undergone a third-party design review. Plans for integrating and testing the 850 GHz instrument module are presented in Sec. 2.4. The Prime-Cam 850 GHz module was optimized for the largest FoV and highest mapping speed possible, and is planned to be deployed in 2026. The overall assembly and testing of the opto-mechanical design represent significant future work. With a finalized optical design presented, Chapter 3 will explore the theory and parameters for the detector arrays for the Prime-Cam 850 GHz module.

Chapter 3

Microwave Kinetic Inductance Detectors

В тихом омуте черти водятся. (In a quiet whirlpool, devils dwell.)

RUSSIAN PROVERB

This chapter reviews the physics of microwave kinetic inductance detectors (MKIDs). The review begins with a summary of relevant topics in superconductivity (Sec. 3.2), framed in the context of the Bardeen-Cooper-Shrieffer and Mattis-Bardeen theories of superconductivity, building to topics in surface conductivity (Sec. 3.2.2) and superconducting resonators (Sec. 3.2.3). These topics include discussion of a basic resonator model and accompanying parameters useful in characterizing the device. Sec. 3.3 describes MKID properties relevant to their operation as detectors, focusing on measurable parameters including responsivity and noise performance. The deeper understanding of MKIDs provided by this chapter provides greater context to the remainder of the dissertation, particularly the development and testing of prototype MKID detectors as presented in Chapter 5. As will be discussed below, the scope of this review is limited to the study of titanium nitride (TiN) MKIDS, which is reflected in the assumptions used in the derivations.

3.1 Introduction

Since their invention in 2003,[17] there have been thousands of MKIDS used on sky in the mid-infrared to microwave regime across many instruments.[57] One of the first successful instruments to deploy MKIDs was the MUltiwavelength Sub-millimeter Inductance Camera (MUSIC), along with its prototype DemoCam.[58,59] These first photometric imagers were designed to accommodate four detectors per pixel, each sensitive to a different frequency, resulting in a multichroic camera. The combined detector count across all the pixels was 2,304. For comparison, the proposed detector arrays for the 850 GHz module of Prime-Cam are comprised of roughly 45,000 polarization sensitive

MKIDs, more than any planned millimeter/sub-millimeter instrument to date. The 850 GHz detector arrays build upon a legacy of increasingly sensitive, densely-packed arrays - a result of improved precision in fabrication capabilities.

The range of functionality in MKIDs extends beyond the millimeter/sub-millimeter regime, being sensitive to frequencies from the far-infrared to x-rays. Superconducting resonators, which comprise the MKIDs as will be seen below, have many uses beyond photon detection, including quantum computing circuitry and qubit systems, dark matter experiments, and quantum-limited parametric amplifiers.[60] With the ever-expanding body of research surrounding superconducting resonators, clearly a foundational understanding of their basic physics is required in order to characterize and optimize MKID arrays. Such a goal is non-trivial in the wide parameter space offered by MKID developers which include material properties, cryogenic capabilities, precision of fabrication, thin-film deposition capabilities, and geometric designs. What follows below navigates through the broad definitions and mathematical complexities to topics relevant to understanding the design and characterization of the prototype MKID devices presented in Chapter 5.

3.2 Superconductivity

Superconductivity is a fascinating phenomenon characterized by a combination of both perfect conductivity for direct currents and perfect diamagnetism where a field is expelled from bulk samples.[61] This occurs in a small range of temperatures at a critical temperature, T_c, above which a given sample is considered to be in either the normal state for type I superconductors or a transition state for type II superconductors. Figure 3.1 depicts a transition into a superconducting state through measurements of resistance as a function of temperature for a TiN thin film. A superconducting material will also transition back to a normal state in the presence of a sufficiently high field known as the thermodynamic critical field, H_c, which may be approximated as

$$H_c(T) \approx H_c(0)[1-(T/T_c)^2]. \tag{3.1}$$

Due to the relationship between current and magnetic field, this implies that there is also a critical current which generates the critical magnetic field. In general, type I superconductors are metals with low critical temperatures and fields, and type II superconductors are metallic compounds or

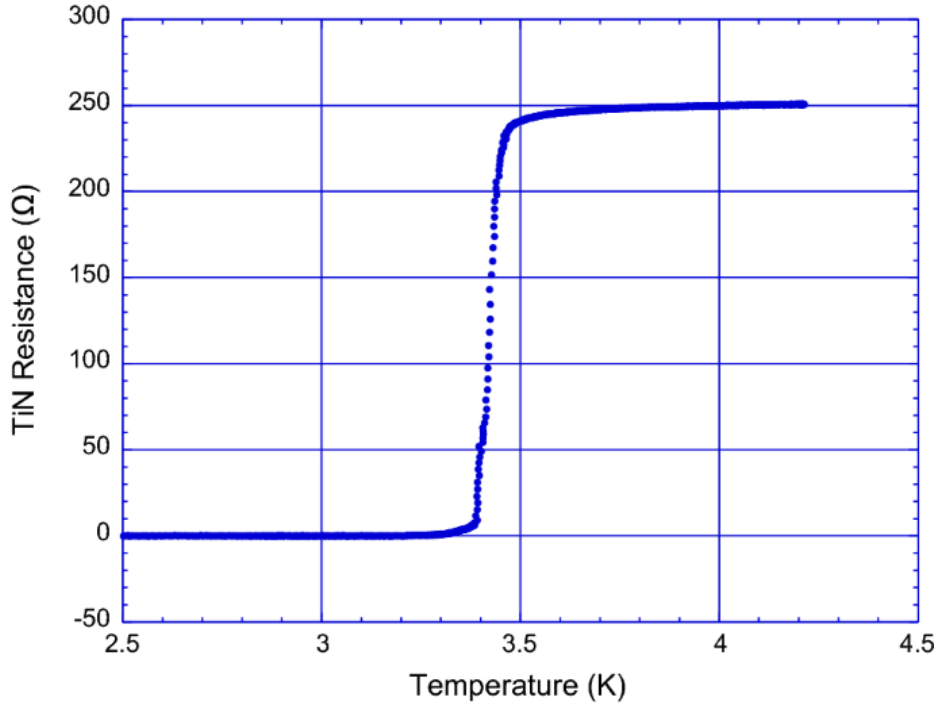

Figure 3.1: Measurement of resistance as a function of temperature for TiN around the critical temperature. The sharp drop in resistance around 3.4 K is indicative of a transition to a superconducting state. Image taken from Ref. 62.

alloys with high critical temperatures and fields. Additionally, thin film superconductors behave in a manner similar to type II superconductors even if they are a metal normally classified as a type I superconductor as a bulk sample.[61]

3.2.1 Charge Carrier Density

From the work of Bardeen, Cooper, and Schrieffer (BCS) a deeper understanding of the energy states of superconductors was developed in what is known as the BCS theory.[63] When a difference in the electronic specific heat was discovered between normal state conductors and superconductors below T_c, early studies concluded that the results between calorimetric and spectroscopic measurements only agreed if excitations occurred in pairs, leading to the groundbreaking conclusion that electrons in superconductors formed Cooper pairs, serving as the charge carriers in the superconducting state. The two electrons are formed due to phonon-electron interactions where a free electron attracts a phonon, which in turn attracts another electron.[64] This weak coupling between the two electrons is defined by a coherence length, ξ_0. BCS theory further predicted that the energy gap on either side of the Fermi energy, E_f, is a uniform value of $\Delta(T)$. Under the assumption that $T << T_c$,

the gap energy binding Cooper pairs is defined as

$$E_g(0) = 2\Delta_0 = 3.528 k_B T_c, \tag{3.2}$$

where Δ_0 is the binding energy for a single electron at $T = 0$. Thus for a Cooper pair to be broken, the electrons must absorb energy where $Eg \geq 2\Delta_0$. This energy corresponds to photons of frequency $\nu > 2\Delta/h) \approx (T_c/1\text{ K})74\text{ GHz}$.[65] For non-zero temperatures below T_c, the distribution of quasiparticles (electrons) is defined by the Fermi-Dirac distribution:

$$f(E) = \frac{1}{\exp(E/k_B T) + 1}. \tag{3.3}$$

With this distribution and the density of states for a superconductor defined in BCS theory ($\rho(E) = E/\sqrt{E^2 - \Delta^2}$), the quasiparticle density, n_{qp}, is calculated as

$$n_{qp} = 4N_0 \int_0^\infty f(E)\rho(E)\mathrm{d}E = 4N_0 \int_\Delta^\infty \frac{E}{\sqrt{E^2 - \Delta^2}} \frac{1}{\exp(E/k_B T) + 1}\mathrm{d}E. \tag{3.4}$$

Here Δ is the gap energy as defined at a temperature below T_c (usually approximated as Δ_o), and N_0 is the single spin density of states at the Fermi energy - a constant which is material-dependent. As shown in Ref. 66, Equation 3.4 can be approximated simply as

$$n_{qp}(T) \approx 2N_0 \sqrt{2\pi k_B T \Delta_0} \exp(-\Delta_0/k_B T). \tag{3.5}$$

Recall that there exists within superconductors two charge carriers: Cooper pairs and quasiparticles. We define the total density of charge carriers, n, as $n = n_s + n_{qp}$, where n_s is the density of Cooper pairs. As demonstrated in Equation 3.5, the relative densities of the charge carriers are temperature-dependent. Intuitively, at temperatures exceeding the critical temperature ($T > T_c$) there are no Cooper pairs and $n = n_{qp}$; at $T = 0$ one would infer that all charge carriers are superconducting and $n = n_s$. As will be shown below, an understanding of the charge carrier density is crucial to understanding the optical response of the kinetic inductance detectors as perturbations in the incident optical power on the detectors directly impacts n_{qp} and n_s.[66]

3.2.2 Surface Conductivity

The existence of two charge carriers is a deviation from the basic Drude model which defines conductivity in terms of a fluid model based on the movement of electrons.[64] As an analog, superconductors may be modelled using the two-fluid model in which n_s and n_{qp} are treated separately.[61] Consequently, the two-fluid model expresses the surface conductivity as a complex value:

$$\sigma(\omega) = \sigma_1 + i\sigma_2. \tag{3.6}$$

Here σ_1 and σ_2 respectively represent the real and complex parts and may be expressed in terms of the charge carrier densities:

$$\sigma_1 = \frac{n_{qp}e^2\tau_c}{m_e}, \tag{3.7}$$

$$\sigma_2 = \frac{n_s e^2}{m_e\omega}. \tag{3.8}$$

From Equations 3.7 and 3.8 the property that a superconductor has zero resistance when $\omega = 0$ is recovered. Since resistivity is the inverse of the conductivity ($\rho = 1/\sigma$), this implies that there is infinite conductance. Furthermore, the fluids can be separated into their contributions to the inductance of a circuit: the quasiparticles, n_{qp}, produce a resistance R, and the Cooper pairs, n_s, produce an inductance $\mathcal{L}_K$. One also observes that in an AC field of frequency ω, there is a phase delay in the Cooper pairs, which lag behind the changing electric field. This lag is the result of kinetic energy stored within the Cooper pairs and is manifest as inductance, resulting in a phenomenon primarily seen in superconductors known as kinetic inductance, which is defined as $\mathcal{L}_K = 1/\omega\sigma_2$.[67]

3.2.2.1 Mattis-Bardeen conductivity

Similar to the Drude model, the two-fluid model provides adequate approximations and phenomenology to first order. However, a more accurate model is required to explore and characterize the behaviour of kinetic inductance detectors. The Mattis-Bardeen theory defines the electrodynamics of superconductors taking into account the properties defined in BCS theory.[68] Crucially, this allows for the derivation of a relationship between the complex conductivity of a superconductor to the quasiparticle density. Following the derivation by Gao[69] and Noroozian,[66] the real and complex

conductivities are expressed as ratios to the normal conductivity, σ_n, as

$$\frac{\sigma_1}{\sigma_n} = \frac{2}{\hbar\omega}\int_{\Delta}^{\infty} \frac{E^2+\delta^2+\hbar\omega E}{\sqrt{E^2-\Delta^2}\sqrt{(E+\hbar\omega)^2-\Delta^2}}[f(E)-f(E+\hbar\omega)]\mathrm{d}E \tag{3.9}$$

and

$$\frac{\sigma_2}{\sigma_n} = \frac{2}{\hbar\omega}\int_{\Delta-\hbar\omega}^{\Delta} \frac{E^2+\delta^2+\hbar\omega E}{\sqrt{\Delta^2-E^2}\sqrt{(E+\hbar\omega)^2-\Delta^2}}[1-2f(E)]\mathrm{d}E \tag{3.10}$$

Under the assumption that the $\hbar\omega \ll \Delta$ and $k_BT \ll \Delta$, the integrals can be solved, yielding

$$\frac{\sigma_1}{\sigma_n} = \frac{4\Delta}{\hbar\omega}\exp(-\Delta/k_BT)\sinh(\xi_0)K_0(\xi_0) \tag{3.11}$$

and

$$\frac{\sigma_2}{\sigma_n} = \frac{\pi\Delta}{\hbar\omega}[1-2\exp(-\Delta/k_BT)\exp(-\xi_0)I_0(\xi_0). \tag{3.12}$$

From the above equations, K_0 and I_0 are the zeroth-order modified Bessel functions of the first and second kind, respectively, and the coherence length is $\xi = \hbar\omega/2k_BT$. The relationship between σ_1 and σ_2 with n_{qp} is shown using Equation 3.5:

$$\frac{\sigma_1}{\sigma_n} = \frac{n_{qp}}{N_0\hbar\omega}\sqrt{\frac{2\Delta_0}{\pi k_BT}}\sinh(\xi_0)K_0(\xi_0) \tag{3.13}$$

and

$$\frac{\sigma_2}{\sigma_n} = \frac{\pi\Delta_0}{\hbar\omega}\left[1-\frac{n_{qp}}{2N_0\Delta_0}\left(1+\sqrt{\frac{2\Delta_0}{\pi k_BT}}\exp(-\xi_0)I_0(\xi_0)\right)\right]. \tag{3.14}$$

Note that the above simplification uses the approximation $\Delta \approx \Delta_0[1+n_{qp}/2N_0\Delta]$ while ignoring the second order n_{qp} dependence.[65] To examine the relation between the complex conductivity and quasiparticle density, the derivatives are evaluated as $\delta\sigma(n_{qp},T)/\delta n_{qp}$, revealing that within the given approximations σ is a linear function of n_{qp}. Indeed, when a perturbation from a steady state is introduced, the relationship may be defined as[60,65]

$$\frac{\delta\sigma_1}{\sigma_1} = \frac{\delta n_{qp}}{n_{qp}} \tag{3.15}$$

and

$$\frac{\delta\sigma_2}{\sigma_2-\sigma_2(n_{qp}=0)} = \frac{\delta n_{qp}}{n_{qp}}. \tag{3.16}$$

This result confirms that a change in the quasiparticle density will result in a proportional change in the complex conductivity. For full details on the greatly condensed derivation of this relationship, the reader is directed to Gao (Ref. 69).

3.2.2.2 Surface Impedance of a Thin Film Superconductor

The above derivations have defined the relationship between the complex conductivity and quasiparticle density. To exploit this relationship experimentally, however, one finds that the complex conductivity is a difficult parameter to directly probe.[60] Instead, the response of the system relies on the measurement of the surface impedance, Z_s, defined as

$$Z_s = R_s + i\chi_s = \frac{1}{\sigma d}, \tag{3.17}$$

where d is the film thickness.[69] Using the definition of complex conductivity (Equation 3.6), Equation 3.17 can be rewritten as

$$Z_s = \frac{1}{(\sigma_1 - i\sigma_2)d} = \frac{\sigma_1 + i\sigma_2}{(\sigma_1^2 + \sigma_2^2)d}. \tag{3.18}$$

Assuming $\sigma_1 \ll \sigma_2$, which implies a superconducting state, Z_s is then defined as

$$Z_s \simeq \frac{\sigma_1}{\sigma_2^2 d} + i\frac{1}{\sigma_2 d}. \tag{3.19}$$

Thus in this approximation we define $R_s = \sigma_1/\sigma_2^2 d$ and $\chi_s = 1/\sigma_2 d$. Recall from Equations 3.7 and 3.8 the relationship between charge carrier density and complex conductivity, noting that in the limit $T = 0$ ($\sigma_1 \to 0$), we find $n_{qp} = 0$ and $n = n_s$, which meets our expectation that $R_s = 0$. Note that it is common to see the reactance defined in some references as $\chi_s = \omega L$. In the case $Z_s(0) = i\chi_s(0)$ and $\sigma(0) = -i\sigma_2(0)$, and thus $Z_s(0) = -1/i\sigma_2(0)$. In the thin film limit where the film thickness is less than the London penetration depth, fractional perturbation in conductivity is related to the fractional perturbation in surface impedance as

$$\frac{\delta Z_s}{Zs} = -\frac{\delta\sigma}{\sigma}. \tag{3.20}$$

In this superconducting limit we then find that, to first order:

$$\frac{\delta R_s}{\chi_s(0)} = \frac{\delta \sigma_1}{\sigma_2(0)}, \tag{3.21}$$

and

$$\frac{\delta \chi_s}{\chi_s(0)} = -\frac{\delta \sigma_2}{\sigma_2(0)}. \tag{3.22}$$

From Equations 3.15 and 3.16, these expressions may then be defined in terms of quasiparticle density:[66]

$$\frac{\delta R_s}{\chi_s(0)} = \frac{S_1(\omega)}{2N_0\Delta_0}\delta n_{qp}. \tag{3.23}$$

$$\frac{\delta \chi_s}{\chi_s(0)} = -\frac{S_2(\omega)}{2N_0\Delta_0}\delta n_{qp}. \tag{3.24}$$

In the limit of the approximation ($\hbar\omega \ll \Delta_0$ and $k_B T \ll \Delta_0$), S_1 and S_2 are defined as:[69]

$$S_1(\omega) \simeq \frac{2}{\pi}\sqrt{\frac{2\Delta_0}{\pi k_B T}}\sinh -\xi K_0(\xi), \tag{3.25}$$

and

$$S_2(\omega) \simeq 1 + \sqrt{\frac{2\Delta_0}{\pi k_B T}}e^{-\xi} I_0(\xi). \tag{3.26}$$

Finally, the ratio of the two perturbations is given as

$$\beta(\omega) = \frac{S_2(\omega)}{S_1(\omega)} = \frac{\delta \sigma_2}{\delta \sigma_1} = \frac{|\delta \chi_s|}{\delta R_s}. \tag{3.27}$$

Equation 3.27 is crucial as it determines the greater of the two responses and has been used to compare observed response measurements with theory. Furthermore, expressing the perturbations in relation to δn_{qp} is convenient as perturbations in the incident optical power, δP_0, directly determine δn_{qp}.[66]

Using the derivations and assumptions outlined in Sec. 3.2.2, the surface impedance as a function of frequency can be modelled for a given superconducting thin film, as depicted in Figure 3.2 for thin film titanium nitride (TiN). As defined in Equation 3.17, the surface impedance is shown in its components: the surface resistance (green) and the surface reactance (blue). Figure 3.2 shows that for low power electromagnetic fields ($\hbar\omega \ll \Delta$) the reactance is several orders of magnitude

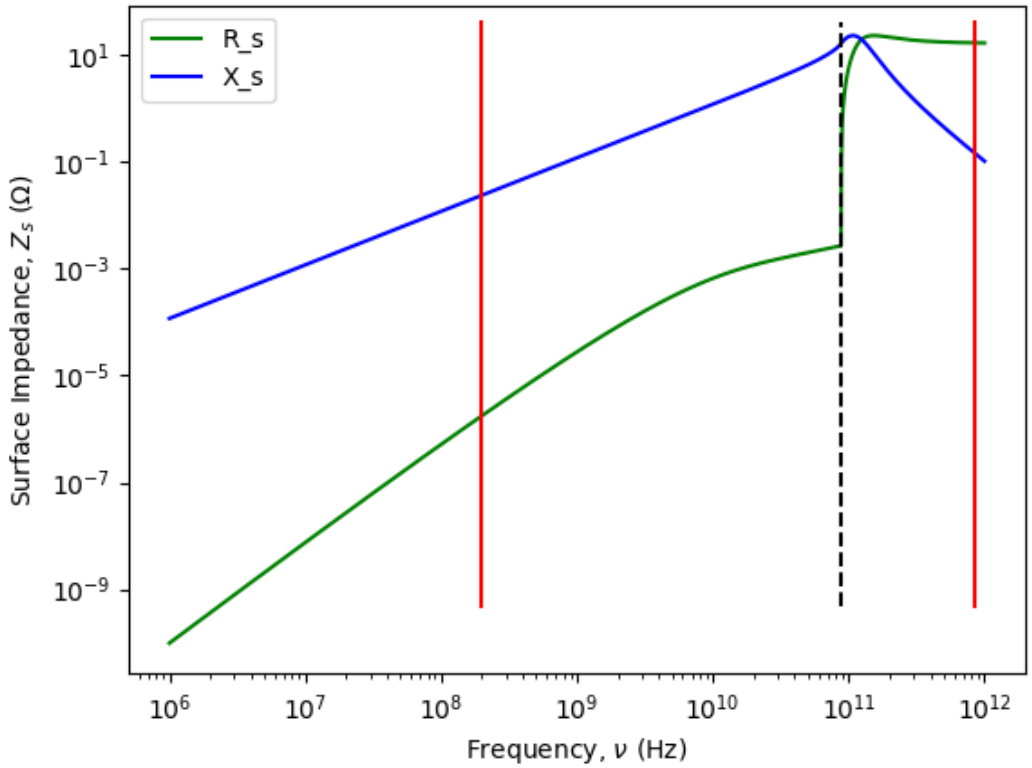

Figure 3.2: Model of the frequency-dependence of the surface impedance of a superconducting thin film made of titanium nitride (TiN). The surface impedance is split into the surface resistance (green) and surface reactance (blue). The dotted black line indicates the transition point where $\hbar\omega = 2\Delta$. The vertical red lines depict two regions of interest in the design of kinetic inductance detectors: the readout frequencies (left) and absorption frequencies (right). Note that in the readout regime, the input power will see a superconducting system, while the input radiation at 850 GHz exceeds the binding energy and interacts with the system in a normal state. This dichotomy defines the functionality of the kinetic inductance detector.

greater than the resistance, as expected. The transition between superconducting and normal states is denoted by the vertical dotted black line, showing a transition frequency of ∼90 GHz. On either side of the transition frequency are vertical red lines representing different regimes of interest for designing microwave kinetic inductance detectors. The left side represents the readout frequency at which probe tones will be used to measure perturbations in the reactance and is shown to be in the superconducting state. Conversely, the right line is within a region above the binding energy of the superconducting thin film TiN and represents incident frequencies in the band of interest (centered at 850 GHz). This duality of input is the crux of functionality of kinetic inductance detectors; incident photons will interact with the superconducting film, breaking Cooper pairs and,

consequently, perturbing the surface impedance of the superconducting film. As will be detailed below, the perturbations in the surface impedance can be measured in a meaningful way as part of a kinetic inductance detector using probe tones below the transition frequency. Figure 3.2 therefore highlights the importance of the above derivations showing the relationship between quasiparticle density and surface impedance.

3.2.3 Superconducting Resonators

Regardless of design, every MKID is based on an RLC circuit. The two most common designs for MKIDs are coplanar waveguide (CPW)[17] and lumped element MKIDs (LEKIDs).[70] This work focuses exclusively on the latter, which includes discrete components to tune the capacitance, inductance, and absorption of the detector. A basic circuit diagram of a LEKID is shown in Figure 3.3. Through careful selection of the components, each MKID can be tuned to have a unique resonance frequency. In general, a LEKID array consists of detectors with a constant inductance, and detectors are tuned through variations in the capacitance. Each detector is coupled to a transmission line, and excitation tones are sent to each resonator simultaneously (see Figure 3.4). It is this innate frequency multiplexing,[71] coupled with relative ease of fabrication, that makes MKIDs so appealing for large, dense arrays. MKIDs can also be designed to fill more of the focal plane than other technologies, such as transition edge sensors (TESs) at similar frequencies, resulting in greater mapping speeds.[27]

The resonance frequency for an RLC circuit is defined as

$$f_0 = \frac{1}{2\pi\sqrt{LC}} \tag{3.28}$$

where L represents the sum of the kinetic inductance, L_K, and the geometic inductance, L_g, or in terms of the sheet inductances as

$$L = \frac{l}{w}(\mathcal{L}_K + \mathcal{L}_g), \tag{3.29}$$

where the length and width of the inductor are denoted by l and w respectively. Using the inductance and surface resistance, R_s, outlined above, the internal quality factor of a superconducting resonator is given as

$$Q_i = \frac{\mathfrak{Im}\{Z_L\}}{\mathfrak{Re}\{Z_L\}} = \frac{\omega_0 L}{R_s} \simeq \frac{\sigma_2}{\sigma_1} \tag{3.30}$$

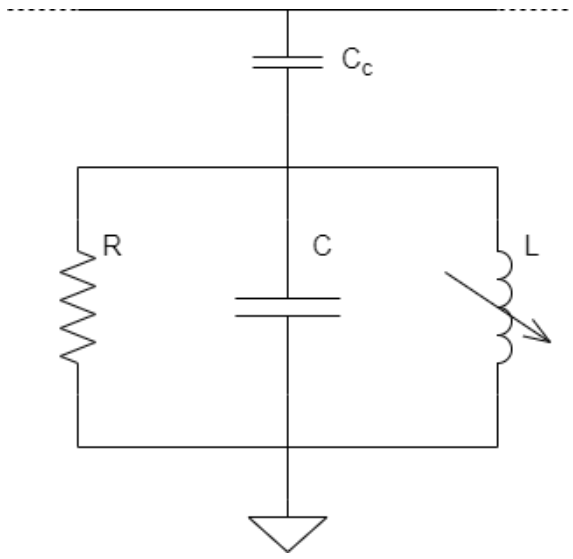

Figure 3.3: Circuit diagram of a kinetic inductance detector. A lumped element kinetic inductance detector consists of discrete components combined in parallel (L, R, and C). A kinetic inductance detector is typically capacitively connected to a transmission line (C_c). In many designs, the ground is virtual.

Note also that Q_i may be expanded in scope to include other sources of loss in the resonator, such as parasitics.[69]

The internal quality factor, Q_i, of a resonator is of crucial importance to a kinetic inductance factor as it determines the bandwidth of the resonance ($\Delta\omega = \omega_0/Q$). However, since R_s is relatively low compared to χ_s (see Figure 3.2), Q_i tends to be large, resulting in the equivalent of an incredibly narrow notch filter. To produce a resonator with a workable bandwidth, resonators are often connected to the stripline via a coupling capacitor, as shown in Figures 3.3 and 3.4. For such a capacitively coupled device, an additional quality factor, the coupling quality factor (Q_c), is included and is defined as[72]

$$Q_c = \frac{2(C_r + C_c)}{\omega_0 C_c^2 Z_0}, \tag{3.31}$$

where C_c is the coupling capacitance, C_r is the resonator capacitance, and Z_0 is the impedance of the microwave feedline. The overall quality factor of the resonator, Q_r, is the defined as

$$\frac{1}{Q_r} = \frac{1}{Q_i} + \frac{1}{Q_c}. \tag{3.32}$$

Since Q_i tends to be far greater than Q_c, it follows from Equation 3.32 that Q_r tends to be roughly

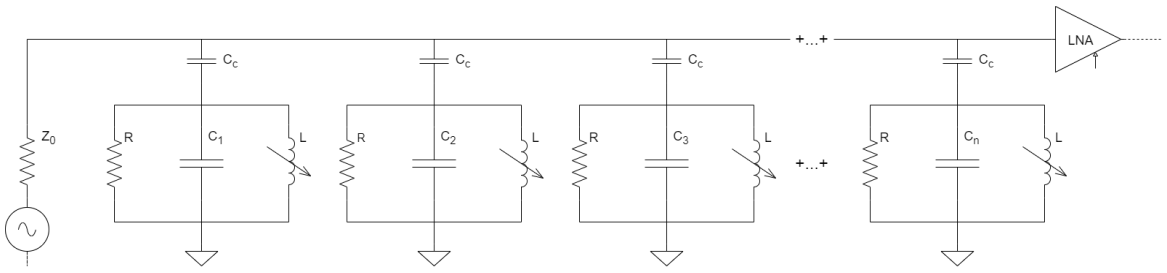

Figure 3.4: Circuit diagram demonstrating an array of lumped element kinetic inductance detectors. To multiplex these detectors each detector must have a unique resonance frequency, f_0, which is accomplished by ensuring each detector has a unique capacitance (C_1, C_2, ... C_n). The detectors are all coupled to a single transmission line, through which excitation tones for each resonator are sent to each detector simultaneously.

equal to Q_c, resulting in a wider and shallower resonance.

The resonator itself acts as an impedance to ground, albeit a virtual ground, with a frequency-dependant impedance defined as[67]

$$Z_R(\omega) = \frac{1}{i\omega C_c}\left[\frac{1-\omega^2 L_T(C_r+C_c)+i\omega R(C_r+C_c)}{1-\omega^2 L_T C_r + i\omega R C_r}\right]. \tag{3.33}$$

When measured on-resonance, Equation 3.33 may be simplified as

$$Z_R(\omega_0) = \frac{Z_0 Q_c}{2Q_i}\frac{1}{1+i\varepsilon}, \tag{3.34}$$

where $\varepsilon = C_r/Q_i C_c$. Following the derivation in Ref. 51, the transfer function of resonator circuit assuming a microwave readout is defined as

$$S_{21} = \frac{Z_R}{Z_R + Z_0}, \tag{3.35}$$

where the the scattering parameter S_{21} is a measureable quantity using instruments such as a vector network analyzer (VNA). The result is a frequency dependent value for the transfer function:

$$S_{21}(\omega) \simeq 1 - \frac{Q_r}{Q_c}\frac{1}{1+2iQ_r\delta x}, \tag{3.36}$$

where $\delta x = (\omega-\omega_0)/\omega_0$. As most resonators have asymmetric lines shapes,[67,69,73] the fit for $S_{21}(\omega)$ can be modified to include a complex coefficient, A, and an additional parameter to define the asym-

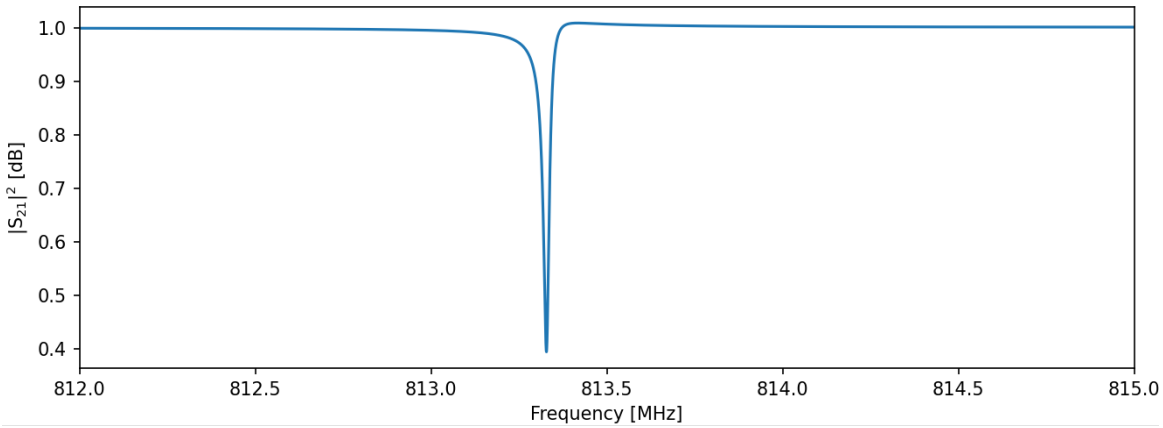

Figure 3.5: Sample resonance shape with asymmetry. The resonator was simulated using empirical results from the BLAST-TNG experiment for an 850 GHz LEKID. See Ref. 74 for details.

metry, χ, giving

$$S_{21} = A\left(1 - \frac{Q_r}{Q_c}\frac{1+i\chi}{1+2iQ_r\delta x}\right). \tag{3.37}$$

A sample resonator simulated using Equation 3.37 is shown in Figure 3.5. The simulated resonator uses empirical values taken from the BLAST-TNG experiment (details in Ref. 74): $Q_r = 32,826$, $Q_c = 54,460$, $A = 1$, $\chi = -0.2$, and $\omega_0 = 813.33$ MHz.

Aside from the internal resonance and capacitive coupling to the feedline, there are many types of coupling that can arise in a resonator, all of which would be deemed parasitic. This includes coupling to metals or dielectrics in the packaging, noise inherent in the system (two-level system or TLS effects[75]), or even other resonators. Regardless of their source, these parasitic capacitances can impact ω_0, Q_r, or introduce further asymmetry in S_{21}. Ongoing efforts to push the precision and noise performance of MKIDs require designs that can reduce, circumvent, or eliminate these effects.

3.3 Microwave Kinetic Inductance Detector Theory

This section focuses on the derivation of MKID responsivity related to fluctuations in temperature, T, and absorbed optical power, P_{abs}. The noise and sensitivity, which are used to quantify the amount of power an MKID can detect, are also discussed below. Understanding these parameters are crucial in calibrating the performance of MKIDs.

3.3.1 Thermal Properties

From the inception of the kinetic inductance detector the relationship between temperature and surface conductivity has been known.[60] As detailed above, the change in surface conductivity (or surface impedance) is a result of a change in the quasiparticle density. Using the formulations given in Gao,[69] the thermal responsivity of the resonant frequency, R_T, can be determined as:

$$R_T = \frac{\mathrm{d}f_0}{\mathrm{d}T} = \frac{\mathrm{d}f_0}{\mathrm{d}\sigma_2}\frac{\mathrm{d}\sigma_2}{\mathrm{d}n_{qp}}\frac{\mathrm{d}n_{qp}}{\mathrm{d}T} \tag{3.38}$$

To obtain a relation between f_0 and σ_2, one first relates the two in the form

$$\frac{\mathrm{d}f_0}{\mathrm{d}\sigma_2} = \frac{\mathrm{d}f_0}{\mathrm{d}\mathcal{L}_K}\frac{\mathrm{d}\mathcal{L}_K}{\mathrm{d}\sigma_2}. \tag{3.39}$$

Using the definition of f_0 given in Equation 3.28, one derives that

$$\frac{\mathrm{d}f_0}{\mathrm{d}\mathcal{L}_K} = -\frac{C}{4\pi(LC)^{3/2}} = -\frac{\alpha f_0}{2\mathcal{L}_K}, \tag{3.40}$$

where $\alpha = L_K/L$. Recall from above that $\mathcal{L}_K = 1/\omega\sigma_2$. Deriving this relation with respect to σ_2 results in

$$\frac{\mathrm{d}\mathcal{L}_K}{\mathrm{d}\sigma_2} = -\frac{1}{\omega\sigma^2} = -\frac{\mathcal{L}_K}{\sigma_2}. \tag{3.41}$$

Thus one finds

$$\frac{\mathrm{d}f_0}{\mathrm{d}\sigma_2} = \frac{\alpha f_0}{2\mathcal{L}_K}\frac{\mathcal{L}_K}{\sigma_2} = \frac{\alpha f_0}{2\sigma_2} \tag{3.42}$$

From Equation 3.5, we can also derive the dependence of the quasiparticle density on temperature as

$$\begin{aligned}\frac{\mathrm{d}n_{qp}}{\mathrm{d}T} &= \frac{2N_0 2\pi k_B\Delta_0}{2\sqrt{2\pi k_B T\Delta_0}}e^{-\Delta_0/k_BT} + 2N_0\sqrt{2\pi k_B T\Delta_0}e^{-\Delta_0/k_BT}\frac{\Delta_0}{k_BT^2} \\ &= \frac{n_{qp}}{T}\left(1+\frac{\Delta_0}{k_BT}\right).\end{aligned} \tag{3.43}$$

Finally, the relationship between σ_2 and n_{qp} as derived by Gao[69] is defined as

$$\frac{d\sigma_2}{dn_{\mathrm{qp}}} = \frac{\sigma_2}{2N_0\Delta_0}\left(1+\sqrt{\frac{2\Delta_0}{\pi k_BT}}e^{-\xi}I_0(\xi)\right). \tag{3.44}$$

Following these derivations, the dependence of the resonance frequency, f_0, on temperature is given as the product of Equations 3.42-3.44:

$$\begin{aligned} R_T &= \frac{\alpha f_0}{2\sigma_2}\frac{\sigma_2}{2N_0\Delta_0}\left(1+\sqrt{\frac{2\Delta_0}{\pi k_B T}}e^{-\xi}I_0(\xi)\right)\frac{n_{qp}}{T}\left(1+\frac{\Delta_0}{k_B T}\right) \\ &= \frac{\alpha f_0 e^{-\Delta_0/k_B T}}{T}\sqrt{\frac{2\pi k_B T}{\Delta_0}}\left(1+\frac{\Delta_0}{k_B T}\right)\left(1+\sqrt{\frac{2\Delta_0}{\pi k_B T}}e^{-\xi}I_0(\xi)\right) \end{aligned} \tag{3.45}$$

From Equation 3.45, one can extrapolate that the main parameters to consider in determining the thermal responsivity of a kinetic inductance detector are the energy gap, Δ_0, which as defined by Equation 3.2 is dependent on T_C, and the kinetic inductance fraction, α. A theoretical response for a TiN MKID is shown in Figure 3.6, where it is clear that for low bath temperatures, as will be used for Prime-Cam, the MKID array will be relatively insensitive to fluctuations in bath temperature.

Another factor to consider is the impact of temperature on the internal quality factor of the resonator, Q_i, which is defined in Equation 3.30. Under the assumptions $\xi << 1$ and $n_{qp} << N_0\Delta_0$, Equations 3.13 and 3.14 can be approximated using $I_0(\xi)\approx 1$, $K_0(\xi)\approx \ln(1/\xi)$, $\sinh\xi\approx\xi$, $e^{-\xi}\approx 1$, and $n_{qp}/N_0\Delta_0\approx 0$. These equations may then be simplified as

$$\frac{\sigma_1}{\sigma_n} = \frac{n_{qp}}{N_0\hbar\omega}\sqrt{\frac{2\Delta_0}{\pi k_B T}}\xi\ln(1/\xi) \tag{3.46}$$

and

$$\frac{\sigma_2}{\sigma_n} = \frac{\pi\Delta_0}{\hbar\omega}. \tag{3.47}$$

Thus under these conditions, the internal quality factor may be defined as

$$Q_i = \frac{\pi\Delta_0 N_0}{n_{qp}}\sqrt{\frac{\pi k_B T}{2\Delta_0}}\frac{1}{\xi\ln(1/\xi)} \propto \frac{1}{\xi\ln(1/\xi)}, \tag{3.48}$$

where it is clear that Q_i is dependent on f, T, Δ_0, and α. These examples highlight the fact that many key parameters for a kinetic inductance detector may be determined by performing dark tests on an array.

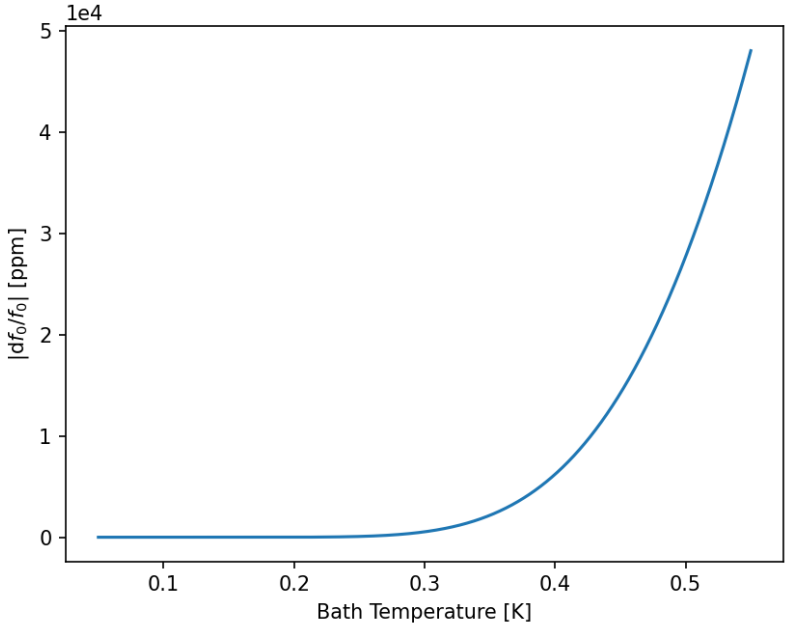

Figure 3.6: Theoretical magnitude of the shift in resonance frequency as a function of temperature for a TiN MKID in parts per million. Since the expected bath temperature is projected to be at roughly 100 mK, the TiN detectors are expected to exhibit low sensitivity to base temperature fluctuations.

3.3.2 Optical Responsivity

In order to employ MKIDs as photon detectors, it is crucial to understand how they respond to absorbed photons. In a form similar to Equation 3.38, the optical responsivity, R_P, of a MKID at a fixed bath temperature is defined as:

$$R_P = \frac{\mathrm{d}f_0}{\mathrm{d}P_{abs}} = \frac{\mathrm{d}f_0}{\mathrm{d}\sigma_2}\frac{\mathrm{d}\sigma_2}{\mathrm{d}n_{qp}}\frac{\mathrm{d}n_{qp}}{\mathrm{d}P_{abs}}. \tag{3.49}$$

Here Equations 3.42 and 3.44 combine and simplify as before, giving

$$\begin{aligned}\frac{\mathrm{d}f_0}{\mathrm{d}\sigma_2}\frac{\mathrm{d}\sigma_2}{\mathrm{d}n_{qp}} &= \frac{\alpha f_0}{2}\frac{1}{2N_0\Delta_0}\left(1+\sqrt{\frac{2\Delta_0}{\pi k_B T}}e^{-\xi}I_0(\xi)\right) \\ &\simeq \frac{\alpha f_0}{4N_0\Delta_0}\left(1+\sqrt{\frac{2\Delta_0}{\pi k_B T}}\right),\end{aligned} \tag{3.50}$$

which assumes that $\xi << 1$. It is clear that the optical responsivity is dependent on the system geometry, temperature, and material properties. In the case $\xi > 1$, $e^{-\xi}I_0(\xi) \to \ln(1/\xi) = \sqrt{2k_BT/hf_0}$,

resulting in cancellation of the temperature dependence.[67]

The final term in Equation 3.49 deals with dependence of n_{qp} on the absorbed optical power. Recall that quasiparticles arise when Cooper pairs split. In a superconducting thin film the generation rate of quasiparticles is denoted as Γ_g. Quasiparticles also recombine with a rate Γ_r, and in an equalibrium state $\Gamma_g = \Gamma_r$. Since there are different mechanisms which generate quasiparticles, Γ_g may be further broken into the thermal generation rate, Γ_t, optical generation rate, Γ_o, and readout generation rate, Γ_{ro}, the last of which is due to power absorbed from the readout probe tone.[60] Thus[65]

$$\Gamma_g = \Gamma_t(T) + \Gamma_o(P_0) + \Gamma_{ro}(P_{ro}). \tag{3.51}$$

The number of quasiparticles as determined from both the generation and recombination rates of quasiparticles is defined as

$$\frac{\mathrm{d}n_{qp}}{\mathrm{d}t} = \Gamma_t(T) + \Gamma_o(P_0) + \Gamma_{ro} - \Gamma_r. \tag{3.52}$$

Here the derivation of the optical power may be simplified depending on certain cases as outlined in Ref. 67. In the case of a device which is dominated by thermally generated quasiparticles, such as TiN MKIDs, Equation 3.52 may be simplified to[74]

$$\frac{\mathrm{d}n_{qp}}{\mathrm{d}t} = \Gamma_t(T) + \Gamma_o(P_0) - \Gamma_r, \tag{3.53}$$

where $\Gamma_r = n_{qp}/\tau_{eff}$; τ_{eff} is the energy relaxation time defined from the quasiparticle lifetime, τ_{qp}, as $\tau_{eff} = \tau_{qp}/2$. For most MKID materials, τ_{qp} is typically $\mathcal{O}(10\ \mu\mathrm{s})$.[74]

Γ_o is defined from the total absorbed power, $P = \eta_0 P_0$, where η_0 is the optical efficiency of the MKID.[65] It follows that the optical generation rate as it relates to the total number of quasiparticles, $N_{qp} = n_{qp}\Sigma$, is[60]

$$\Gamma_o = \frac{\eta_0 P_0}{\Delta\Sigma}, \tag{3.54}$$

where Σ is the superconducting volume. Using the small signal approximation, Equations 3.53 and 3.54 give

$$\frac{\mathrm{d}n_{qp}}{\mathrm{d}P} \simeq \frac{\eta_0 \tau_{eff}}{\Delta\Sigma}\left(\frac{1}{1 + i\omega\tau_{eff}}\right). \tag{3.55}$$

The result of Equations 3.49, 3.50, and 3.55 give the DC frequency response to optical power for

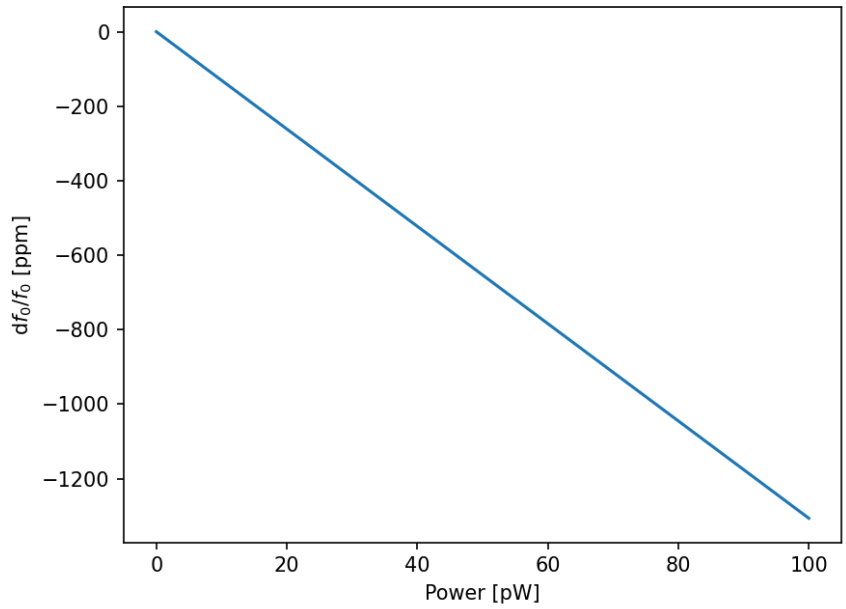

Figure 3.7: Theoretical magnitude of the shift in resonance frequency as a function of absorbed optical power for a TiN MKID in parts per million. The response appears linear over a wide range of absorbed power and shows relatively high sensitivity in the working range as compared to the thermal response.

the case of TiN:

$$R_P = \frac{\alpha f_0}{4N_0\Delta_0}\left(1+\sqrt{\frac{2\Delta_0}{\pi k_B T}}\right)\frac{\eta_0\tau_{eff}}{\Delta\Sigma}. \tag{3.56}$$

The result is proportional to τ_{eff} - and therefore τ_{qp} - and is inversely proportional to Σ, the former of which is a material property, and the latter of which is defined by the physical design of the device. These results emphasize the care that must be taken when designing and fabricating MKIDs in order to achieve the requisite responsivity. A model of the response for a TiN MKID is presented in Figure 3.7, which shows the linear response of an MKID over a wide range of powers. Within the working range of Prime-Cam, which projects $\sim$100 pW of loading,[9] the sensitivity of MKIDs to optical power is far greater than the thermal response at $\sim$100 mK (Figure 3.6).

3.3.3 Sensitivity

The metric used when describing the overall quality of a millimeter/submillimeter detector is the sensitivity, which is characterized by the noise equivalent power (NEP). The formal definition of NEP is the noise power of the system measured after 0.5 seconds of integration time. It can also be

described as the noise power of the system when the SNR is equal to one. Some sources also quote noise equivalent temperature (NET), particularly in radio astronomy.[51] NEP and NET are related by the following relation:

$$NEP = \frac{NET}{k_B B}, \tag{3.57}$$

where B is the bandwidth. The goal of every detector is to be photon noise limited, particularly from the desired source. Care must therefore be taken to ensure that all other sources are minimized such that the system becomes source noise limited. The NEP for a system is the sum of several different sources of noise. These are covered below with the exception of readout noise, which is covered in Chapter 4. The noise sources outlined below are presented in order from most dominant to least dominant. Note that readout noise is typically the least dominant of all relevant noise sources for a well designed system.[74]

3.3.3.1 Photon noise

Photon noise arises due to statistical fluctuations in the photon rate of arrival or photon flux. The result is a Poisson distribution with a square-root relationship between signal and noise ($\varepsilon = \pm\sqrt{N}$ for N collected photons). The NEP for photon noise is defined as[60]

$$\begin{aligned} NEP_\gamma &= \sqrt{2Phf(1+\eta n_0)}, \\ &= \sqrt{2Phf + 2P^2/B}, \end{aligned} \tag{3.58}$$

where $P = \eta n_0 B h f_c$. Here n_0 is the photon occupancy number, B is the bandwidth, and f_c represents the central frequency of the bandwidth. The first term in Equation 3.58 is referred to as *shot noise* and is a result of uncorrelated arrival of photons, and the second term is *wave noise* due to the correlated arrival of photons.

3.3.3.2 Generation - Recombination noise

Even in an steady state, the number of quasiparticles in an MKID fluctuate about a mean value of N_{qp}. The fundamental noise limit of an MKID is set by the generation and recombination (g-r) of quasiparticles which have been excited whether optically or thermally.[60] Noise arises due to the randomness inherent in the g-r process.[76] There are two general cases for the NEP of g-r noise: dark and optically driven g-r noise. Dark g-r assumes that there is no exposure to external optical signals

and is defined as

$$NEP_{gr} = \frac{2\Delta}{\eta}\sqrt{\frac{N_{qp}}{\tau_{qp}}}\frac{1}{\sqrt{1+(2\pi f\tau_{qp})^2}}. \tag{3.59}$$

Under the assumption that the detectors are exposed to an optical signal which dominates quasiparticle generation, NEP for g-r noise then takes the form[65]

$$NEP_{gr} = \frac{2\eta Phf(1+\eta\bar{n}_{ph})}{\sqrt{1+(2\pi f\tau_{qp})^2}}, \tag{3.60}$$

where $\bar{n}_{ph}$ is the mean photon occupation number. This term can be simplified to[77]

$$NEP_{gr} = \sqrt{\frac{4\Delta_0 P}{\eta_{pb}}}, \tag{3.61}$$

where η_{pb} is the efficiency of absorbed photons creating quasiparticles, defined as $\eta_{pb} = q\Delta/hf$. In this case it is clear that the recombination noise is of the same order as the photon shot noise for a given power P. To limit this effect, the system may be operated in the wave noise limit from optical loading.[65]

3.3.3.3 Amplifier noise

Noise in the RF chain is dominated by amplifier noise generated by the first amplifier in the chain after the detectors (more on this in Chapter 4). Inclusion of a low-noise amplifier (LNA) is vital due to the probe tone power being of roughly the same order as the thermal noise power generated at room temperature (1 pW) across a 1 GHz bandwidth. The NEP for amplifier noise is defined as[78]

$$NEP_{amp} = \frac{Q_i Q_c}{Q_r^2}\frac{2\Delta_0 N_{qp}}{\beta(\omega)\eta\tau_{qp}}\sqrt{\frac{k_B T_a}{P_{ro}}}, \tag{3.62}$$

where $\beta(\omega)$ is the response ratio (Equation 3.27), and T_a is the temperature of the amplifier. From Equation 3.62 it clear that NEP^2_{amp} may be reduced by increasing $\beta(\omega)$, P_{ro}, and Q_r.[60,65] For many materials $\beta(\omega)$ is greater than one, indicating a clear advantage to frequency readout,[78] and with well designed MKIDs (high Q_r) the amplifier noise is routinely driven below other sources of noise.[79]

3.3.3.4 Two-Level System noise

Two-level systems (TLS) are caused by dielectric dipoles contained within the dielectric upon which MKIDs are fabricated.[60,80] This is supported by the fact that removing dielectric substrate from the superconducting volume results in a decrease in TLS noise.[81] There are several proposed mechanisms for the cause of TLS fluctuations, including random emission or absorption of phonons and random tunneling of neighboring TLS creating random potential energies for each TLS.[66] Regardless of its cause, TLS is responsible for observable low temperature resonance frequency shift, dissipation, and frequency noise.[69] While the microscopic effects remain unclear, a semi-empirical noise model has been developed for TLS fluctuators which scales with a number of parameters:[82]

$$S_{TLS} = \left(\frac{T^*}{T}\right)^2 \left(\frac{A_c^*}{A_c}\right)^{0.5} \left(\frac{g_c^*}{g_c}\right)^{2.1} \left(\frac{N_0^*}{N_0}\right)^{0.5} \left(\frac{\Sigma^*}{\Sigma}\right)^{0.5} \left(\frac{Q_r}{Q_r^*}\right)^{0.5} \left(\frac{\Delta_0^*}{\Delta_0}\right), \tag{3.63}$$

where A_c is the area of the capacitor, g_c is the gap between the fingers of the interdigitated capacitor (IDC) fingers, and parameters marked with * represent fiducial scaling values. It is clear that to reduce the TLS noise as much as possible, the capacitor area and IDC finger gaps must be as large as possible.[66] It has been experimentally confirmed that TLS noise is due to a resonator's capacitor rather than the inductor.[75] The NEP for TLS noise is defined as

$$NEP_{TLS} = \frac{\sqrt{2S_{TLS}}}{R_x}, \tag{3.64}$$

where R_x can be either the thermal or optical responsivity (R_T or R_P). Due to the many related parameters, the dependence on responsivity, and the use of fiducial values, TLS noise is difficult to predict and is most often found by looking for its signatures, such as noise which scales with power.[65]

3.3.3.5 Total Noise

The overall sensitivity of a detector is defined by the NEP. Total NEP as measured by a detector is the quadrature sum of the noise contributions from the sources described above:

$$NEP_{Tot}^2 = NEP_\gamma^2 + NEP_{gr}^2 + NEP_{amp}^2 + NEP_{TLS}^2. \tag{3.65}$$

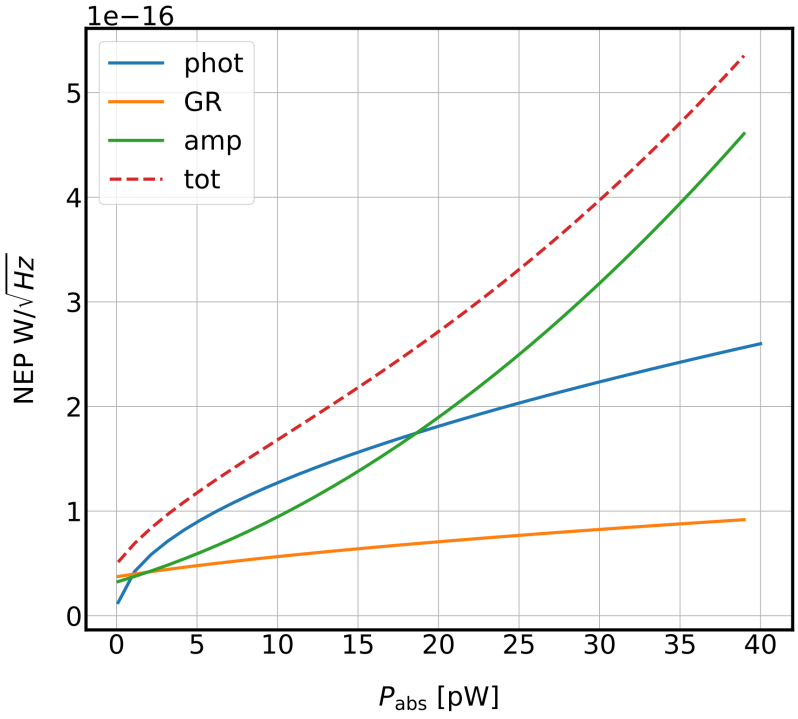

Figure 3.8: Simulated NEP as a function of the absorbed power for total NEP (red, dashed line) and individual noise sources: photon noise (blue), g-r noise (orange), and amplifier noise (green). In the case of g-r noise it is assumed that the detectors are exposed to an optical signal. Image taken from Ref. 74.

The goal in detector design is to be limited in sensitivity by NEP_γ. A diagram showing the typical responses of NEP to increasing power, with the exception of NEP_{TLS}, is presented in Figure 3.8. Strategies to reduce each source of noise has been presented in the preceding sections.

3.4 Conclusion

Chapter 3 discussed the foundations of MKIDs with a focus on derivations and techniques for optimization as they relate specifically to TiN detectors. Sec. 3.2 introduced relevant topics in superconductivity, building towards defining superconducting resonators, crucial for understanding MKIDs. Sec. 3.3 explored the theory behind MKIDs with a focus on responsivity and sensitivity. For the ideal operation of a detector, the noise should be dominated by photon noise. With theory and parameters relevant for MKIDs defined, Chapter 4 will explore the cryogenic testbed used to characterize MKIDs with added emphasis to the readout design.

Chapter 4

A Cryogenic Testbed for MKIDs

I like the cold weather. It means you get work done.

NOAM CHOMSKY

This chapter describes the cryogenic testbed used to test the prototype microwave kinetic inductance detectors (MKIDs). A summary of the cryogenic facility is given in Sec. 4.1. Sec. 4.2 outlines the design specifications, simulations, and assembly of the test box used to characterize the prototype MKIDs. The radio frequency (RF) chain design for the readout is described in Sec. 4.3 with a discussion of the theory. Sec. 4.3 also highlights the design considerations of the RF chain for the Prime-Cam 850 GHz module. The readout design and functionality is presented in Sec. 4.4, including a brief summary on the firmware procedure. This chapter presents the design of a high-performance RF chain. Understanding the response of the RF chain is crucial to extracting the response of the prototype detectors.

4.1 Cryogenic Facility

The cryostat chosen for the work of testing components for the Prime-Cam 850 GHz module is the Bluefors LD250 system.[36] As shown in Figure 4.1, there is a relatively large internal volume with a diameter of 294 mm in the system, which can reach temperatures $<$10 mK. The LD250 system is cooled using a combination of a two stage Cryomech PT415 pulse tube cooler and a dilution fridge. The former cools the system to $\sim$4 K through adiabatic cooling, and the latter involves a more complex mechanism to reach the base temperature. The result is a cryostat capable of achieving ultra-low temperatures in roughly 24 hours when unloaded.

The LD250 system is a commercial unit, and has therefore been designed to reduce thermal loading from radiative transfer and thermal conductance. The current shield design for the cryostat

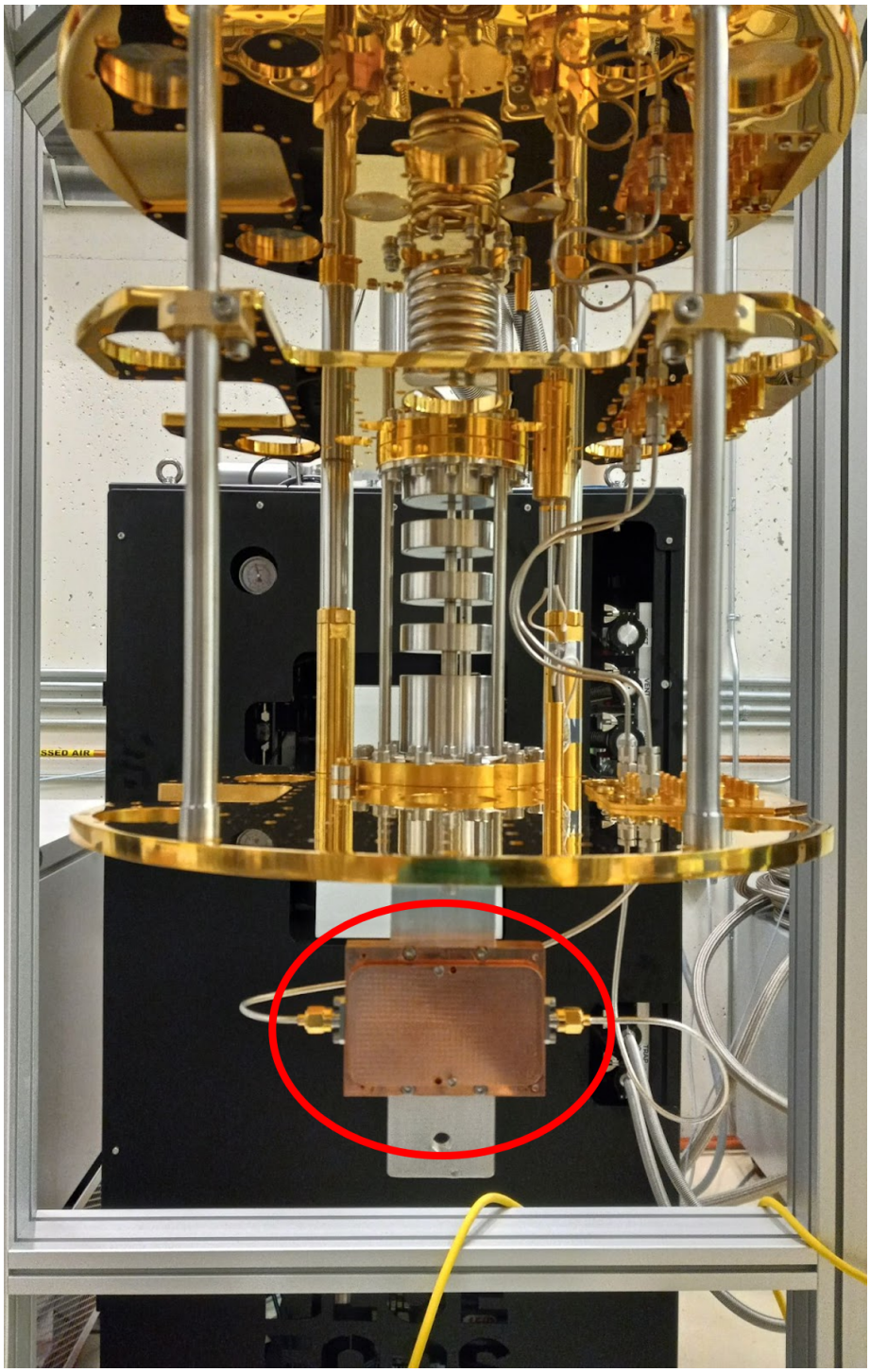

Figure 4.1: Cryogenic stages of the Bluefors LD250 cryostat. The stages from top to bottom are the still flange, cold plate, and mixing chamber flange. The still flange reaches a base temperature of $\sim$1 K, and the mixing chamber flange unloaded reaches temperatures $<$10 mK. In the center of the image is the dilution refrigerator, which allows the system to reach sub-Kelvin temperatures. The experimental volume of the cryostat is underneath the mixing chamber flange. Highlighted is a spare array from the High-resolution Airborne Wideband Camera Plus (HAWC+) instrument on the Stratospheric Observatory for Infrared Astronomy (SOFIA)[45] mounted within the working volume.

lacks any windows, though the system can be retrofit to include a polypropylene window and a combination of thermal infrared and band limiting filters to allow light to be passed from an external source. For convenience, the system includes multiple flange slots and can include up to 77 coaxial cables with SMA connectors. Thus the Bluefors LD250 provides an ideal test environment for MKIDs, all with the push of a button.

4.2 Prototype Test Box

In order to facilitate the development of detector arrays for the 850 GHz module, a test box was developed in collaboration with NIST which could accommodate the requisite test chips, filters, and feedhorn blocks. The test box was designed to accommodate both a preliminary aluminum feedhorn block to aid in rapid testing, as well as a silicon feedhorn block which was designed and fabricated by NIST, the profile of which was characterized by the Quantum Sensor Group in part using the test box. Initially, it was proposed that two separate devices would be designed, one for each type of feedhorn block, though after discussions it was concluded that a single test box could be designed to accommodate both designs. Another important consideration was the feasibility of fabrication of certain complex parts, particularly the aluminum feedhorn block, which resulted in several modifications to the final design.

4.2.1 Specifications

The test box was designed to accommodate a single test chip measuring 10 mm by 10 mm. Such a small size allows for several test chips to be fabricated simultaneously since SOI wafers have a diameter of 6”. The kit is designed to accept two different types of feedhorn: aluminum and silicon. Each of these require different techniques to align them, particularly aluminum due its high thermal contraction. Also necessary are filter holders to define the band for optical testing and considerations for RF coupling, which includes alignment, space, and room for wirebonding to the test chips. The test chip must press firmly against the feedhorn blocks in order to provide adequate thermal contact in order for the prototype MKIDs to reach base temperature, while there must also be an air gap between the two to prevent shorting the detectors to the block.

The aluminum feedhorn block, detailed in depth below, will include both built in alignment pins for the test chips, but also a small air gap etched around the working area of the test ships with a

depth of $\sim$25 μm, though with an accuracy of $\pm$5 μm. This machining accuracy is not truly an issue however since the purpose of the aluminum feedhorns is solely to provide a baseline for optical tests of the prototype chips with a system relatively simple to model. Thus the design allows for an air gap to prevent shorting while also maintaining contact with a significant portion of the test chip for thermalization. The test chip is then aligned with the feedhorns by pressing the chip firmly against the alignment pins. Since the thermal contraction between the silicon and is different, the detectors and feedhorns will appear offset at room temperature.

For the silicon feedhorn blocks, the design is comparatively simple. Since the feedhorns and test wafer are both fabricated from silicon wafers, there are no alignment challenges when cooling. The two components may be aligned and fastened together at room temperature using dowels before being inserted into the test box. Since the silicon feedhorns are metalized and gold-coated, there should be sufficient thermal conduction between the two as compared to the aluminum. In case there are issues thermalizing the wafer, gold pads are included on the test chips to allow extra wirebonding to increase thermal conduction to ensure the prototype detectors reach base temperature. Note that the design, fabrication, and testing of the silicon feedhorns is done by NIST and is not in the scope of this work.

To ensure accurate testing, particularly for low NEP applications, the system must be as light-tight as possible. To achieve this, the test box was dimensioned to allow for relatively tight fit with the feedhorn block with a lip around the circumference. The pieces were designed to be bolted together as well, ensuring firm contact. Additionally, the filter holders were designed to sit directly over the feedhorns, and the oversized sample filters ensure that any light entering the system is within the specified band. As a final precaution, the small gaps between pieces may be covered with aluminum tape.

4.2.2 Feedhorn Block

The feedhorn block represents the most complex portion of the test box. As shown in Figure 4.2, the feedhorn blocks include many features: waveguides, feedhorns, air gap, alignment pins, and slots for sample clips and wire bonds. These features may be categorized to simply the waveguide, feedhorn, and mechanical design. A summary of the simulated optical response of the test box is given in Sec.4.2.2.1.

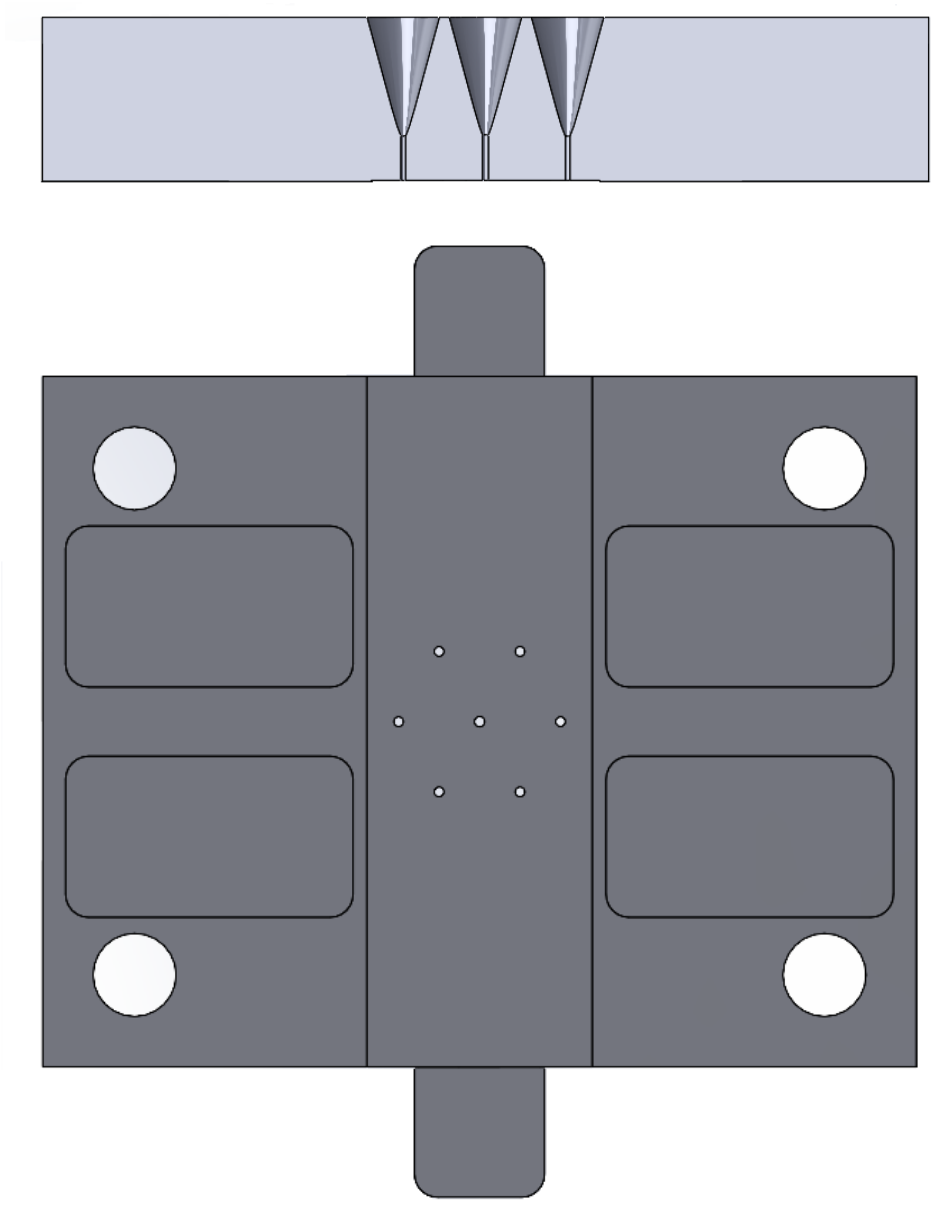

Figure 4.2: Rendering of the aluminum feedhorn block for the test box. Top: Cutaway of the feedhorn block depicting the feedhorn design. The spacing of the feedhorns allows for a large, unobstructed field of view. The feedhorns are conical with an angle of 15°. Bottom: Base of the feedhorn block. The design includes connected alignment pins that will also serve to align the test wafer during tests and a 25 μm air gap strip. The design accommodates the space need to include sample clips for the test chips, and covers the volume used for wire bonding the readout to the test chip, as well as additional bonds for thermal coupling.

To properly characterize the response of the prototype detectors, the optical response of the test box needs to be reasonably constrained and modelled. Analysis of the system begins by defining the passband available for the detectors. The test box is designed to incorporate up to two low-pass FIR filters, which define the high end of the band. For the aluminum feedhorn block, the low end of the band is determined by the waveguide diameter, providing a high-pass filtering mechanism. The cutoff frequency, f_c, for a waveguide is defined as

$$f_c = \frac{1.8412c}{\pi d}, \tag{4.1}$$

where d is the diameter of the waveguide. For $f_c \simeq 800$ GHz, the diameter of the waveguide must be $\sim$220 μm. The ideal length of the waveguide is generally given as 2-3 wavelengths in order to prevent excess losses within the band. For 850 GHz (350 μm), this corresponds to 0.7-1.05 mm. For simplicity, a length of 0.75 mm was chosen for the waveguide, allowing for some machining tolerance to the feedhorn depth with minimal loss across the band. No flare or optical choke is included on the detector side of the waveguide.

The feedhorns were positioned with a pitch of 2.8 mm, roughly twice the pitch planned for the final detector arrays for the 850 GHz module. The purpose is twofold: to ensure as large a feedhorn as possible for optical loading test, and prevent re-machining the feedhorn block should preliminary results show a 1.4 mm pitch is unattainable. Preliminary designs for the feedhorns included a feedhorn angle of 30°. However, due to tool availability and costs for parts the feedhorn angle was reduced to a conservative 15°. The overall impact is a reduced FoV, and therefore throughput, but the feedhorn block remains relatively simple to model.

The simplest portions of the mechanical design include slots to allow space for pins to secure the sample chips to the base and wire bonds. Naturally, these must allow enough space for the feedhorn to still make contact with the test chips. The depth of the air gap, however, required additional thought. While it is relatively simple to provide adequate space for the detector arrays to not be shorted, the feedhorn block also serves as the grounding plane of the system. The effective shunt capacitance of the system impacts both the response of the detector and the line impedance of the microstrip lines on the test chips. Figure 4.3 depicts the relationship between line impedance and air gap depth for two different microstrip lines with widths of 11.5 μm and 16.5 μm. The results

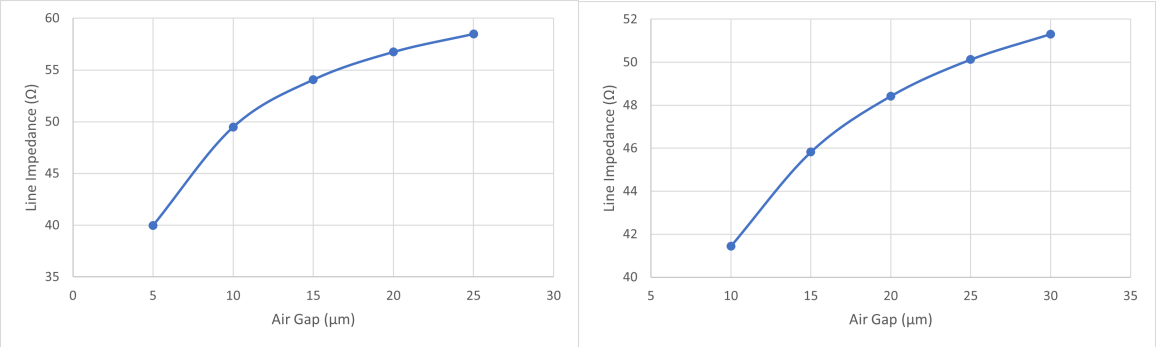

Figure 4.3: Line impedance as a function of air gap for two widths of microstrip lines: 11.5 μm (left) and 16.5 μm (right). The wider stripline shows greater tolerance to deviations in the air gap depth assuming a target line impedance of 50 Ω.

show that wider microstrip lines are more robust to variations in the air gap, a useful feature since the achievable surface tolerance of the air gap recess is ±5 μm. The target line impedance for the microstrip is 50 Ω, and so an air gap of 25 μm was chosen. The surface roughness of the air gap is not a major issue as a tolerancing analysis shows the max variation in the line impedance is ±1.5 Ω, which is insignificant for a preliminary test device. These simulations were performed using the Sonnet software package.[83]

4.2.2.1 Optical Response

Scattering parameters, or S-parameters, are a set of coefficients used to describe the response of an electrical network, particularly for those operating at RF and microwave frequencies. S-parameters are used to relate the magnitude and phase of voltage waves incident to and reflected from network ports.[84] However, S-parameters change with measurement frequency, meaning that characterizing a system requires an analysis of each component across the band of interest; some components may be calculated directly using network analysis, while others require measurement using a vector network analyzer.[85] These results are then cascaded through the system to determine the overall S-parameters, which for a two-port system such as the RF chain design in the 850 GHz module allows for the overall attenuation in a system to be quickly and accurately simulated. In the case of a symmetric system the S-parameters may be summarized in terms of back reflections (S_{11}) and forward transmission (S_{21}). Adding the measured S-parameters for multiple components strengthens a given model's predictive abilities in RF system such as the readout, presented below, factors include cryogenic LNAs, cryoattenuators, and MKIDs, and losses in the coaxial cables.

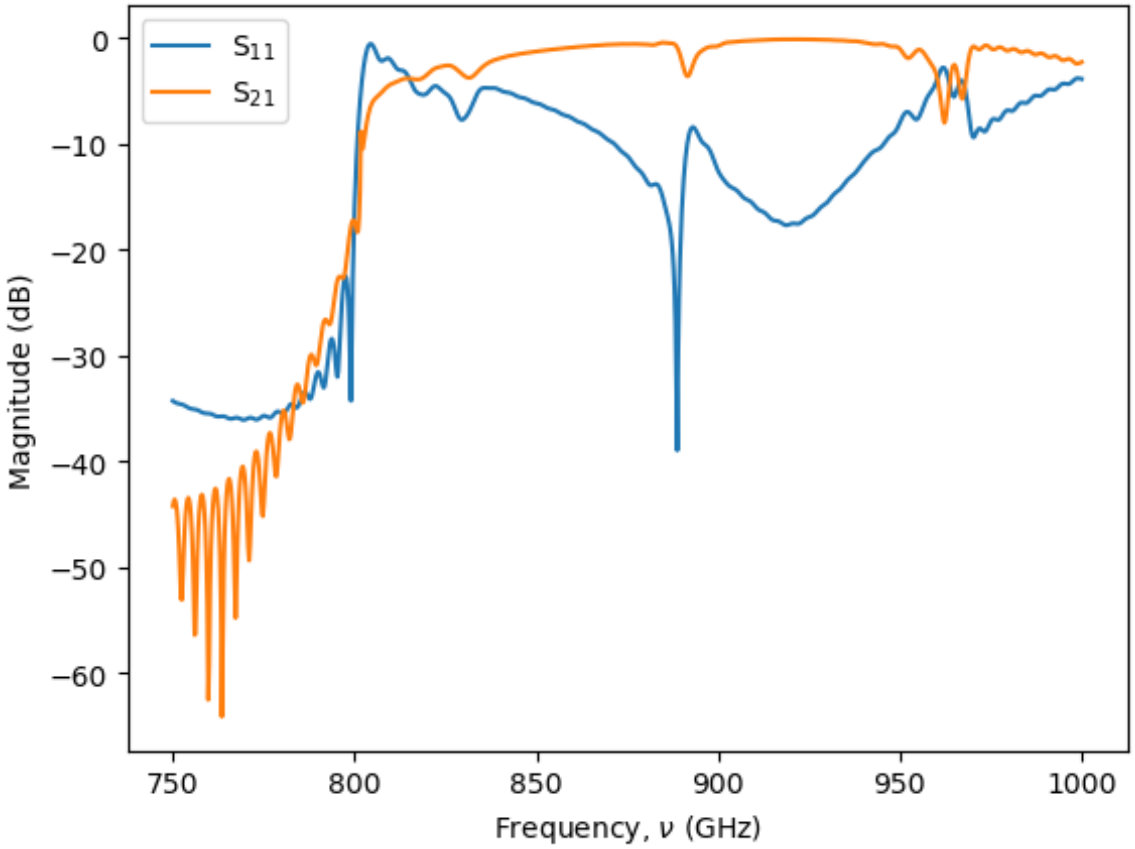

Figure 4.4: Simulated S-Parameters for the test box feedhorns with a Si backshort, open- boundaries with a 25 µm air gap, which best represents the experimental setup using prototype detectors fabricated on SOI wafers.

Simulations on the response of the aluminum feedhorn block were done using CST,[86] the license for which was provided by NRC-HAA. A model of the waveguide, air gap, and a wire port (representing the inductor line of the detector acting as an absorber) over a backshort were generated to represent the experimental setup of a prototype detector fabricated on a silicon-on-insulator (SOI) wafer, which is a wafer with a layered silicon–insulator–silicon substrate. The line impedance for the simulated inductor line was ∼500 Ω, comparable to results from previous experiments using MKIDs, such as BLAST-TNG.[74] Recall that the experimental band of the 850 GHz module is roughly 800-900 GHz. Results of the simulations, presented as S-Parameters in Figure 4.4, show high forward transmission (orange trace) across the bulk of the given band with the exception of a resonance at ∼960 GHz. Resonances, and the magnitude of the back reflection (blue trace) tends to be around the fiducial magnitude of -10 dB. Further simulations confirmed that the resonances are

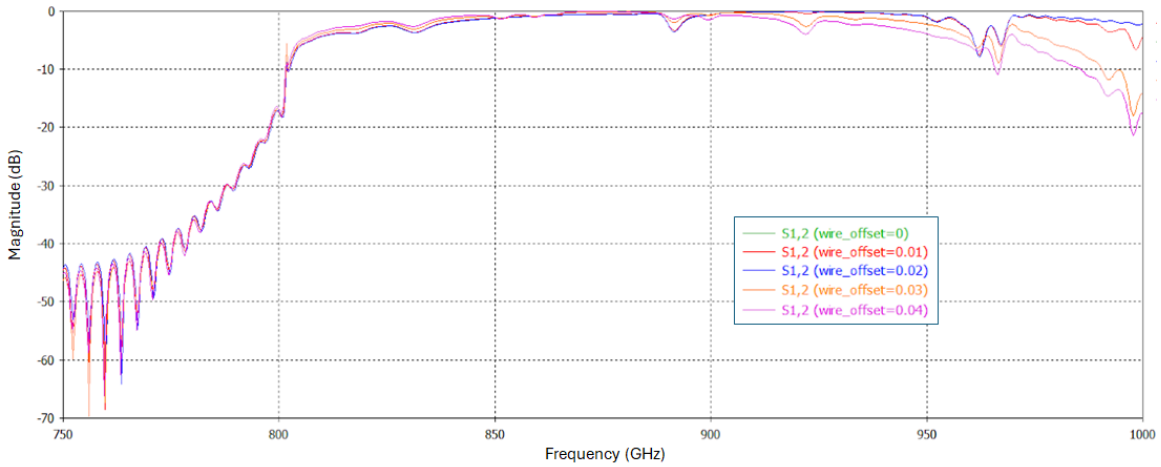

Figure 4.5: Simulated S-Parameters for the test box feedhorns with a linear offset in the discrete port wire, which represents the detector inductor line.

not due to the backshort, but rather could be reduced in magnitude by tuning the impedance of the discrete port. The combination of these results show the feedhorn block is suitable for the purposes of a preliminary device.

One potential issue arising from the design of the aluminum feedhorn block is misalignment between the detectors and waveguides. This is due to the differences in the coefficient of expansion between the aluminum and silicon. At room temperature, the linear displacement between the two is roughly 20 µm. Simulations were performed to test the effect of displacement between the two should the system fail to align during cooldown. The results are shown in Figure 4.5. An offset as high as 40 µm was tested, a worst-case scenario, should the system shift away from alignment during cooldown, all with minimal decrease in transmission across the band. These results confirm that the system is robust to potential misalignment issues.

4.2.3 Assembly

A rendering of the final test box assembly is shown in Figure 4.6. The alignment pins on the feedhorn block also serve as bumpers for the test chips. Slots are included in the base to allow the test chips to be firmly pressed into the alignment pins and allowing for consistency between different trials. Also included in the back is a series of springs designed to push the test chip up into the feedhorn block, ensuring good thermal contact. Figure 4.7 shows the final machined assembly, which includes the filter holder assembly that is positioned over the feedhorn block.

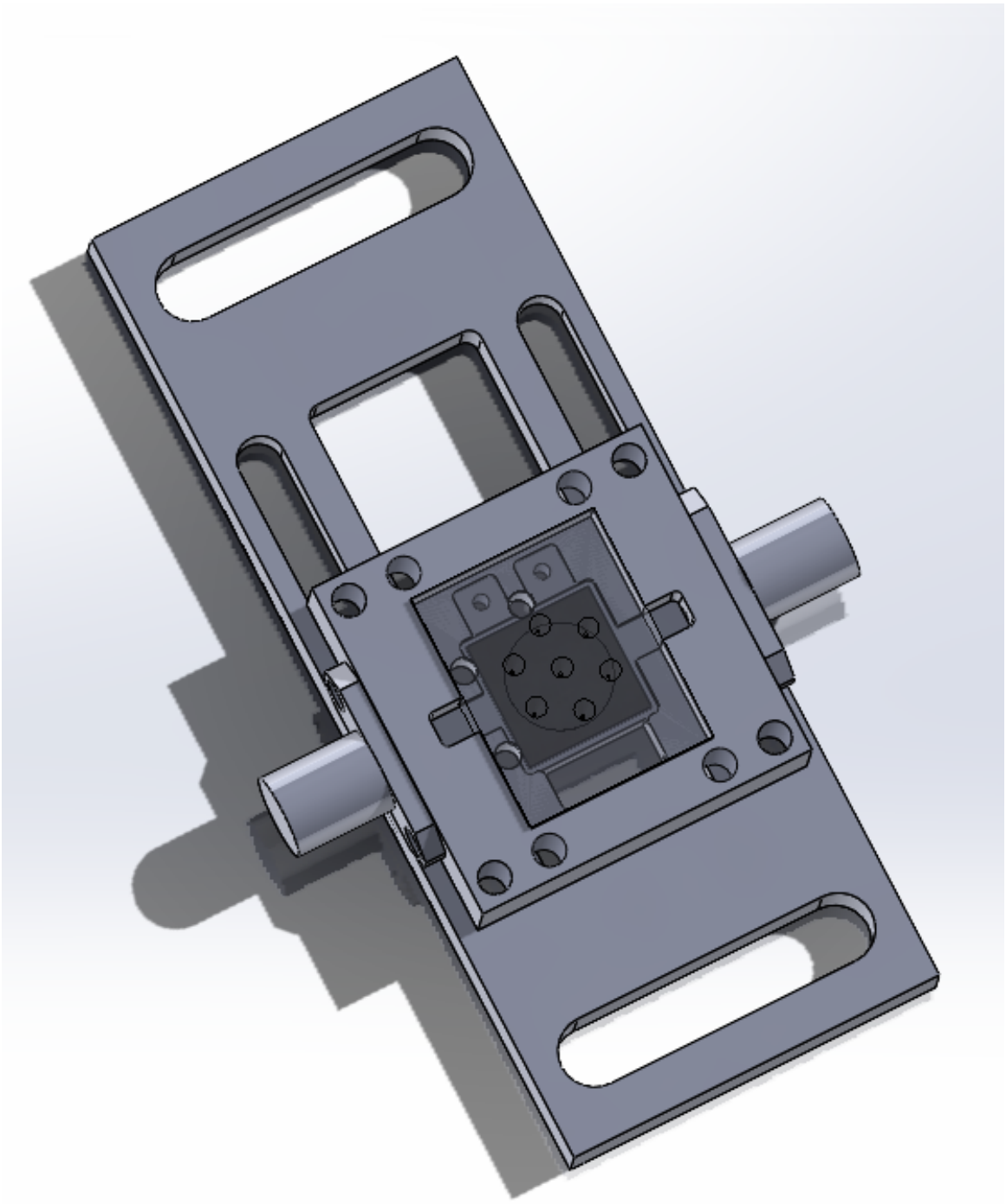

Figure 4.6: Rendering of the assembled test box including coaxial flanges. The system is designed to maintain alignment with thermal contraction in the feedhorn block, and the alignment pins also serve as the bumpers for the test chips. The design includes a 3.5 mm slot to allow one to push the test chips against the alignment pins.

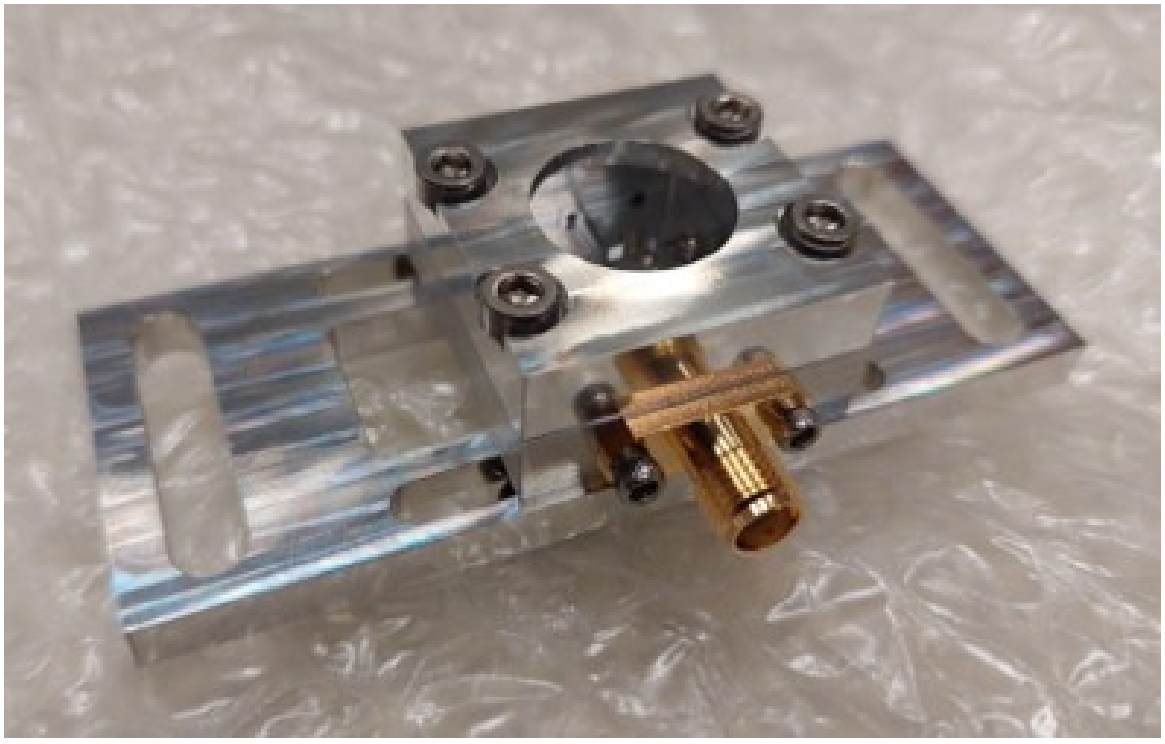

Figure 4.7: Final machined test box assembly. The device allows for up to seven optically-coupled and multiple dark pixels.

4.3 RF Chain Design

The cryogenic testbed for the 850 GHz module is designed to provide a large volume for experiments with several thermally isolated stages with the base stage reaching a temperature below 10 mK in less than 24 hours. Each LD250 unit contains numerous access ports, which are vital for testing kinetic inductance detector (KID) arrays with large RF demands. The cryostat is designed to thermalize the semi-rigid coaxial cables between each of the stages, allowing for a reduction in thermal noise. As can be seen in Figure 4.8, the design for the RF chain as installed in the LD250 system will also incorporate cryogenic attenuators and a cryogenic low noise amplifier (LNA). For the simulations that follow, the system assumes the use of SC-086/50-SS-SS coaxial cables feeding on the input side of the chain, and SC-219/50-CN-CN on the output side.[87] However, in Prime-Cam the 850 GHz module will incorporate flexible stripline based transmission lines.[88] A summary of the RF chain considerations as they relate to the Prime-Cam 850 GHz module is given in Sec. 4.3.4, which also highlights the thermal budget of the system. Understanding the RF chain design is crucial to understanding the performance of the readout.

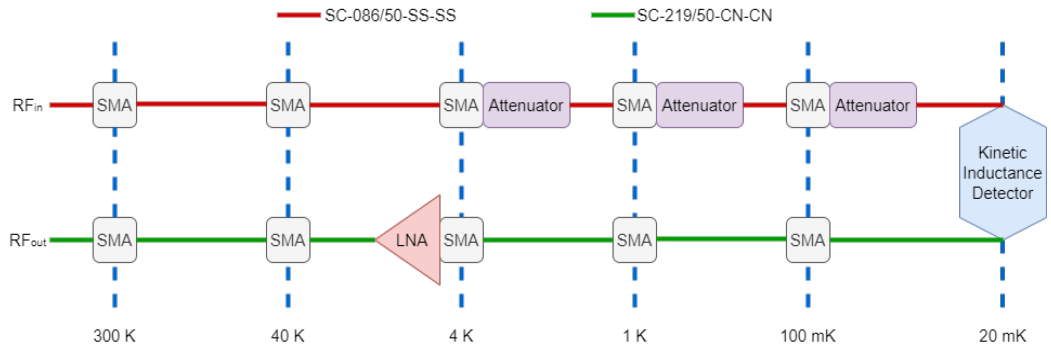

Figure 4.8: Schematic of the RF chain design for the 850 GHz module as it is to be incorporated into the cryogenic testbed. The components will be thermally coupled to the relevant stages to prevent thermal parasitics from reaching the MKID arrays.

Some information presented below has been published in Huber, A. I. et al. "CCAT-prime: optical and cryogenic design of the 850 GHz module for Prime-Cam." In *Millimeter, Submillimeter, and Far-Infrared Detectors and Instrumentation for Astronomy XI*, Proc. SPIE, 2022 (Ref. 25).

4.3.1 Scattering Parameters

The 850 GHz module is designed to introduce as much attenuation as possible (at least 30 dB) before reaching the detector arrays, and as little attenuation as possible onward to the output of the cryostat. Consequently, a series of simulations were performed[89] first using different types of coaxial cables to determine which would be ideal for the system. From this analysis the SC-086/50-SS-SS coaxial cables were selected for the input side of the chain and SC-219/50-CN-CN for the output side as shown in Figure 4.8. Additionally, the simulations included the S-parameters for two MKIDs with resonant frequencies of 1 GHz and 1.001 GHz, with total quality factors of 4,000 and 3,000 respectively and a coupling quality factor of 10,000 for both simulated resonators. The S-parameters were calculated assuming a symmetric system via the method presented in Ref. 90. If provided with the de-embedded S-parameters of the 850 GHz array, they can be fully simulated within this model.

A series of LNAs were explored to examine the attenuation in the RF chain against power dissipation. S-parameters for the LNA were taken from the manufacturers for these simulations. The results, shown in Figure 4.9, highlight these two parameters. Note that the expected band for the readout is approximately 0.3 GHz to 1.3 GHz, a soft constraint set at the low frequency end by current room-temperature filters in the readout. The left panel of Figure 4.9 depicts a system

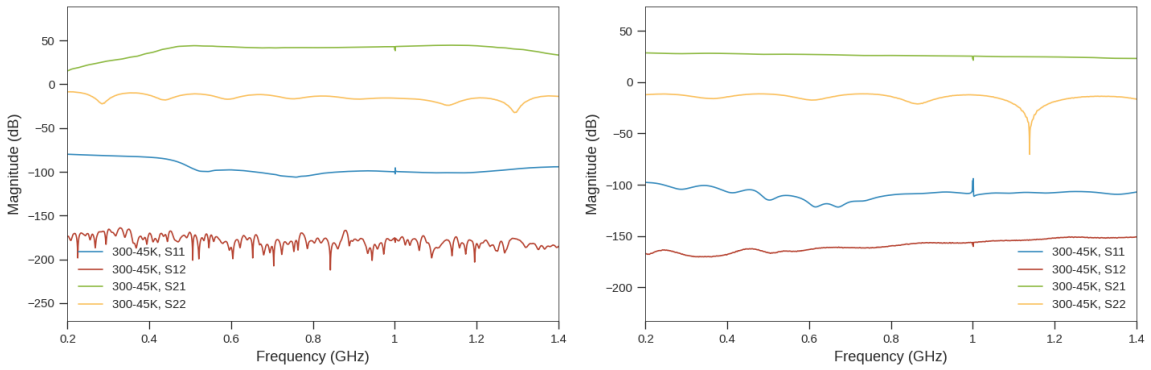

Figure 4.9: Simulated S-parameters through the 850 GHz cryogenic testbed, including detector resonances at both 1 GHz and 1.001 GHz. The simulations considered attenuation in cables, as well as cryogenic attenuators and low noise amplifiers (LNAs), including a room-temperature LNA external to the cryostat. The left panel depicts simulations using a high-gain LNA, while the right panel depicts a low-dissipation LNA.

utilizing a high-gain system operating at the maximum allowable dissipation of 8 mW,[91] while the left panel depicts a system with a dissipation of 5.2 mW;[46] the former reduces but does not eliminate the requirements for signal amplification outside the cryostat, while the latter drastically reduces thermal loading. An additional room-temperature LNA[92] was included prior to being connected to the RFSoC, the justification for which is presented below. These simulations must be compared against in situ measurements before the system can be finalized.

4.3.2 Characterization and Noise

In general, there are three metrics to define in the RF chain components. These are the thermal conduction and dissipation relevant to the thermal budget, S-parameters of the various components within the RF chain, and the equivalent noise temperature of components for the detectors and amplifiers. The proposed experimental procedures for evaluating these metrics are detailed below.

The thermal characteristics of the RF chain are vital as they may determine a possible limit to the number of detectors possible in a given module. There are several contributions to the thermal budget of the Prime-Cam 850 GHz module, which is given in Sec. 4.3.4.2. To characterize the thermal conduction and dissipation of a given system, one must first measure the cooling power of the cryogenic system. The Bluefors LD250 dilution refrigerator includes cryogenic heaters in its installation.[36] By stepping the heaters and allowing the system to settle, a range of cooling values can be obtained across the various stages. In particular, the cooling power from 7-100 mK can

be obtained, which should be well within the operating temperature range once the RF chain is installed. Once the RF chain is installed and before any signal is passed through the system, the base temperature will settle to a value corresponding to a given heater temperature, allowing one to interpolate the thermal conduction of the RF chain. A signal may then be passed into the system, which introduces thermal dissipation into the cryostat from losses in the line. The increase in base temperature then corresponds to the heat introduced by dissipation, and a value can be obtained. A metric of particular interest for the final system is the total thermal load per detector.[18]

S-parameters define the overall frequency response of a given RF component or the overall RF chain itself. Measurements can be taken using a vector network analyzer (VNA), but these must include in the measurements the transmission lines, and any other inline components, which may introduce deviations from the true S-parameters of a given device. There are two major methods to characterize the S-Parameters of a component while eliminating systematic effects, such as those from a VNA used to make the S-parameter measurements: *Thru-Reflect-Line* (TRL) and *Short-Open-Load-Thru* (SOLT).[85] However, the development of a standard load that is functional under

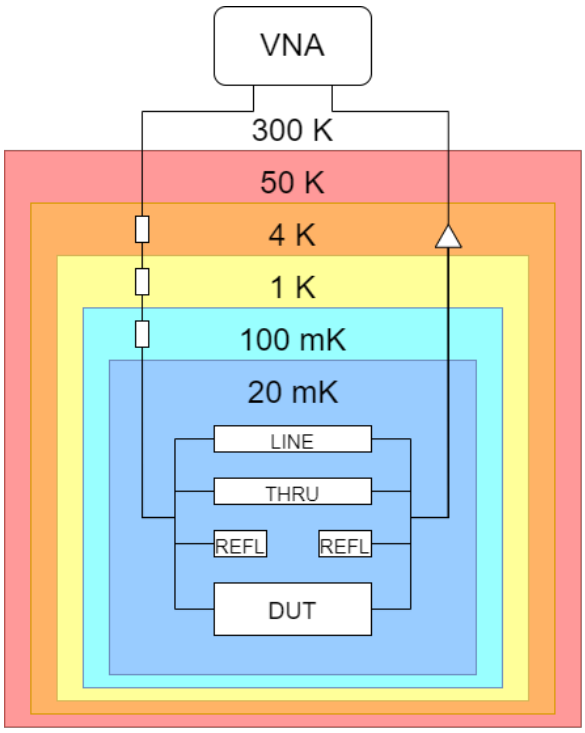

Figure 4.10: High-level diagram of a proposed cryogenic TRL test configuration for measuring S-parameters of RF components, in particular the MKID arrays for the 850 GHZ module of Prime-Cam. This design includes the cryogenic attenuators and LNA as presented in Section 4.3.3.

ultra-low temperatures (mK) - a requirement for the SOLT technique - is difficult and will be imperfect to some degree.[93] Therefore the TRL technique is the more suitable technique for characterizing cryogenic components.

The TRL technique is used to calibrate the network analyzer using three configurations before the device under test (DUT) is inserted and tested. These configurations, given in the name, are defined as follows:[85] The *Thru* configuration connects the two ports together, directly bypassing the DUT. Next, the *Reflect* configuration uses a load with a large reflection coefficient, such as an open or short, before the DUT. Finally, the *Line* configuration is nearly identical to the *Thru* configuration, but incorporates an extra length of matched transmission line. A high-level diagram of the setup for the TRL technique is presented in Figure 4.10.

The effective noise temperature, T_e, is a metric which defines the thermal noise generated by a device and may be used to define the signal-to-noise degradation of a signal.[85] A simple, yet efficient means of calculating T_e is through the *Y-factor method*. The Y-factor method is performed by measuring the (noise) power output of the system with two matched thermal loads at significantly different temperatures. The noise power, N, is defined as the sum of the noise power of the load and the noise power of the DUT:[85]

$$N = GkTB + GkT_eB, \tag{4.2}$$

where G is the gain (also S_{21}), k is the Boltzmann constant, and B is the bandwidth. For using two temperature measurements, T_1 and T_2 where $T_1 > T_2$, The Y-factor is defined as

$$Y = \frac{N1}{N2} = \frac{T_1 + T_e}{T_2 + T_e}. \tag{4.3}$$

The equivalent noise temperature may then be solved through the ratio of the output power measurements and source temperatures:

$$T_e = \frac{T_1 - YT_2}{Y - 1}. \tag{4.4}$$

This method using the Y-factor to find the equivalent noise temperature of a given component based on differences in power between sources can also be used to find the responsivity of the MKID arrays.[51] Other useful metrics for the detectors is an analysis of crosstalk and power spectrum contamination.[48]

4.3.3 Cascaded Noise Temperature

The final step in characterizing the RF chain is an analysis of the noise inputs. The cascaded noise temperature from the output of the detector to the output port of the cryostat (or onward) can be calculated using the Friis formula,

$$T_{cas} = T_{det} + T_{cable1} + \frac{T_{cable2}}{G_{cable1}} + \frac{T_{lna}}{G_{cable1}G_{cable2}} + ..., \tag{4.5}$$

where $G_x = |S_{21}|_x^2$ is the gain of the preceding stage x calculated from its forward transmission scattering parameter. T_{cable1} is the effective noise temperature of the first cable calculated from its loss L and physical temperature as $T_{cable1} = T_{phy}(L-1)$.

In the calculation of the equivalent noise temperature of the cryogenic testbed for the 850 GHz module, an equivalent output noise temperature of 40 K was used for the MKID arrays based on calculations from Ref. 94, using values measured for the BLAST-TNG 850 GHz array.[51] A derivation of this value is given in Ref. 18, and the equivalent noise temperature as calculated across the band of the RF chain in the cryostat with an additional room-temperature amplifier is shown in Figure 4.11. With a baseline detector equivalent noise temperature of 40 K, the added noise from the output of the detector to the output of the room-temperature amplifier is less than 10%.

The equivalent noise temperature of the RFSoCs analog to digital converters can be calculated using the worst-case noise spectral density (NSD) value of -141 dBFS/Hz and full scale input power, P_{FS} = 2 dBm, from.[95] Using these numbers we get,

$$T_{adc} = 10^{(P_{FS}+NSD)/10}/1000/k \approx 10^6 \text{ K} \tag{4.6}$$

where k is Boltzmann's constant. T_{adc} can then be used to determine the total cascaded noise temperature of the total system.

From the cryostat, the signal will be amplified by a room-temperature RF amplifier, such as the ZKL-1R5+ by Mini-Circuits,[92] providing $\sim$ 40 dB of gain and a noise temperature of $\sim$ 300 K. Directly after the amplifier and before the RFSoC ADC, a programmable attenuator with a range of 30 dB will be used to optimize the input power so as to maximize the dynamic range but not saturate the ADC. One can calculate the optimal gain from the full scale input power of the ADC (2 dBm)

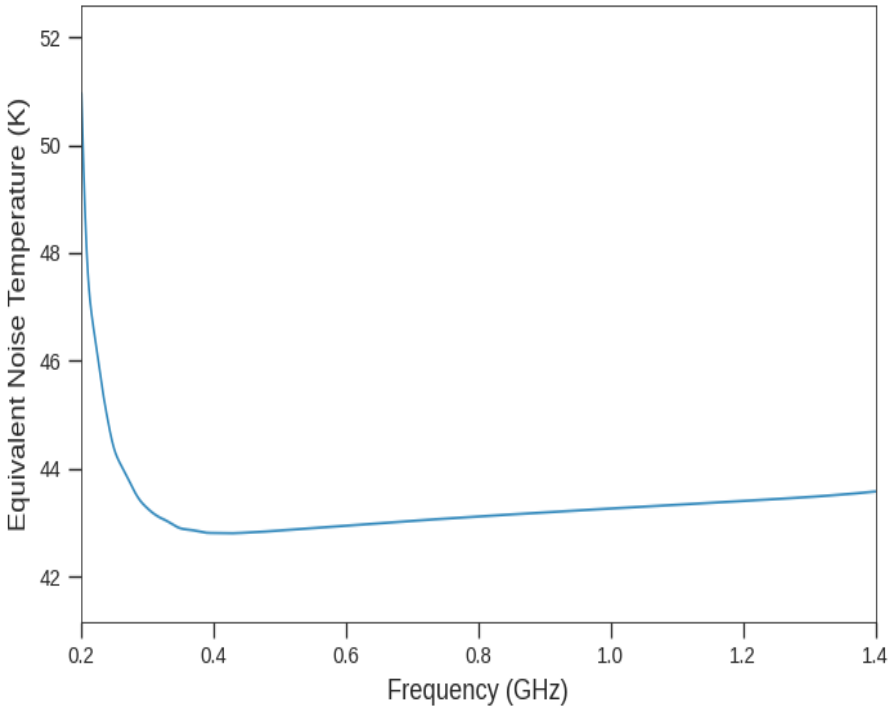

Figure 4.11: Simulated equivalent noise temperature across the detector array readout bandwidth from the cryogenically cooled MKID array to the output of the room-temperature amplifier.[92] The simulation assumes lossy cables and an equivalent output noise temperature of 40 K when on resonance based on values from the BLAST-TNG 850 GHz array.

and the total frequency comb power. A typical detector requires a bias power of -90 dBm[51] and a 1000 tone waveform would give -60 dBm total power at the input to the LNA. The optimal gain can be calculated as,

$$G_{opt} = P_{ADCmax}/P_{comb} \approx 62 \text{ dB}. \tag{4.7}$$

This exceeds the gain of both LNAs in this study and motivates the use of additional gain which can be applied at room temperature. The combination of the ZKL-1R5+ RF amplifier and the following programmable attenuator allows for tuning to the optimal gain.

The total noise temperature including the ADC is represented as

$$T_{tot} = T_{cas} + T_{adc}/G_{opt}, \tag{4.8}$$

where G_{opt} is the optimal gain of the cascade from the input of the LNA to the input of the ADC.

The ratio of the simulated detector noise to the total noise is then given as

$$\frac{T_{det}}{T_{tot}} = \frac{T_{det}}{T_{cas} + T_{adc}/G_{opt}} \approx 0.92. \tag{4.9}$$

Thus the system would add 8% to the total noise in the worst case with the optimal gain. If the 850 GHz detector arrays can be biased at higher powers this number will come down to $<8\%$. The overall system therefore has a maximum noise factor of roughly 0.61 dB.

4.3.4 Prime-Cam 850 GHz Module

The RF chain for the 850 GHz module demands greater cable density than any other Prime-Cam module. To meet this demand, ongoing work is being done to develop and characterize a suitable chain consisting of cryogenic attenuators, LNAs, cabling, and MKID arrays. In tandem there is ongoing work to develop and test a readout system consisting of both hardware and software.[18] Section 4.3.4.1 highlights designs considerations of the baseline RF chain design for the 850 GHz module. In Section 4.3.4.2 the thermal budget for the Prime-Cam 850 GHz module is defined.

It is worth noting that many of the components in the RF chain for the 850 GHz module will operate at at sub-K temperatures, while most components are designed and tested for higher temperature applications (10-300 K).[93] Thus, certain parameters for these components may change for these components as they are incorporated at lower temperatures: components may become superconducting, S-parameters may change, thermal conduction may vary, etc. It therefore becomes critical to test components and explore these parameters at cryogenic temperatures. This leads to the selection of components and the development of an optimized system.

4.3.4.1 RF Design

The designs for the 850 GHz module must strike a balance between minimizing thermal loading to the detector array while simultaneously allowing for the largest number of cables possible. Additionally, the RF chain must be designed such that the system is clearly structured and easy to assemble in situ, the process of which will require careful consideration as to how the plates, shields, and cables will be mounted. The proposed solution to this is the use of cryogenic flexline which will be custom fabricated for the 850 GHz module.

The use of flexline confers several benefits to the RF chain. Flexline has shown to be more

malleable than the default semi-rigid coaxial cabling and is tolerant of cryogenic cycling. Due to the fact that flexline incorporates only a single grounding plane, flexline has been demonstrated to conduct 75% less heat than comparable coaxial cables.[88] Additionally, with a single grounding plane it is possible to mount the requisite cryogenic attenuators inline to reduce the number of connections in the system and minimize the complexity of installing the flexline in the module. Lastly, the inclusion of several (up to 16) channels on a single flexline simplifies the design for the mounting to the magnetic shielding. The potential for developing custom cryogenic flexline has resulted in an ongoing collaboration with CryoElec LLC.[46]

The first prototype has been developed and is shown in Figure 4.12. Preliminary tests have been conducted on the parameters at room temperature, as is common for commercially available flexline, but the components will still require testing - especially at mK temperatures - before the iterative process of development can continue. From the initial analysis of the crosstalk within the flexline in the range of interest for the readout (max 1.3 GHz), the majority of the measured channel isolation was greater than -25 dB. However, further simulations have concluded that in order to achieve channel isolation less than -25 dB, a wider flexline is required to account for increased space between channel. As the grounding plane of the system is copper, this results in a significant increase in thermal conduction across the flexline, which exceeds the limits of the thermal budget. A solution to this is to incorporate a stainless steel grounding plane rather than copper. To date a foundry has not been found that can accommodate the designs of stainless steel flexline, though there is growing interest in the field to do so. In the interim, collaboration with CryoElec LLC has led to designs for ganged, thin-walled coaxial cables to meet the demands of channel isolation required for the 850 GHz module.

4.3.4.2 Thermal Budget

For the cryostat to run as effectively as possible, thermal loading must be kept to a minimum. As the LD250 dilution refrigerator is a commercial unit, care has already been taken in the design to reduce thermal loading from radiative transfer and thermal conductance. However, the inclusion of the RF chain introduces new thermal loading via thermal conductance across the coaxial cables and dissipation from the cryogenic attenuators and LNAs. With more detectors, more cables, attenuators, and LNAs are required. This is the motivation for doubling the readout bandwidth to halve the

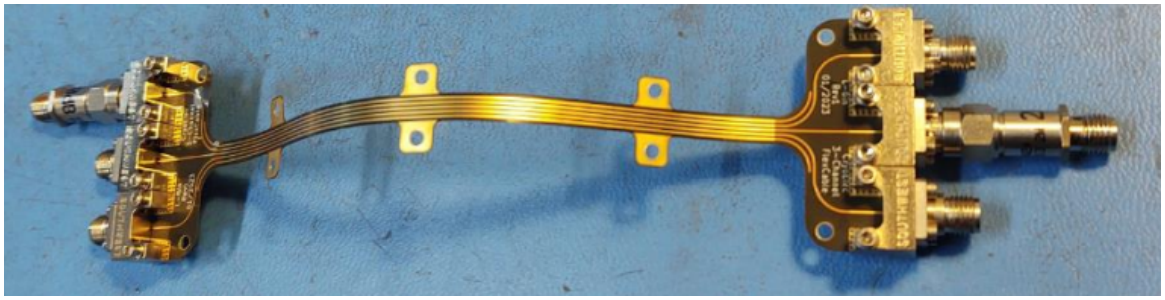

Figure 4.12: Prototype flexline for the 850 GHz module by CryoElec.[46] From the initial analysis of the crosstalk within the flexline in the range of interest for the readout (max 1.3 GHz), the majority of the measured channel isolation was greater than -25 dB.

Table 4.1: Comparison of the predicted thermal loading for RF chain components in the 850 GHz module compared with the overall thermal budget at each stage based on preliminary values for Prime-Cam.

Stage/Component	Thermal Loading	Thermal Budget
40 K Coax	0.278 W	12.57 W
4 K Coax	7.68 mW	457.14 mW
4 K Attenuator	0.008 mW	
4 K LNA	288 mW	
1 K Coax	0.0401 mW	1.71 mW
1 K Attenuator	0.0002 mW	
100 mK Coax	1.93 μW	45.71 μW
100 mK Attenuator	0.0206 μW	
20 mK Coax	0.0328 μW	$\sim$14 μW

required hardware for a given detector array.[18]

From the current optical design, the 850 GHz module is proposed to include 45,000 MKIDs across three wafer arrays, the details of which are given in Chapter 5. Assuming the readout bandwidth is doubled, the 850 GHz module will require roughly 10 Radio Frequency System-on-Chip (RFSoC) boards,[96] 40 cryogenic LNAs, 120 cryoattenuators, and 80 transmission lines. A rough thermal budget for implementation in Prime-Cam is used based on a preliminary analysis of the instrument as these constraints are tighter than those of the LD250 testbed. For the cryoattenuators, the thermal budget and subsequent analyses assume attenuation values of 23 dB, 10 dB, and 3 dB for the 4 K, 1 K, and 100 mK stages respectively. Additionally, the maximum dissipation per LNA was set to 8 mW. A comparison of the thermal loading introduced by the RF chain with the preliminary

thermal budget is shown in Table 4.1. While the thermal loading for all components are within the constraints of the thermal budget, the results emphasize the importance of doubling the bandwidth to halve the requisite number of LNAs. Without this key development in the RF readout, the detector count would need to be reduced to roughly 30,000 MKIDs so that dissipation from the LNAs would fall within the thermal budget for the 4 K stage.

4.4 Readout

Due to the flexibility in resonance frequency and simplicity in their design, MKIDs have always been easily multiplexed.[60,71] Multiplexing requires that each resonator have different resonance frequencies and high quality factors (narrow resonances). As will be shown below, absorption of power, whether optical or thermal, results in a reduction in both the resonance frequency and Q_r. Each MKID therefore requires sufficient bandwidth to accommodate these shifts without colliding with other resonators.[97] The requirements to read out MKIDs is complex, but has the advantage of consisting predominantly of room-temperature electronics with only a handful of cryogenic components.[98,99] Each resonator is monitored by a single probe tone, which returns information on deviations of the resonator from the resonance frequency. It follows that for an array of frequency separated MKIDs, a frequency comb is required to monitor all the resonators simultaneously.

Following the derivation of Sinclair,[51] the frequency comb is derived from a spectrum defined as

$$X(\omega) = \sum_{k=0}^{N} A_k e^{i\theta_k} \delta(\omega_k), \tag{4.10}$$

where A_k and θ_k are the amplitudes and phases. To ensure a maximum signal-to-noise ratio (SNR), the largest possible carrier amplitude must be used without overwhelming the range of the electronics, particularly the digital-to-analog converter (DAC), meaning the crest factor (defined as the ratio between the peak amplitude and RMS amplitude of the signal) must be minimized.[97] In Equation 4.10, A_k represents amplitude correction for a transfer functions, and θ_k is randomized to minimize the crest factor. Since real-world data are discrete and not continuous, Equation 4.10 must be realized in terms of the discrete inverse Fourier transform:

$$f(t) = \sum_{p=0}^{N} F(\omega_p) e^{i\omega_p t}, \tag{4.11}$$

Where $F(\omega_p)$ is the spectrum to be transformed. Combining Equations 4.10 and 4.11 results in

$$\begin{aligned} x(t) &= \sum_{p=0}^{N}\sum_{k=0}^{N} A_k e^{i\theta_k}\delta(\omega_k)e^{i\omega_p t}, \\ &= \sum_{k=0}^{N} A_k e^{i(\theta_k-\omega_k)}. \end{aligned} \tag{4.12}$$

This complex sum of sinusoids, which match the frequencies of the resonators, can then be incorporated into the readout firmware as:

$$I(t)+iQ(t) = \mathfrak{Re}\{x(t)\}+i\mathfrak{Im}\{x(t)\}. \tag{4.13}$$

With the frequency comb generated, the firmware may then be used to readout the resonators. In general, the phase, $\phi(t)$, is used to characterize the system rather than the frequency as it provides a better SNR:[74, 100]

$$\phi(t) = \tan^{-1}\left(\frac{Q(t)}{I(t)}\right). \tag{4.14}$$

4.4.1 Firmware Procedure

The basic framework of the firmware procedure is presented here to highlight the complexity of the readout design. For full details of the readout, the reader is directed to Sinclair (Ref. 51) and Gordon (Ref. 74). Once the probe tones have been defined in the software and firmware as outlined above for each resonator, the detectors are monitored via the following steps:[74]

1. Generate frequency comb with DAC.
2. Digitally upconvert frequency comb to radio frequency (RF) band and pass to detectors.[18]
3. Receive detector-modulated frequency comb. Attenuators, amplifiers, and/or filters may be incorporated in readout chain.
4. Digitally downconvert modulated frequency comb to baseband.[18]
5. Digitize and analyze frequency comb with polyphase filterbank/Fourier transform.[20]
6. Digitally demodulate each channel.
7. Accumulate each signal and downsample to desired readout rate.
8. Packetize I and Q for each channel.

Once packetized, the data is streamed to network and the timestreams are used to interpret

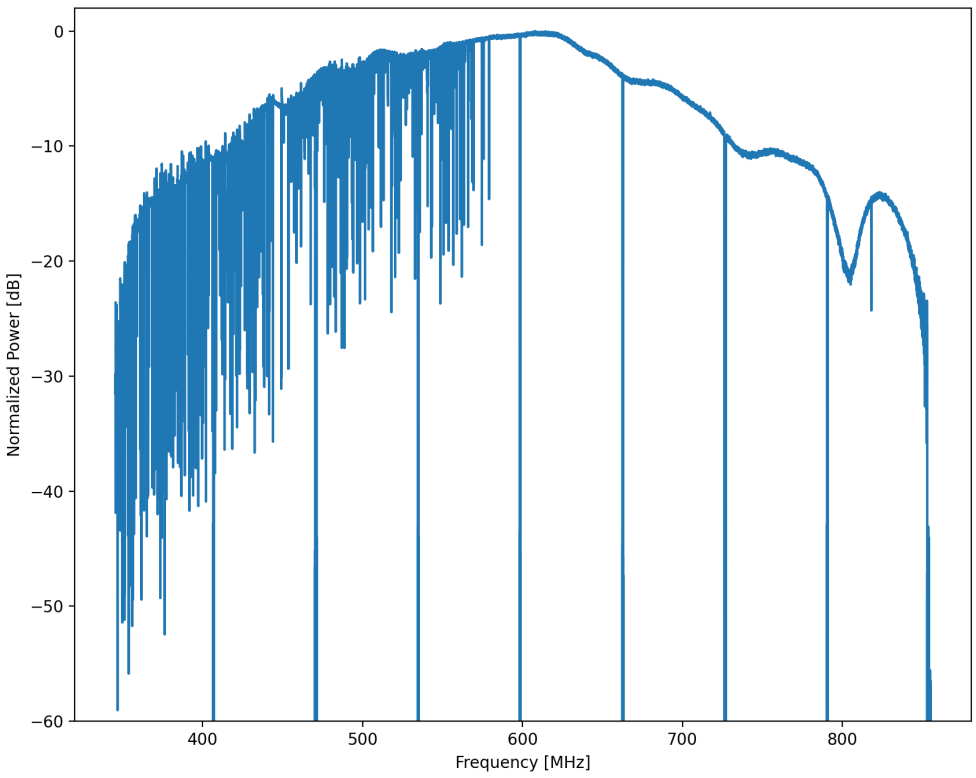

Figure 4.13: First light results in the cryogenic test facility showing a multi-detector sweep on a sample detector package using the RFSoC design. Of the 287 resonators the algorithm found in the first pass, almost all were valid detectors. The MKID array were spares from the High-resolution Airborne Wideband Camera Plus (HAWC+) instrument on the Stratospheric Observatory for Infrared Astronomy (SOFIA). See Ref. 45.

the response of each resonator and converted to absorbed power. The proposed architecture for the 850 GHz readout will incorporate 1,024 MHz of RF bandwidth with detector noise-limited performance.[19] The bandwidth of the readout will be sufficient to support up to 2,048 detectors, providing a multi-octave readout system with a readout bandwidth of ∼500 Hz, comparable to previous readout systems.[74,98] Ongoing work in the field of MKID readout is pushing to surpass a two-octave readout in favour of a scalable multi-octave readout.[20] Note that both firmware and data processing for MKID readout require intricate software control.[21] First light results using the novel RFSoC system[96] are shown in Figure 4.13, marking a major milestone in the development of the readout system.

4.5 Conclusion

Chapter 4 presented the cryogenic test bed for characterizing prototype MKIDs, touching briefly on considerations for the final 850 GHz module. A description of the Bluefors LD250 cryostat was given in Sec. 4.1, outlining key aspects required for tests. Sec. 4.2 details the specifications and designs test box for characterizing the prototype test chips. The test box will allow for both optical and dark testing of prototype detectors. The details of the RF chain design for the experimental setup are given in Sec. 4.3, with ongoing work on the RF design for the 850 GHz module presented in Sec. 4.3.4. Sec. 4.4 summarizes the readout design and functionality, including the firmware procedure, and presents first results from a sample array. With the test kit and experimental setup defined, Chapter 5 explores the design and initial results from prototype MKIDs developed for the Prime-Cam 850 GHz module.

Chapter 5

Design and Characterization of Prototype 850 GHz MKIDs

Science is magic that works.

KURT VONNEGUT

Among the instrument modules being developed for the Prime-Cam receiver, the highest frequency 850 GHz module presents unique challenges in optical design, coupling, detection, and readout. The 850 GHz module will incorporate approximately 45,000 polarization-sensitive, lumped-element microwave kinetic inductance detectors (KIDs), which will represent the most KIDs on sky in a single instrument to date. Chapter 5 presents the critical aspects of the detector design and discusses solutions to the challenges of efficient optical coupling and a multi-octave readout band. Specifically, the designs (discussed in Sec. 5.2) will include a feature which reduces the inductance across a portion of the detectors by shorting pairs of inductor lines to allow the KIDs to be tuned across four distinct bands across the readout range, all with minimal impact to the responsivity of the detector. The resonators are coarsely tuned via the inductance shorts, and finely tuned by etching away small portions of the interdigital capacitors (IDCs). In Sec. 5.3.1, a comparison between simulations and preliminary results of thermal responsivity for TiN MKIDs is presented. Prototype 850 GHz MKID designs are shown in Sec. 5.4; the characterization of the prototype MKIDs is presented and discussed in Sec. 5.5. The results of this work directly inform the design of MKIDs for the multi-octave readout architecture as part of the development of densely packed arrays for the Prime-Cam instrument.

5.1 Introduction

The proposed design of Prime-Cam will include roughly 70,000 MKIDs; of that number, roughly 45,000 MKIDs will be used for the 850 GHz instrument module, which represents the most MKIDs on a single instrument module to date in the mid-infrared regime and beyond. This presents unique challenges in designing and implementing these densely packed arrays.

The baseline readout design for MKIDs used on other facilities to date is 500 detectors/line,[18] meaning that 45,000 detectors require 180 coaxial cables and 90 cryogenic low noise amplifiers (LNAs). A single board handles up to four channels, meaning 23 Xilinx Radio Frequency System on a Chip (RFSoC) boards minimum are required. These exceptional hardware requirements can easily overwhelm both a fiscal and thermal budget. To this end has the 850 GHz module team undergone extensive work into expanding the readout to handle two[19] or more[20] octaves of readout (doubling or even tripling the number of detectors read) in a single channel with a minimum goal of halving the cryogenic radio frequency (RF) design.

Beyond hardware challenges are extensive software challenges. A single RFSoC will transmit data at a rate of roughly 128 Gb/s: an enormous data rate. Furthermore, control of each RFSoC with optimized tone powers and tuning for each detector is required in short time frames for rapid re-calibration of detectors, with overall integration with the facility control software as a whole. The software developed to achieve the ambitious detector count in the 850 GHz array is currently undergoing demonstrations on other modules.[21]

The advances in the hardware and software associated with the readout enable the development of tightly packed arrays of far-infrared (FIR) MKIDs. While MKIDs are not the solution to every astronomical inquiry, this work aims to push the ability of future instruments to include incredibly dense arrays of MKIDs with sensitivities suitable for the Cerro Chajnantor site, with potential applications to balloon-borne instruments, other FIR modules, industry, and fields such as quantum computing. With the development of state-of-the-art RFSoC-based readout, we are able to accommodate this immense number of pixels with less hardware overhead. Combined with the ease of fabrication for MKIDs, this makes future MKID arrays suitable candidates for low cost instrumentation. What follows below is the latest developments towards the design and fabrication of the most densely-packed far-infrared lumped element MKID array for the 850 GHz polarimeter, which will include more MKIDs than any other terrestrial FIR instrument to date.

Many of the details in Sec. 5.2 and 5.3 have been published in Huber, A. I. et al. "CCAT: design and performance of densely packed, high-frequency, dual-polarization kinetic inductance detectors for the Prime-Cam 850 GHz module." In *Millimeter, Submillimeter, and Far-Infrared Detectors and Instrumentation for Astronomy XII*, Proc. SPIE, 2024 (Ref. 101).

5.2 Kinetic Inductance Detector Design

This work is limited to lumped element kinetic inductance detectors - which is to say the individual components relevant for defining the performance of kinetic inductance are discrete and spatially separate from other components. These components are in the internal capacitor, inductor, and coupling capacitor. Furthermore, while aluminum with meanders has been used for other modules for various performance advantages, particularly $1/f$ noise,[102] the volume required to meet our higher loading specifications while maintaining ideal optical coupling is impossible. For this reason the designs and assumptions for simulations are limited to Titanium Nitride (TiN). Lastly, as the 850 GHz module is a polarimeter two detectors are required per pixel, one for each polarization.

5.2.1 Resonator Design

The primary challenge of the 850 GHz detector array is the tight-packing of the detectors on the focal plane. This requirement demands that the design is mindful of pixel size and the detector footprint is minimized while maintaining performance comparable to other modules. A standard MKID design, shown in Fig 5.1, shows that the capacitors occupy a large portion of the overall MKID footprint. As the resonance is inversely proportional to $\sqrt{L_{Tot}C}$, where L_{Tot} is the total inductance and C is the capacitance, we see that to reduce the size of the capacitor, that of the inductor must increase.

One parameter considered in the designs is the film thickness of the TiN due to its direct effect on the resistance and sheet inductance of the resonator. As the film deposition thickness increases, the resistance, which determines optical coupling, decreases and the sheet kinetic inductance increases. As shown in Fig 5.2, using the different thickness and line widths, the ratio of active inductance (absorber) to dark inductance can be modified and tuned to optimize the resonator design. Since aluminum has far lower kinetic inductance than TiN, aluminum shorts can be included in the inductor line to further explore the variability between optically active and dark inductance.

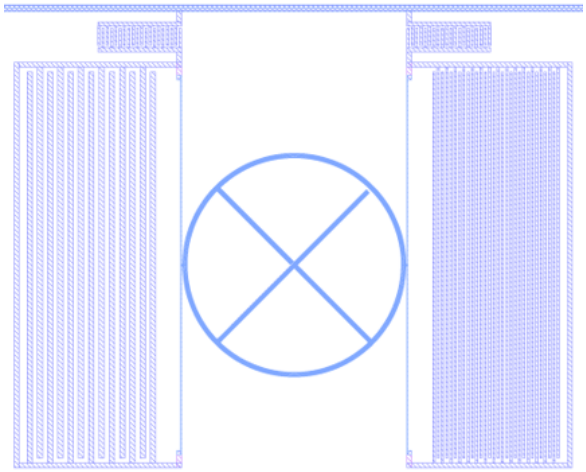

Figure 5.1: Design of a prototype 850 GHz pixel consisting of two orthogonal kinetic inductance detectors. It is clear that the interdigitated capacitors form the majority of the overall footprint.

Recall from Chapter 3 that the thermal and optical responsivity of TiN MKIDs are:

$$\frac{\mathrm{d}f_0}{\mathrm{d}T} = \frac{\alpha f_0 e^{-\Delta_0/k_B T}}{T}\sqrt{\frac{2\pi k_B T}{\Delta_0}}\left(1+\frac{\Delta_0}{k_B T}\right)\left(1+\sqrt{\frac{2\Delta_0}{\pi k_B T}}e^{-\xi}I_0(\xi)\right), \tag{5.1}$$

and

$$\frac{\mathrm{d}f_0}{\mathrm{d}P_{abs}} \simeq \frac{\alpha f_0}{2N_0\Delta_0}\left(1+\sqrt{\frac{2\Delta_0}{\pi k_B T}}\right)\frac{\eta\tau_{eff}}{\Sigma}, \tag{5.2}$$

respectively. In these equations $\alpha = L_K/L_{Tot}$ is the kinetic inductance fraction, $\Delta_0 = 1.764 k_B T_c$ is the binding energy for a single electron, and $\xi = \hbar\omega/2k_B T$ is the coherence length, N_0 is the material-dependent single spin density of states at the Fermi energy, η is the internal quasiparticle generation efficiency, τ_{eff} is the energy relaxation time, and Σ is the superconducting volume in the detector. Thus the optimization of a kinetic inductance detector depends on a handful of parameters, many of which are material dependent. These are Δ, $\mathcal{L}_K$, τ_{qp}, N_0, f_0, and α, which depends on the physical dimensions of the inductor.[103]

The 850 GHz module will experience relatively high loading during operation. It can be seen from Equation 5.2 that $\mathrm{d}f_0/\mathrm{d}P_{abs} \propto 1/\Sigma$, meaning the effect of loading on the responsivity can be suppressed by increasing the superconducting volume. This may take the form of increasing the line widths of the inductor lines, since kinetic inductance is proportional to the number of squares, or increasing the film thickness. Here the balance must then be struck between the appropriate value of inductance and film thickness. A typical TiN film used for MKID fabrication consists of a TiN

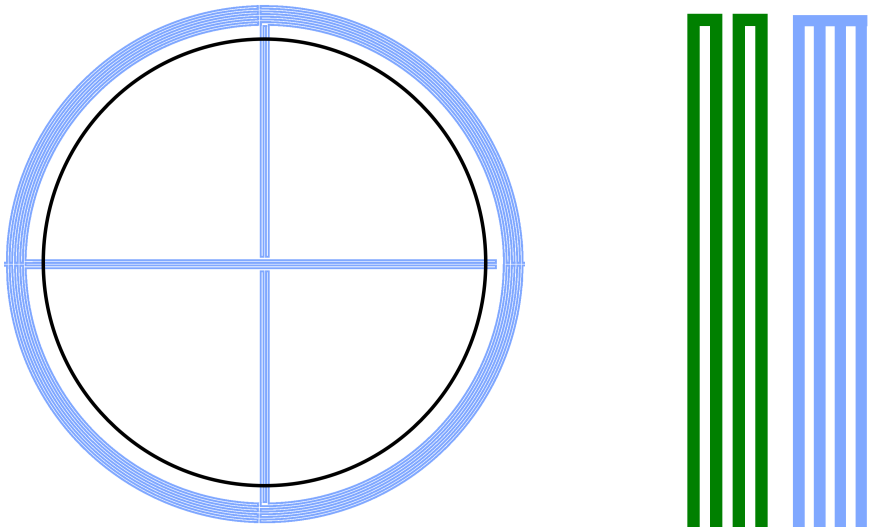

Figure 5.2: Left: Sample inductor design for for two polarization-sensitive kinetic inductance detectors in a single pixel. The area under the feedhorn is denoted by the black circle. Each inductor consists of dark inductance around the arc (defining the circular shape) and optically active inductor (seen as the "crosshair"). The directions of the optically active inductor lines determine the polarization sensitivity of the detectors. Right: Sample designs of non-shorted (green) and shorted (blue) inductor lines.

layer sandwiched between two layers of Ti, known as a trilayer film; this work explores a pentalayer design which will allow for a smaller footprint and increased volume while maintaining the desired responsivity and impedance matching. Optimizations are done using finite element simulations using a parameterized model.[104]

5.2.2 Shorting Inductor Lines

Simplistically, the inductors in MKIDs are a series of lines tracing back and forth, with kinetic inductance being proportional to the number of squares, which implies thinner lines provide greater inductance. A typical inductor (Fig 5.2) consists of dark inductance around the arcs - giving it a circular shape - and optically active inductance under the feedhorn - seen as a cross-hair shape. The direction of the lines of the optically active inductor determine the polarization sensitivity of the detectors, and is where considerations of cross-polarization, the absorption of one polarization by an orthogonal detector, is taken into consideration. The total inductance of the resonator, L_{Tot}, is divided into geometric inductance, which is determined by the physical shape of the inductor, and kinetic inductance, which is determined by the material properties of the superconducting material. For MKIDs, the ratio $\alpha = L_K/L_{Tot}$ should be maximized for optimal performance.

Once a higher inductance resonator design has been achieved, there remains an issue of achieving the requisite frequency schedule. Preliminary simulations of the design showed that the reduced size of the capacitors coupled with the high inductance of the resonators meant that varying the fingers of the IDCs to tune the resonance frequency was insufficient to achieve two-octave performance; the high inductance limits the range of frequencies achievable by tuning the capacitors. To reduce the inductance a technique was developed to reduce the inductance in a detector by shorting pairs of inductor lines, which allows for a two-octave design.

Shorting inductor lines means coupling adjacent lines into bundles. Lines which are shorted together provide the same optical coupling, but results in a decreased kinetic inductance as the effective number of squares has decreased. When N lines are shorted together, the result is a decrease in the kinetic inductance proportional to $1/N^2$. Since $f_0 = 1/\sqrt{L_{Tot}C}$, it follows that shorting inductor lines results in $f_0 = N/\sqrt{L_{Tot0}C}$, where L_{Tot0} is the total inductance of the non-shorted inductor. Note, however, that the geometric inductance of the detector is not impacted by shorting detectors, meaning that it is crucial for α to be maximized when shorting inductors, else the impact of shorting inductor lines will be diminished. To achieve this same effect using strictly capacitors would require a factor of 16 change in the capacitance and so far appears to be quite impossible based on our simulations. This is further complicated when including sources of parasitic capacitance.

Key advantages to the technique of shorting inductor lines are ease of design and editing. Rather than redesigning inductors to couple with light adequately with a lower inductance, a few lines in the design software shift already existing lines in the design to short the inductors with minimal effect to their overall performance. Additionally, there is no significant change to the superconducting volume, meaning the responsivity and optical coupling efficiency of the detectors are preserved, as shown in Figure 5.3.

5.2.3 Array Design

Recall from above that the 850 GHz polarimeter is intended to have the highest possible mapping speed while maintaining image quality. Any optical design that we are able to make that achieves the requisite 1.3° field of view requires more lenses, meaning additional losses in optical throughput due to reflection and absorption. Using a four-lens design we are able to achieve a high-Strehl across 1.1° field of view, providing better image quality and field of view than the default three-lens

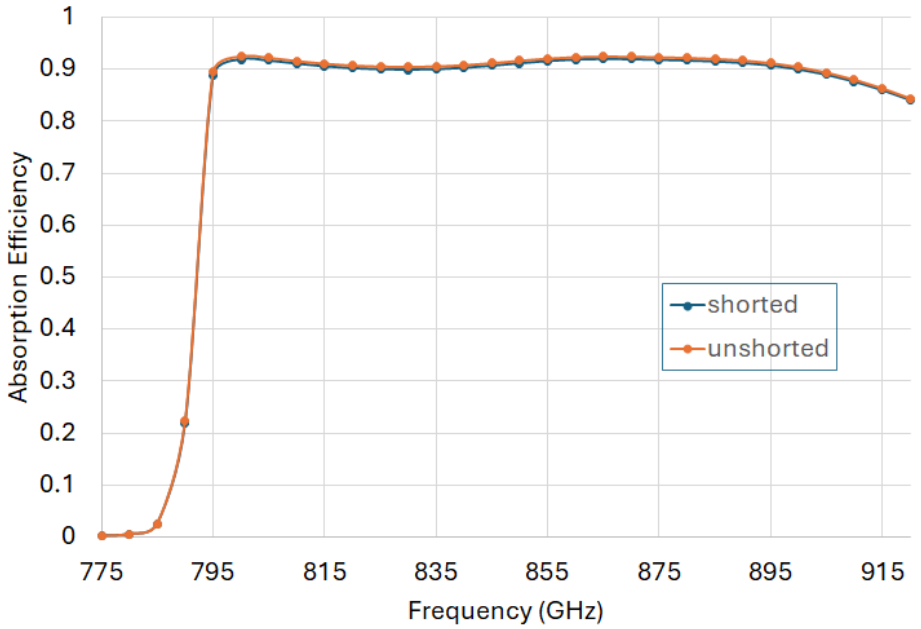

Figure 5.3: Simulations of the absorption efficiency for MKIDs which are either shorted (blue) or unshorted (orange). The roughly half percent deviations between the two are around the repeat accuracy of the simulation software and may be the result of differences in meshing.

design used by Simons Observatory and other CCAT polarimeter modules. To compensate for the reduced FoV, the detector count on the focal plan is being maximized to increase the mapping speed. Specifics on the optical design are given in Chapter 2.

The technique of shorting the inductors provides a means to reduce the inductance by a factor of N^2. For this work, only two lines are shorted together at a time, meaning resonators will have kinetic inductance values of L_K and $L_K/4$ for non-shorted and shorted inductors respectively. This allows for a coarse tuning of the resonators across the readout bandwidth by having the inductor lines shorted or unshorted, and then finely tune the resonators via the interdigitated capacitors. This process allows for the resonators to be much smaller than they would need to be for lower frequency designs, enabling the tight pixel pitch required for the 850 GHz module. Since the internal quality factor, Q_i, for these resonators is far greater than the coupling quality factor, Q_c, the total resonator quality factor, Q_r, is limited by Q_c since

$$\frac{1}{Q_r} = \frac{1}{Q_c} + \frac{1}{Q_i} + \frac{1}{Q_{loss}}, \tag{5.3}$$

where Q_{loss} represents parasitic losses in the resonator from the inductance or the capacitance.[75]

Table 5.1: Frequency plan of the 850 GHz array based on the two IDC finger sizes and either shorted or non-shorted inductors. The frequency values are in units of MHz.

	5 μm IDC	12 μm IDC
Non-Shorted	300 - 435	435 - 635
Shorted	635 - 925	925 - 1,350

The designs are based around two different inductor designs which are identical except for two lines being shorted together. Target values for the inductance are 200 nH and 50 nH, which assumes that the kinetic inductance dominates all other sources of inductance. Note that in some simulations a geometric inductance as high as $\sim$ 10 nH was found for models of potential MKIDs. Disregarding the geometric inductance, the target inductances were set as constants and the available ranges in capacitor sizes were then explored under the assumption that the overall footprint of the pixels were minimized; the simulations were essential in determining the ideal size of the capacitor fingers. An IDC ideally has enough fingers to be able to tune the resonator across its given band, but not so many that the size of the capacitors becomes cumbersome and a 1.4 mm pixel pitch is unachievable. Given that a typical MKID operates above 1 GHz, the 300 MHz baseline for the readout means the resonator designs require a large amount of capacitance.

We were able to determine two different sets of capacitors which would allow for tuning across the entire planned readout band. The result is two sets of IDCs of differing widths, 5 µm and 12 µm. Using the two values for the inductance and two sets of capacitors, the two octaves worth of resonators are easily obtained (See Table 5.1). The frequency spacing assumes a spread of 0.15% between resonances, beginning at the readout baseline of 300 MHz. The variations in the design are so simple, the sets of detectors are practically indistinguishable aside from a handful of lines shifted in the design software. Essentially, the line shorting provides a coarse tuning of the resonance, and the capacitors are relegated to fine tuning the resonators within the given band.

5.3 Preliminary Results from a MKID Test Array

The parameter space outlined for the detector development for the 850 GHz module has been presented above. More than a dozen distinct detector designs have been designed to explore the variables to guide the optimization of the final pixel array. A series of witness chips have been designed, a sample of which is shown in Figure 5.4. Witness chips allow the exploration of features

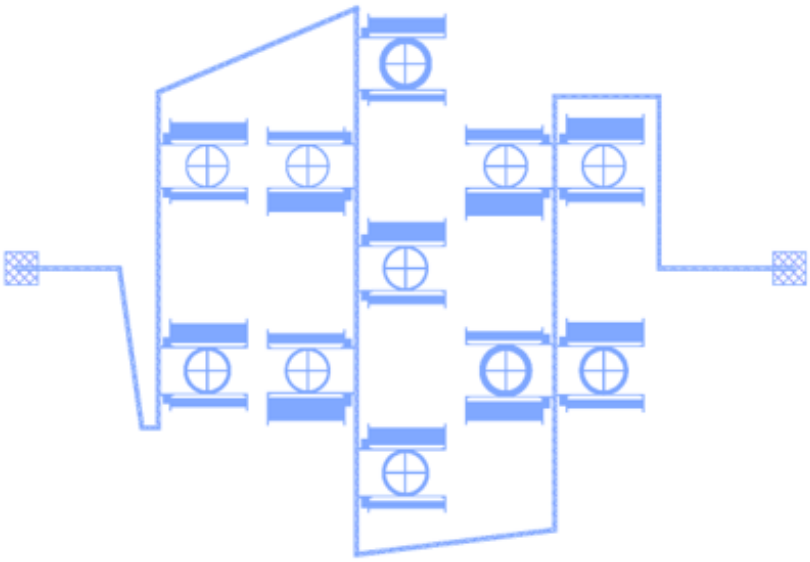

Figure 5.4: Schematic of an 850 GHz witness chip. Each chip includes 11 pixels total: seven optical and four dark. Each pixel consists of two orthogonal polarization-sensitive detectors.

such as the thermal and optical response with rapid turnaround time. Each witness chip consists of 11 pixels, seven of which are optical and four dark pixels. The test box (see Sec. 4.2) is designed to explore noise inherent in the system and factors such as cross-talk between detectors and cross-polarization within a single pixel. Fabrication of the witness chips also probes the accuracy of models matching theoretical frequency plans and actual results.

An issue arising from the small scale of the witness chips is its inability to characterize the scalability of the designs. As a better sample, a 144-pixel array was developed to address both the scalability of the design to multiple octaves and highlight issues that need to be addressed in resonance positions. The larger test array also provides an opportunity to test the capabilities and performance of the multi-octave readout system. Characterizing the thermal and optical responses of each design in tandem with the scalability and performance of the detectors in conjunction with the readout will be crucial in finalizing the focal plane arrays.

5.3.1 Dark Testing

The TiN prototype arrays underwent dark testing, where the detector response was modulated by varying the bath temperature as a test of the thermal responsivity. Results were taken using a VNA sweep functionality in the RFSoC readout.[21] A sample result is shown in Fig 5.5. The results

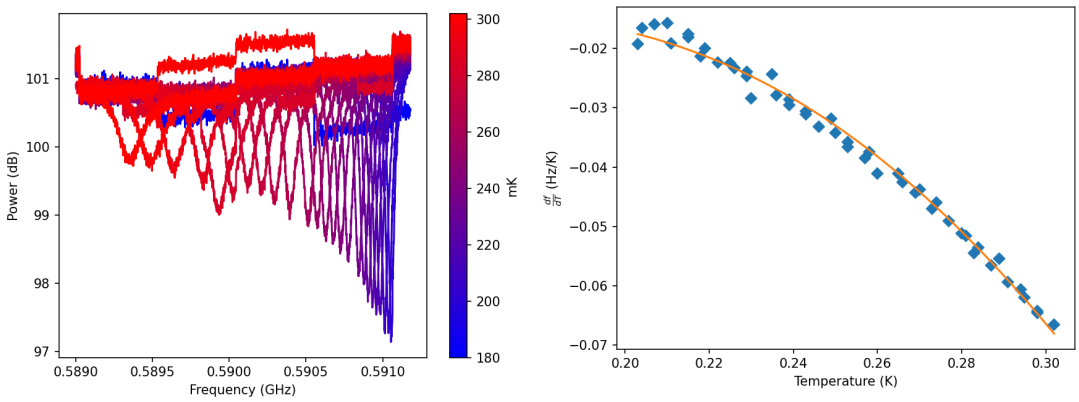

Figure 5.5: Sample results of a TiN prototype kinetic inductance detector. Left: VNA sweeps of a resonance probing thermal responsivity. The detector exhibits the expected decrease in resonant frequency and quality factor (broadening) with increasing temperature. Right: The thermal responsivity is remarkably well fit with the Mattis-Bardeen curve. Parameters such as critical temperature and the kinetic inductance ratio may be extracted from this fit and used to compare and optimize competing detector designs.

show the expected shift in both resonant frequency and quality factor with increasing temperature, seen as a shift to a lower resonance frequency and broadening of the resonance profile as shown in the left panel. The discontinuities arise from differences in tone powers being output by the the readout system. Regardless of the discontinuities, the thermal responsivity is remarkably well fit with the Mattis-Bardeen curve, shown in the right panel of Fig 5.5. From the fit, crucial parameters may be extracted to compare and optimize competing detector designs. This includes parameters such as critical temperature and the kinetic inductance ratio. MKID design is complex, and these preliminary tests are insufficient to answer questions such as the ideal ratio of optically active and dark inductances, or the impact of shorting the inductor on parasitics in the system. What follows will explore results from the updated generation of MKIDs developed to continue exploration of these and other variables outlined above.

5.4 850 GHz Prototype MKIDs

The preceding sections outlined a cumbersome parameter space with numerous variations of designs to explore. These designs can be probed using a series of dark and optical tests on witness chips, which are small samples of detectors configured with some number of detectors able to be coupled to an external source (see Figure 5.4). A single witness chip allows one to find optimal

Table 5.2: Detector parameters for the eleven pixels included in the witness chips.

Pixel	Line Width (μm)	Number of Lines	Inductance (nH)	Volume (μm^3)	Optical or Dark
1	2.8	2	52.5	375	Optical
2	2.8	2	89.5	670	Optical
3	2.8	2	169	1290	Optical
4	1.4	4	122	232	Optical
5	1.4	4	200	377	Optical
6	1.4	4	72	526	Optical
7	1.4	4	90	650	Optical
8	2.8	2	52.5	375	Dark
9	1.4	4	122	232	Dark
10	1.4	4	200	377	Dark
11	2.8	2	169	1290	Dark

parameters for a series of variables, such as the inductance, volume, and line width of a resonator. Several types of witness chips were fabricated: low and high coupling capacitor chips ($Q_i = 20,000$ and $Q_i = 40,000$), different ratios of optical to dark inductance, and a series where half the capacitors are not etched to explore the impact of TLS noise. Table 5.2 presents the parameters of the different pixels used for the witness chips. Recall that a single pixel consists of two orthogonal resonators, meaning there are two resonators for each design. Another set of sample arrays with 144 dark pixels was designed to explore the feasibility of the multi-octave design. Fabrication of the prototype detectors utilized a pentalayer TiN film consisting of three layer of 4-nm thick TiN separated by layers of 10-nm Ti. Figure 5.6 show two samples of fabricated prototypes.

Due to time constraints and mechanical issues with cryostats, the TLS test and light to dark inductance ratio chips were not tested. These will be tested in the future as they will provide insight into fabrication requirements in the case of the TLS test chip, and exploration of a previously unexplored parameter in the case of the light to dark inductance ratio chip.

5.5 Prototype MKID Characterization

The final portion of this chapter reports the measurement and performance of the prototype MKIDs designed for the 850 GHz module. Fabrication of the wafers was done at the National Institute of Standards and Technologies (NIST) in Boulder, Colorado. Tests were conducted to confirm the shorting technique performs as expected, characterize the new pentalayer TiN film, measure

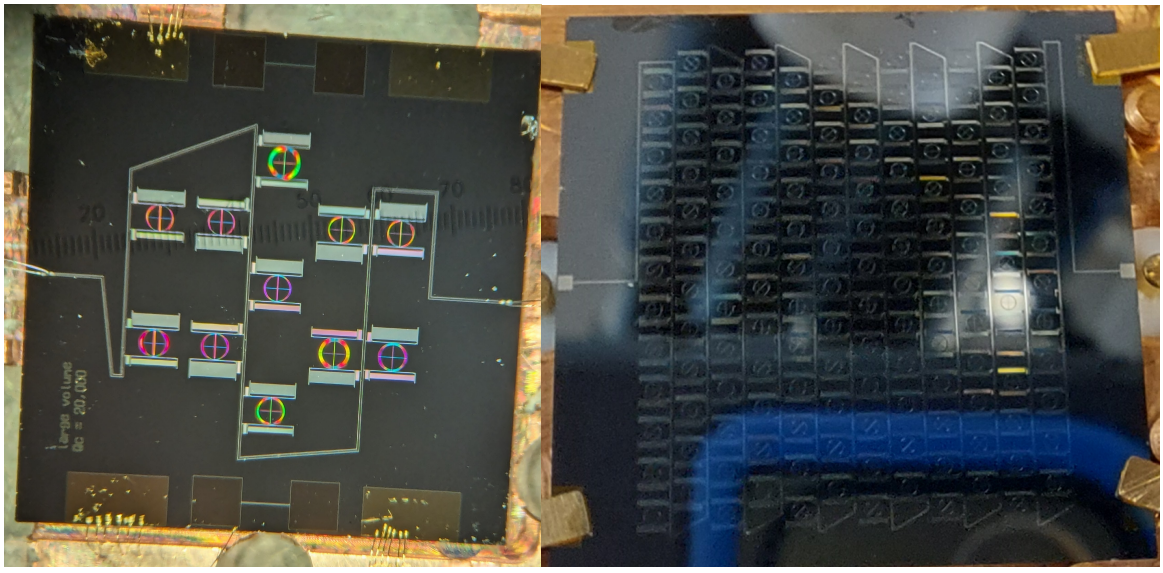

Figure 5.6: Left: A fabricated witness chip with $Q_i = 20,000$. Seven pixels are designed to be optically coupled with the test box, and four pixels will be tested exclusively dark. Right: A fabricated two-octave array prototype. All 144 pixels (288 resonators) are designed to be tested dark.

the thermal and optical responsivity of the TiN MKIDs, and explore the noise performance of the prototypes. Prototype wafers were tested in multiple cryostats, specifically two units at NIST, and the setup detailed in Chapter 4, which resides at the Herzberg Astronomy and Astrophysics (HAA) center in Victoria, British Columbia. A description of the experimental setup is given in Sec. 5.5.1; preliminary results from a two-octave prototype array are presented in Sec. 5.5.2; Sec. 5.5.3 shows and discusses the measured responsivities of the prototypes; and a first noise analysis of the prototype MKIDs is shown in Sec. 5.5.4.

5.5.1 Experimental Setup

Tests for the 850 GHz prototypes were conducted in three cryostats, two at NIST (a Bluefors LDR and adiabatic demagnetization refrigerator (ADR) cryostat) and and one at HAA (Bluefors LDR). Of these, only the NIST LDR was used for optical testing due to the availability of magnetic shielding for the cryostat and the availability of the requisite test kit including a calibrated cryogenic blackbody. The NIST ADR and HAA LDR were used for dark tests, which included measuring the critical temperature of the pentalayer, performing bath temperature and readout power sweeps, and exploring the characteristics of the two-octave design.

For dark tests, the boxes were mounted to the coldest stage of the given cryostat and connected

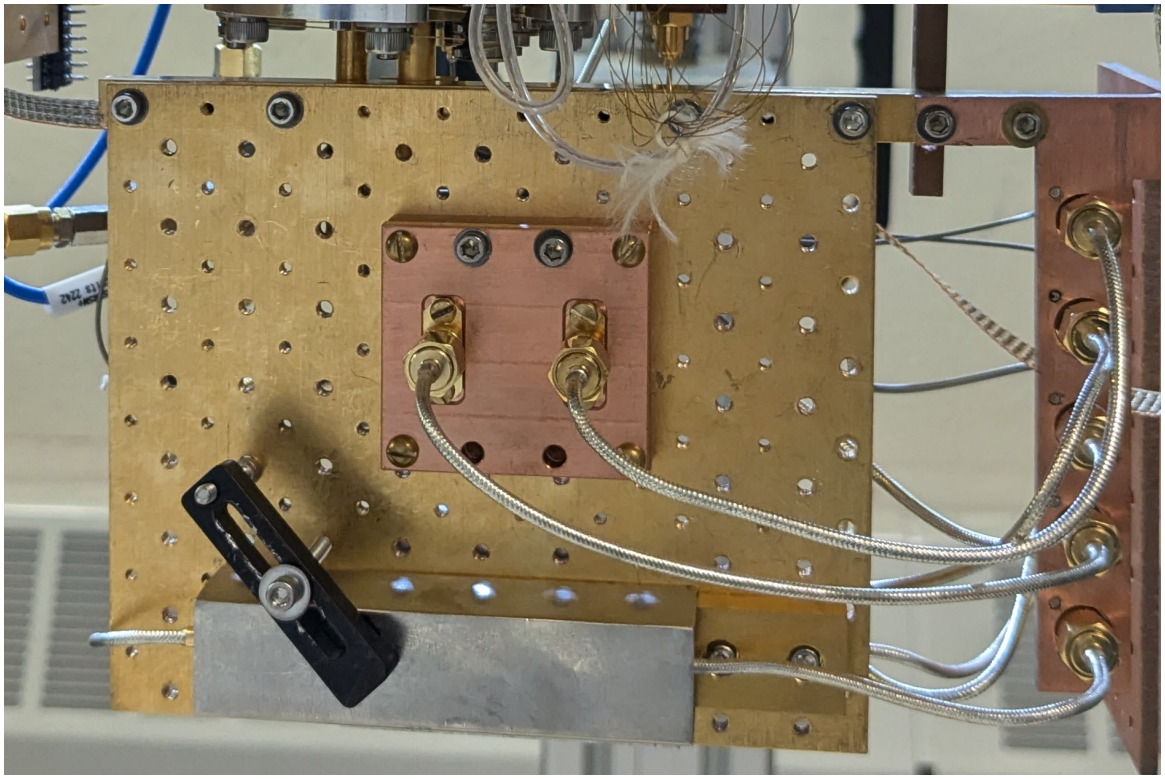

Figure 5.7: Setup of a two-octave array (top) and dark test of a prototype chip with added magnetic shielding (bottom) inside the NIST ADR.

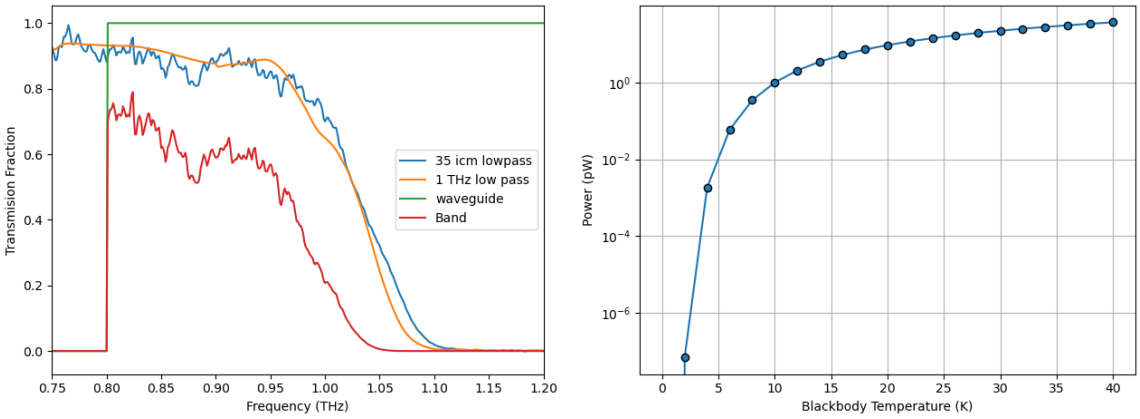

Figure 5.8: Left: Transmission fraction for each component defining the overall transmission (red). There were two of each type of filter used in the tests. Right: Calculated power incident on the detectors based on the output power of the blackbody source and the transmission band.

to SMA feedthrough lines leading to room temperature, as shown in Figure 5.7. To achieve greater precision in the measurement of Q values, additional magnetic shielding was included around the test chips. The critical temperature of the pentalayer film was measured in the NIST ADR due its ability to hold temperatures greater than 1 K with a PID loop. Bath temperature and power sweeps were performed in both the NIST ADR and HAA LDR using VNA scans stitched together to provide high resolution measurements across the whole relevant range of the detector prototypes, which allows for each of the resonators to be fit and characterized. For these tests, the HAA LDR provides the advantage of lower base temperatures, allowing for better range in bath temperature sweeps, which is crucial in exploring factors such as TLS noise which dominates as the bath temperature drops.

Optical tests were performed exclusively in the NIST LDR. A calibrated cryogenic blackbody was suspended from the still flange, with thermal offsets to prevent excess heating of the cryostat while achieving blackbody temperatures as high as 72 K. Two IR low-pass filters were attached to the output of the blackbody, and two more IR low-pass filters were used in the test box, ensuring a well defined edge at the high frequency edge of the measured band. Recall from Chapter 4 that the diameter of the waveguide in the feedhorn block defines the low frequency edge of the band. The resulting band is shown in Figure 5.8, which also depicts the incident power on the detectors based on the overall transmission of the system and the temperature of the blackbody The test box was affixed directly below the cryogenic blackbody to ensure that the entire FoV of the detectors was filled by the blackbody, as shown in Figure 5.9

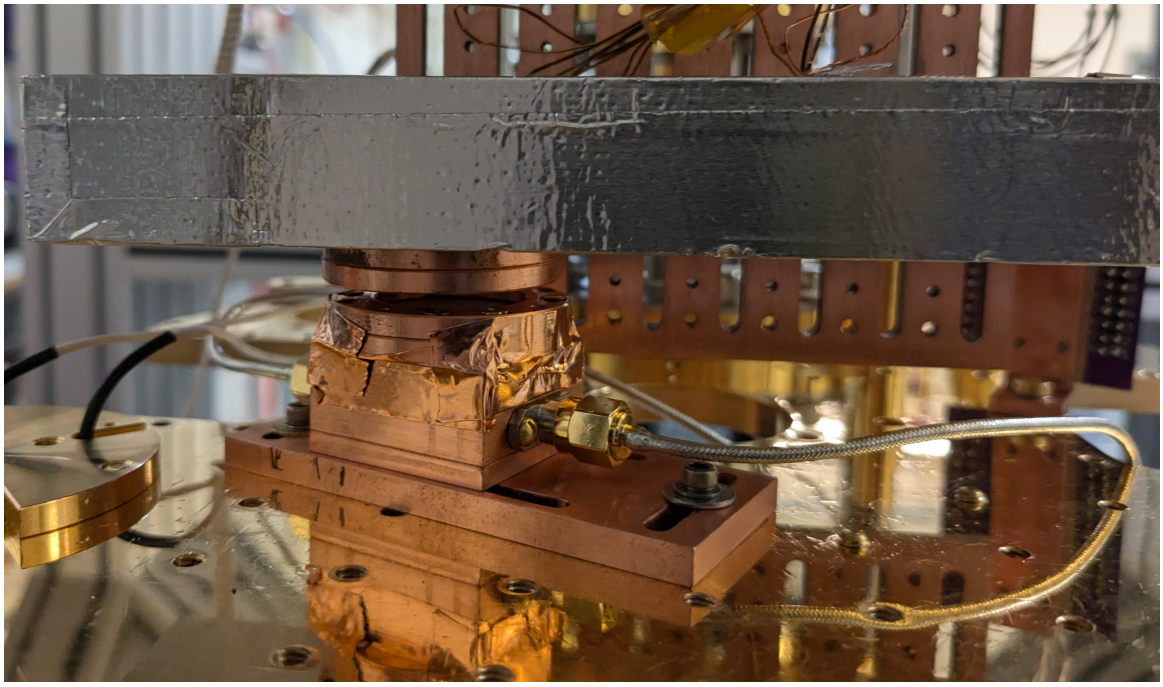

Figure 5.9: Setup for optical tests inside the NIST LDR. The blackbody (top) is thermally connected to a separate stage to prevent heating the prototype arrays in the test box (bottom).

The tests faced three main issues. First, the cryogenic LNA used in the NIST LDR showed greater 1/f noise than expected, leading to delays in obtaining results as the LNA was swapped with an amplifier with better performance. The second problem arises from the blackbody output. As shown in Figure 5.8, the output of the blackbody is able to achieve $\sim$42 pW output at 40 K. However, the predicted atmospheric loading lies in the range of approximately 60-100 pW of loading in the first quartile conditions. Once again, delays in measurements were introduced as the system needed greater thermal isolation to avoid overheating the NIST LDR stages. Lastly, and most seriously, the feedhorn positions on the block did not match those of the pixels on the test chips, as shown in Figure 5.10. A sample Si feedhorn block was successfully fit-tested to a test chip to confirm alignment of the system and rule out any issues in the fabrication process. The designs of both the witness chips and the feedhorn blocks were reviewed, ensuring there were no deviations between the two. These results indicate the misalignment arose due to an error in fabrication and missed tolerances. In order to proceed with testing, the prototype array was diced to allow testing of two pixels, the fiducial 377 μm^3 and the 1,290 μm^3 volume, the largest prototype MKID volume. While this ultimately limited the overall results, as will be shown below the sampling of these two pixels

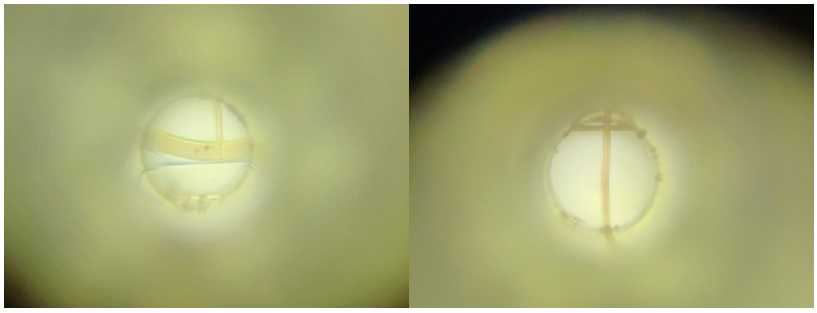

Figure 5.10: Sample pixels showing the misalignment of the feedhorn block holes with the detectors. The expected deviation was roughly 21 µm to account for thermal contract, far less than the observed deviation.

ultimately proved informative to the final design of the 850 GHz detector.

5.5.2 Two-Octave Prototype Array

A two octave prototype array was affixed in a Bluefors dilution refrigerator and cooled to sub-Kelvin temperatures to provide a first look at a two-octave design using the shorted inductor technique. Figure 5.11 presents a VNA sweep of the first two-octave MKID array designed to span multiple octaves. The results confirm that shorting the inductors is a viable method for coarsely tuning inductors across a two-octave band. Seen are four distinct bands, representing the four types of detectors as outlined in Table 5.1. The gaps between the bands were included in the design to enhance visibility.

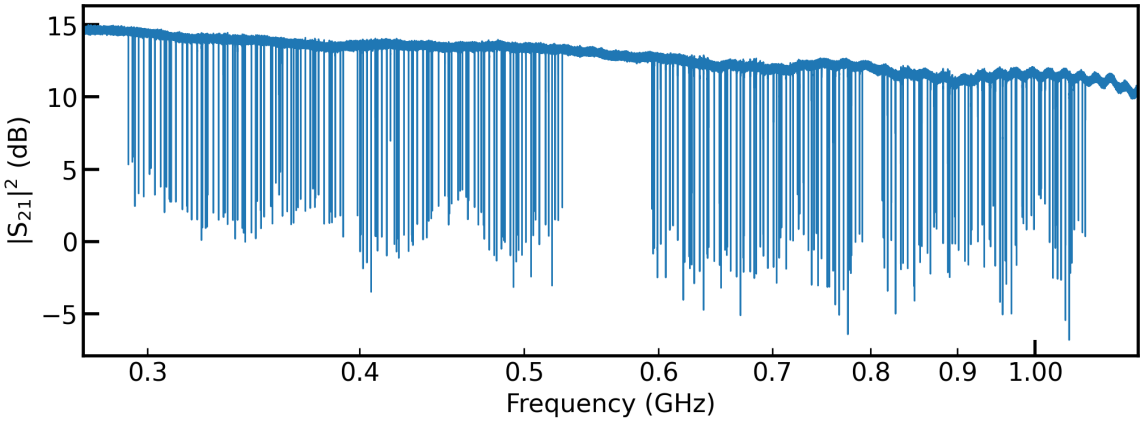

Figure 5.11: VNA sweep of a two octave array using the shorted inductor technique. Four distinct bands are visible, representing the four detector types.

In terms of manufacturability, the two-octave arrays which were tested showed that the fabrication process achieved greater than 98% yield (284/288 and 286/288). While such a high yield is

expected as there is significant spacing between the resonators, meaning minimal yield losses due to collisions, this highlights that the narrowness of the inductor and capacitor lines, as well as the fabrication recipe will introduce minimal yield losses in the final array due to fabrication. Furthermore, with the development of techniques to provide post-measurement corrections to arrays in order to reduce collisions,[105] it is expected that despite having the most densely-packed FIR MKID arrays, the 850 GHz module should have high detector yield.

Each of the resonators were fit to determine a host of parameters, such as Q_i, Q_c, and the time constant, τ. Determining these parameters informs the design and fabrication of the TiN detectors, a vital step in determining the efficacy of the pentalayer design of the film. The left panel of Figure 5.12 depicts a histogram of the Q_i values for the two-octave array showing that the designs resulted in Q_i greater than 100,000. This is crucial to understand since for TiN arrays, Q_i may vary greatly depending on the recipe. The right panel of Figure 5.12 presents the measured T_c for the TiN arrays, which was found to be roughly 850 mK. With the measured normal resistance of the TiN, 31.5 $\Omega/\square$, the kinetic inductance can be calculated using

$$\mathcal{L}_K = \frac{k_B R}{\pi \Delta_0}, \tag{5.4}$$

which yields 51.1 pH/$\square$. Lastly, the time constant for the TiN detectors was found to be in the range of 0.15-0.2 ms. These results suggest the film may be expanded further to a "septalayer" design without degradation of the detector quality should additional volume be needed for the detectors.

5.5.3 Experimental Responsivity

In order to characterize the different prototype detector designs, the thermal and optical responses were measured. The thermal responsivities, shown in the top panel of Figure 5.13, matches the expected response while showing a spread in response with increasing temperature which arises due to variations in the resonator volume. Q_i (bottom of Figure 5.13) likewise shows a relatively muted response before dropping at higher temperature. Both responses match the expected form predicted by theory as presented in Chapter 3.

The focal plane of the Prime-Cam instrument is intended to remain at a bath temperature of 100 mK, maintained as near as possible using a PID loop. At the relevant bath temperature, the

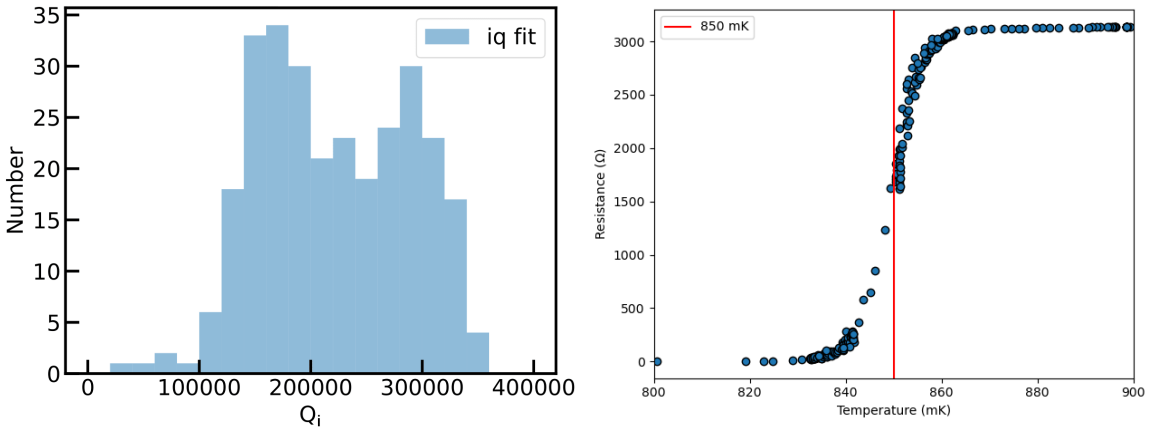

Figure 5.12: Left: Histogram of the fit Q_i values of the resonators in the two-octave prototype array. The overwhelming majority of resonators achieved Q_i greater than 100,000. Right: DC measurement of the critical temperature of the pentalayer film used for the TiN prototype detectors.

variations in the frequency response due to temperature are so small, the differences in the response are practically indistinguishable between different detector designs. Q_i likewise shows relatively muted response which remains approximately constant around 100 mK before dropping at higher temperature - well beyond the range of operation in Prime-Cam. Results of these tests indicate the overall success in the design and fabrication of the prototype detectors, particularly in the properties of the pentalayer film.

As mentioned in Sec. 5.5.1, alignment issues greatly limited the available optical tests for the prototype arrays. Fortuitously, initial tests showed that the fiducial volume detector was sufficiently aligned to characterize. Preliminary results showed that the responsivity of the fiducial volume to optical loading was far greater than what was desired, leading to the conclusion that the most crucial design to test was the highest volume resonator. This decision is reflected in the lack of results for other designs, as the witness chip needed to be diced in order to properly align the requisite pixel, the results of which are shown in Figure 5.14.. The tests were expanded to explore as far into the expected loading range of the 850 GHz module as possible, to determine the response of the resonator, which is closely determined by the volume of the resonator (see Sec. 3.3.2). Figure 5.15 shows results for Q_i with increasing optical loading, which convey relative stability across the expected range of loading for the module.

One vital confirmation from these tests arises from the fact that in the working limits of the 850 GHz module, the responsivity due to the thermal fluctuations around 100 mK is far less than the

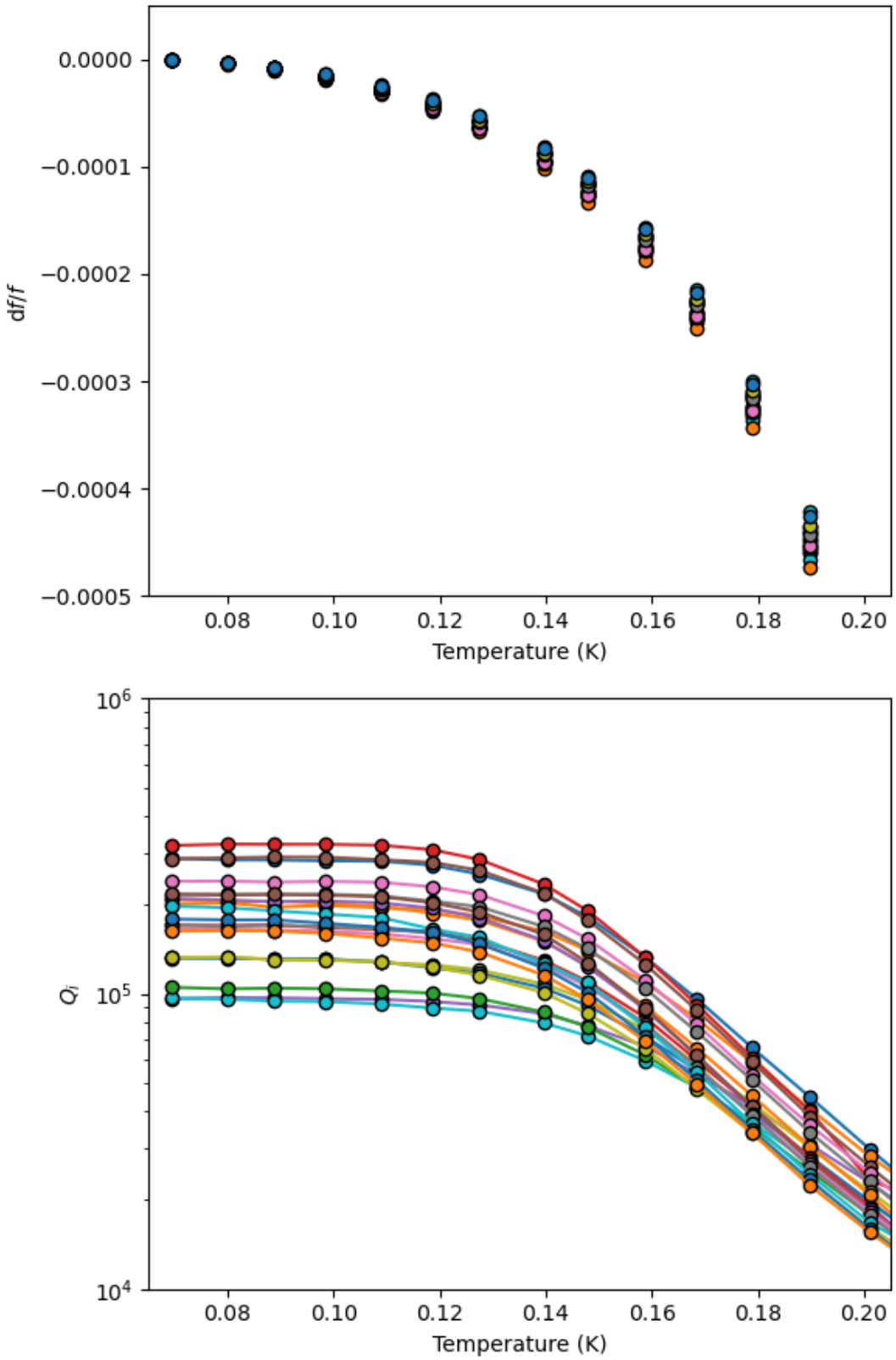

Figure 5.13: Measured thermal response in frequency (top) and Q_i (bottom).

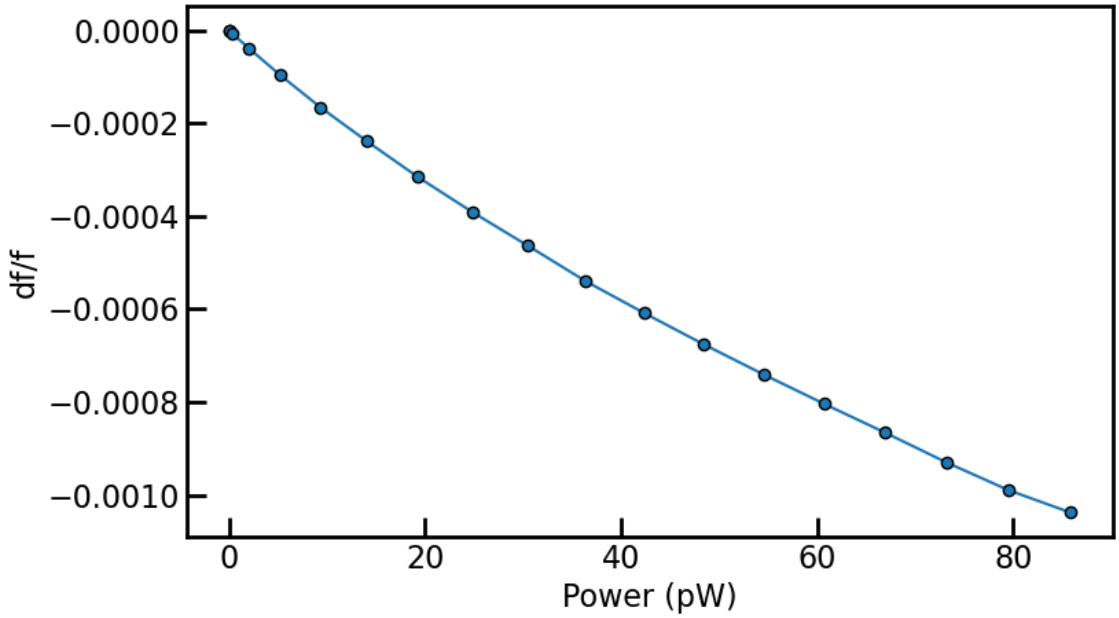

Figure 5.14: Optical response for the high volume protoype resonator.

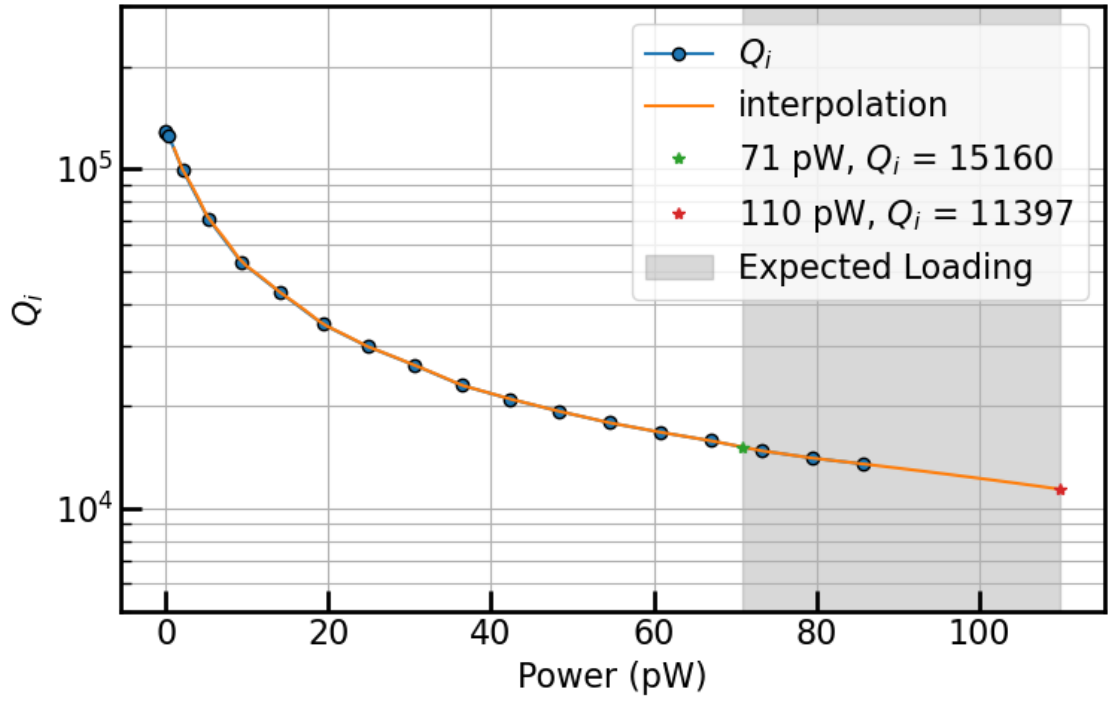

Figure 5.15: The internal quality factor, Q_i, as a function of input power for loading levels expected for the 850 GHz module. For the expected typical loading level of 71-110 pW, Q_i is relatively constant with a mean value of ∼13,860. The higher limit of the fit was calculated using linear interpolation.

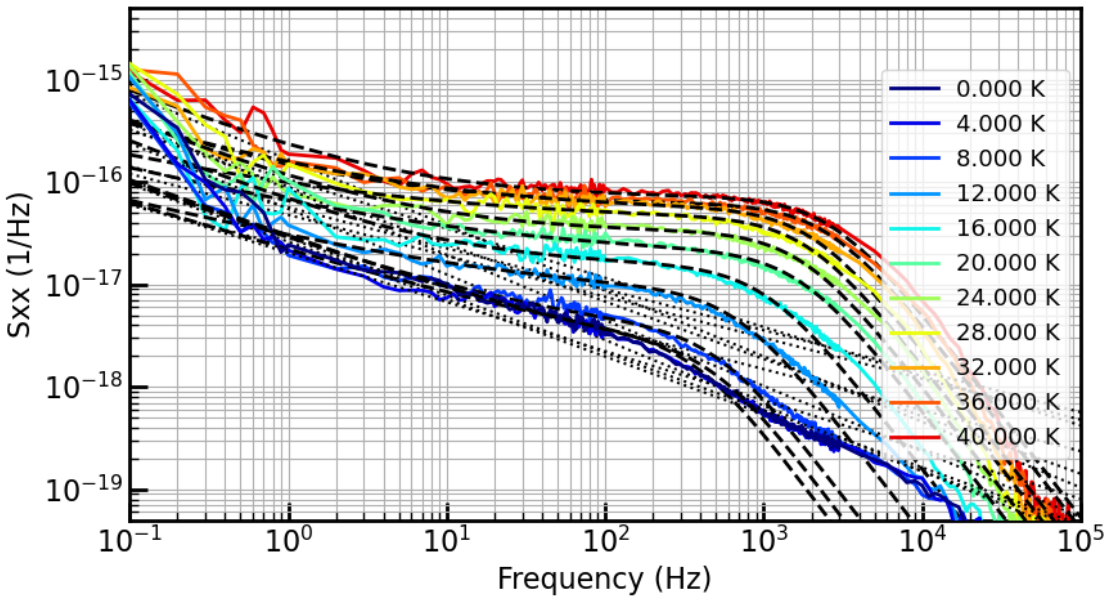

Figure 5.16: Power spectral density as a function of increasing optical loading with low-frequency noise slopes for the high volume 1,290 μm^3 resonator. At the loading levels expected for the module on site, the 1/f TLS noise is subdominant. At lower loading, it is clear the TLS noise is subdominant to photon noise, but still contributes significantly. Additional low frequency noise is believed to be due to temperature fluctuations in the blackbody source at higher temperatures. The dashed lines depict the fits to the overall noise profile, and the dotted lines represent the fits to the 1/f noise, which is assumed to be dominated by TLS noise.

responsivity due to optical signals while the system is under loading. This property is crucial for MKIDs, else the arrays essentially become thermometers. Note that a thermometer-like design is not necessarily a problem and can be exploited to serve much like a bolometer, as is the case with thermal kinetic inductance detectors[106] (TKIDs).

5.5.4 Noise Analysis

In order to better understand the response of the MKID prototypes, a noise analysis was performed where the spectrum of the noise was examined, the functional noise equivalent power of optically loaded MKIDs was calculated, and the optical efficiency of the system was fit. Understanding the noise sources in a given system informs revisions necessary to achieve the required sensitivities for a given instrument. The theory behind the noise in MKIDs is covered in Chapter 3. What follows are the results of an analysis on the prototype MKIDs.

In general, the power spectral density (PSD) is used to define random signals as it is a measure

of the power in a signal as a function of frequency. This includes power from both the desired signal and unwanted noise. For the prototype detectors, the PSD was calculated across increasing optical loading levels, which increases both the photon and generation-recombination noise in the system. Measuring the noise across the relevant range of loading allows for the sensitivity to be probed across across the operational range of the system, providing more information for finalizing the detector design.

The PSD of a signal, denoted S_{xx}, is calculated as the Fourier transform of the autocorrelation of the signal:[107, 108]

$$S_{xx} = \int_{-\infty}^{\infty} R_{xx}(\tau) \exp^{-i2\pi f\tau} \mathrm{d}\tau, \tag{5.5}$$

where R_{xx} is the autocorrelation of the signal measured over a finite interval T:

$$R_{xx}(\tau) = \lim_{x\to\infty} \frac{1}{T} \int_{-\infty}^{\infty} x_T^*(t-\tau) x_T(t) \mathrm{d}t. \tag{5.6}$$

Figure 5.16 depicts the calculated PSD swept across increasing incident power for the high volume resonator. Once the PSDs are calculated, the noise sources are characterized with a fit using the following five-parameter model:[109]

$$S_{xx} = \frac{A + Bf^{-C}}{1 + (2\pi f D)^2} + E \tag{5.7}$$

where A is the resonator white noise, Bf^{-C} is the $1/\sqrt{f}$ noise (dominated by TLS), D is the quasi-particle lifetime τ, and E is the system white noise level, particularly the amplifier white noise level. We subtract the system white noise level off for our modelling, and can therefore exclude E from the fit. The NEP is derived from the PSD simply as NEP $= \sqrt{S_{xx}}$.

The low frequency noise slope is depicted in Figure 5.16 as small dotted lines, which represent the response of the TLS noise. It is clear by eye that at 1 Hz, the TLS noise is subdominant to the photon noise at the relevant loading levels, though it still has a significant contribution to the overall noise. Specifically, for the large volume resonator we see photon noise limited performance with a PSD of 2×10^{-17} at 850 GHz, while we see TLS noise with a PSD of 1×10^{-17} at 1 Hz. Figure 5.16 also shows a confounding increase in the 1/f noise at higher loading. The present working theory is that this is the result of temperature fluctuations in the blackbody source at higher temperatures.

The NEPs for the fiducial and large volume resonators are shown in Figure 5.17. These results show that for both volumes there is a large shift in the noise level with small increases in loading levels, particularly at the lower limit of optical loading. Furthermore, for both cases the system is clearly photon-noise limited. However,the fiducial volume resonator shows a lower TLS noise than that of the high volume detector. The fiducial volume resonator also lacks the increase in 1/f noise seen in the NEP of the high volume resonator. Note that the fiducial volume was not measured to higher levels of optical loading due to timing and setup constraints. In both cases, the measured detectors showed sensitivities less than 10^{-15} W/Hz$^{0.5}$.

The remaining step in the analysis is to extract the optical efficiency of the system, ε, from the white noise parameter of the system, or A in Equation 5.7. To get an accurate representation of the response, the white NEP of the resonator is defined as the squareroot of the ratio of white noise to the optical responsivity, or $NEP_{white} = \sqrt{A/R}$. These values are then compared to the NEP from photon noise, NEP_γ, and generation-recombination noise, NEP_{gr}. Recall that NEP_γ is defined in Equation 3.58, and NEP_{gr}, for optically driven generation and recombination, is defined in Equation 3.61. The variables required to solve for these values are the photon occupancy number, n_0, the pair-breaking efficiency, η_{pb}, and the optical responsivity, R_P. Note that for η_{pb}, a constant value of 0.6 was used as this has been accurately measured on other devices.[110] Calculated values for NEP_γ and NEP_{gr} must not only be added in the quadrature sum, but must also be corrected for by the optical efficiency which contributed to these measurements:

$$NEP_{Model} = \sqrt{\frac{NEP_\gamma^2 + NEP_{gr}^2}{\varepsilon}}. \tag{5.8}$$

Finally, the results were also compared against NEP_γ. The results for the high volume resonator are shown in Figure 5.18, which show an optical efficiency of $\sim$0.8. Values for the optical efficiency have been consistent across all measured resonators to date.

5.5.5 Discussion

First tests of detectors fabricated using shorted and non-shorted inductors confirmed the efficacy of this technique (Figure 5.11). Figure 5.19 shows the range of the full two-octave band and extends to include the parasitic resonances. There is a significant band between the readout and parasitic

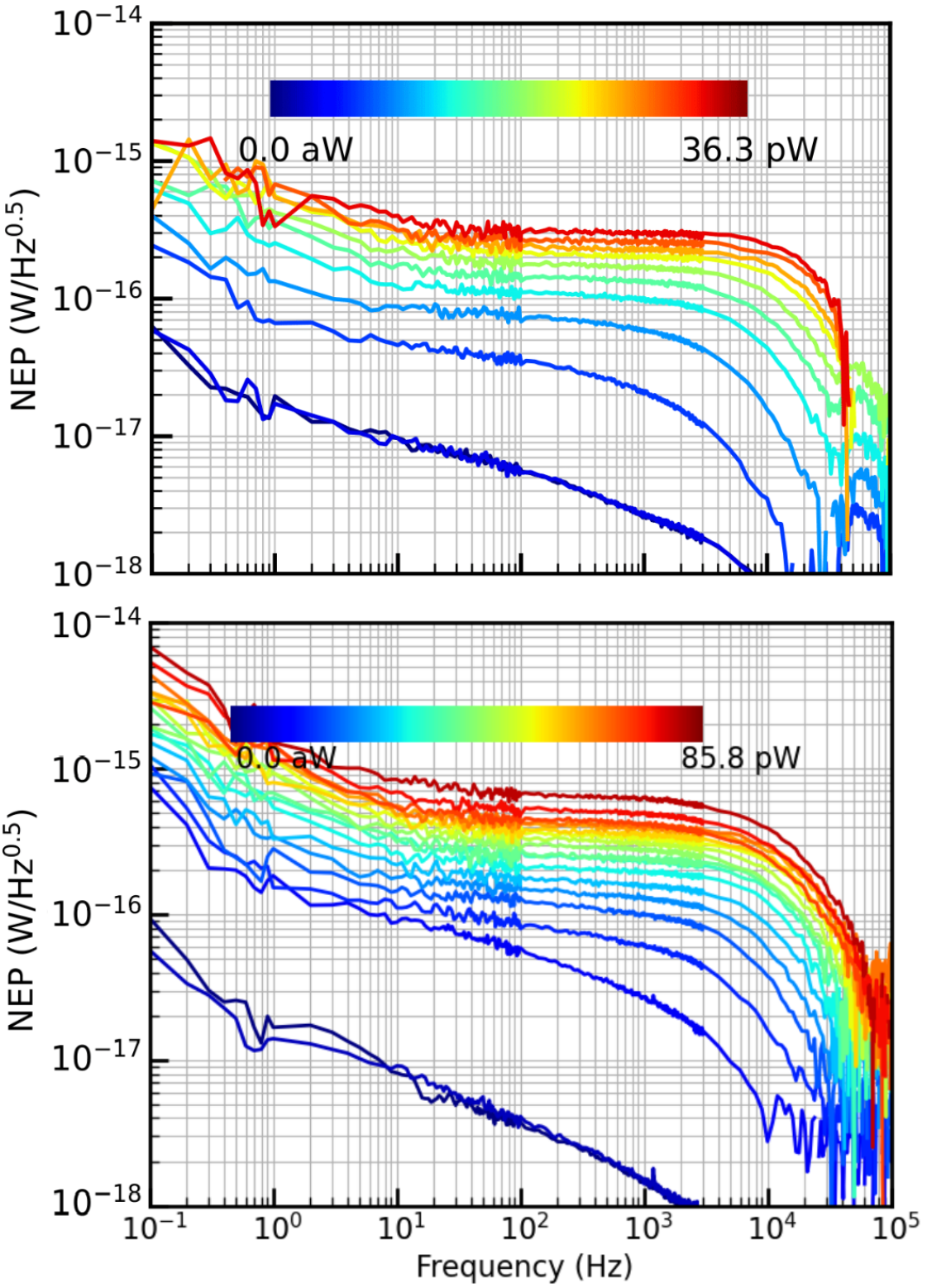

Figure 5.17: NEP with increasing optical loading for different volumes of resonator. Top: NEP of the fiducial 377 μm^3 resonator. The resonator exhibits high sensitivity to loading at low input powers. Bottom: NEP of the higher volume resonator (1,290 μm^3). At lower loading, TLS noise is subdominant to photon noise, but still contributes significantly.

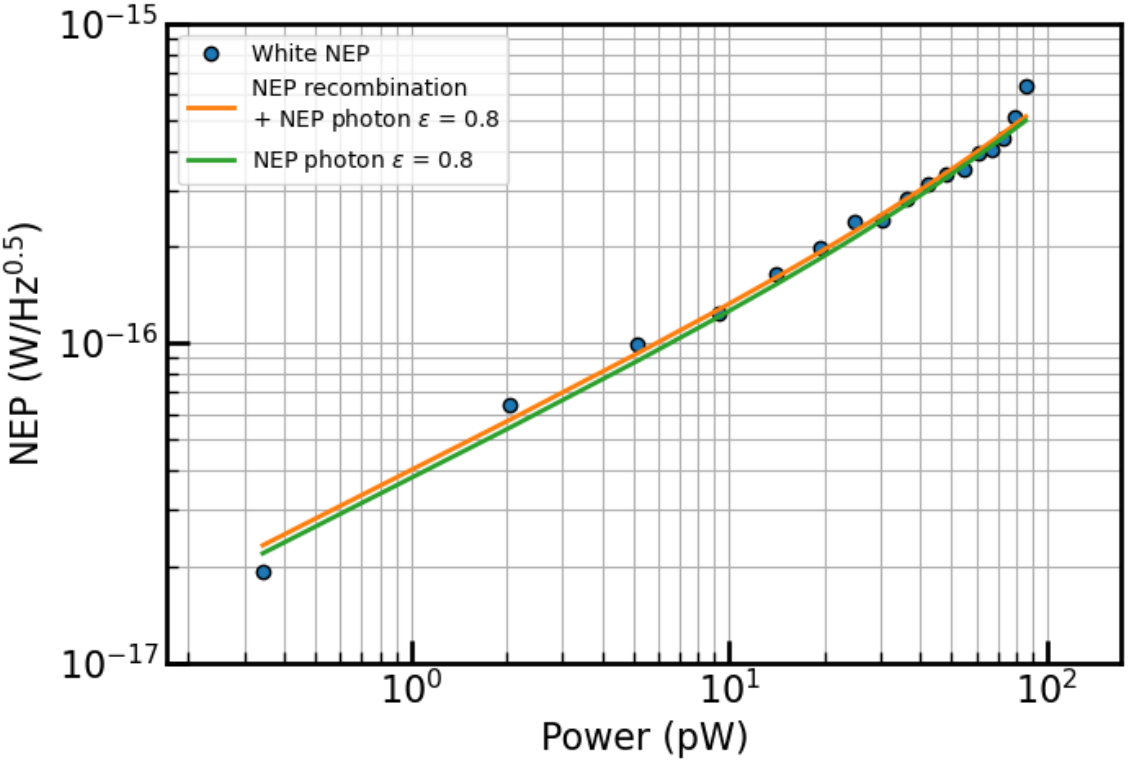

Figure 5.18: White noise equivalent power as a function of incident power for the high volume resonator (1,290 μm^3) showing the fitted optical efficiency, ε. The results of fitting show an optical efficiency of ∼0.8.

resonances - nearly a another octave. As the complexity of the final arrays increase, it is expected that these resonances will shift to lower frequencies due to microstrip modes and the overall architecture of the array. Having a substantial gap increases the likelihood of minimal interference between these resonances. If the intervening band between the two resonance remains clear, it raises the potential for a design greater than two octaves.

High yields were achieved in both the tested two octave arrays, which highlights the success of fabrication. Values for Q_i were greater than 100,000 in nearly all cases. Since Q_i depends greatly on the material properties of the film, this emphasizes the resounding success of the pentalayer design. The measured properties matched with remarkable precision to the predictions provided by NIST, which were used in modelling and designing the arrays. These results imply that, should the need arise to increase the volume of the detectors to combat higher loading arise, a thicker film comprised of more layers could be accurately modelled and fabricated for future detectors.

Thermal tests of the witness chips confirmed the results of the DC measurements used to char-

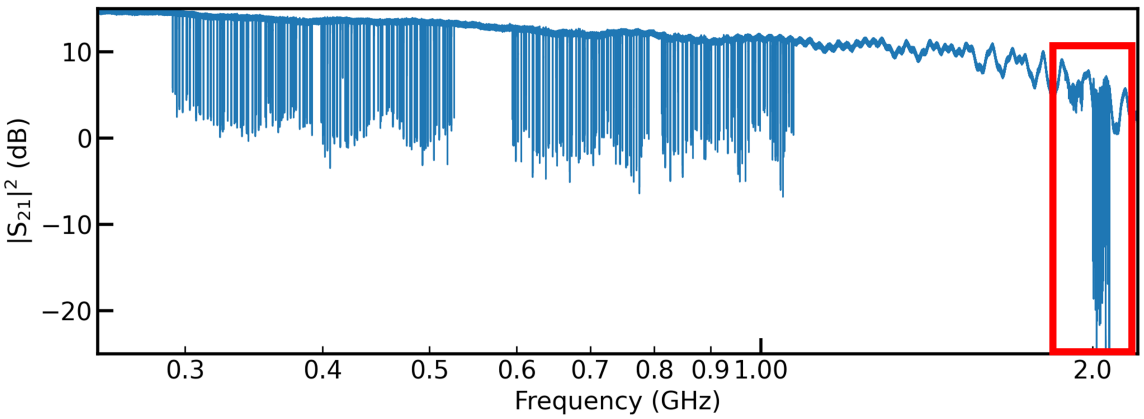

Figure 5.19: VNA sweep of a two octave array emphasizing the parasitic resonances (highlighted in red). The range between the readout band and the parasitic resonances is significant and clear of any signal.

acterize the film. The measured resonators exhibited high Q_i values, matched well with expected parameters based on simulations, and showed high stability at the expected bath temperature (see Figure 5.13). However, an interesting result arose due to an issue in the setup where the test wafers were mounted directly beneath a non-superconducting material, gold-coated copper. Models for the detectors assumes a superconducting ground plane for the resonances, and in the case of the gold-coated copper the results showed a sharp drop in overall detector performance, particularly Q_i as shown in Figure 5.20. The obvious solution is the inclusion of a superconducting waveguide interface plate (WIP), ideally aluminum-coated, to ensure a consistent grounding plane is present for all the resonators. The final array will utilize a gold-coated Si feedhorn block, which demands an aluminized Si WIP for both ideal performance and alignment.

The optical responsivity presented in Figure 5.14 provides a sufficient and measurable shift in frequency in the expected loading regime. However, as shown in Figure 5.15, the mean Q_i within the expected loading range is ∼13,860. The proposed target for performance is to have $Q_i \simeq Q_c$ under loading, though having low Q_i limits Q_r to less than Q_c, which may have benefits in controlling the effective noise temperature of the detectors to reduce readout noise.[19] It should be noted that the detectors easily achieved the critical threshold of having optical responsivity at the relevant loading far greater than the thermal responsivity at the expected bath temperature.

To mitigate the issues of low Q_i, one may increase the volume of the resonator. This may be done by increasing the linewidths in the resonator or adopting a new septalayer TiN film for the

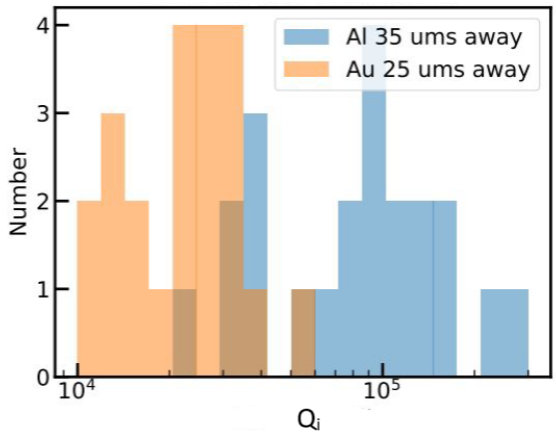

Figure 5.20: Measured Q_i for a non-superconducting gold grounding plane and a superconducting aluminum grounding plane.

resonators. A simpler solution is to adjust Q_c, though this comes with a tradeoff between amplifier noise (proportional to Q_c/Q_r) and collisions in the final design, reducing the yield. Holding Q_i constant, while increasing Q_i reduces the total number of collisions potentially by a factor of two, although this increases the amplifier noise by a factor of roughly two as well. To balance this dichotomy, it is proposed that a value of Q_c =30,000 is adopted for the arrays.

Analysis of the noise revealed that the desired sensitivity of at least 10^{-15} W/Hz$^{0.5}$ is achieved at the predicted loading. Furthermore, the NEP is photon noise dominated. However, the initial measurements revealed that the TLS noise is greater than expected. This is generally resolved through optimizing the interdigitated capacitors (IDCs) in the resonators, as this is where the electric field is able to interact the strongest with the TLS defects of the substrate. Narrowing the gaps, g, between fingers of width, w, increases the capacitance at the expense of increased TLS noise; larger gaps increase the overall size of the detector footprint. Results from previous attempts to produce highly sensitive detectors show that in order to reduce TLS noise in the thick volume detectors, either the capacitor finger must be separated or the overall capacitor area - and therefore the detector footprint - must increase.[69,75,111] These recommendations could be utilized to quickly optimize the capacitors for the 850 GHz detectors.

Overall, the performance of the prototype detectors was remarkable, with one of the designs very nearly achieving all the specifications. The high volume resonator, with relatively minimal modifications, could easily be adopted as the final designs for the 850 GHz detector array. What remains is the optimization of the final detector design based on the results from these prototypes.

5.6 Conclusion

The 850 GHz module will consist of approximately 45,000 TiN, polarization-sensitive, lumped-element kinetic inductance detectors, meaning the module will field more microwave kinetic inductance detectors than any other millimeter-wave receiver to date. The detectors are being designed to be read out using a multi-octave readout architecture, allowing for approximately double the multiplexing of other CCAT modules. This chapter explored the the design of prototype MKIDs, including a method of shorting inductors to modify the resonance with minimal change to the absorber architecture. Several different volumes of resonator were tested, and the resulting characterization was presented above. The feasibility of a two octave design using the inductor shorting technique was confirmed. Likewise, the tested pentalayer film showed remarkable qualities for the sheet inductance and critical temperature, enabling a relatively high volume for the resonators in a small footprint. 850 GHz MKID prototypes showed high responsivity to thermal and optical loading, and photon limited performance. However, the results showed that the sensitivity of the majority of the designs was too great, and the measured TLS noise contributed significantly to the overall noise - roughly 1/3 of the overall noise - despite being subdominant to the photon noise. The solution is using higher volume resonators, such as the 1,290 μm^3 volume, and better optimization of the capacitors with back etching to reduce the interactions with the electric field around the capacitors. Overall, the current high volume resonator design performs very near the requirements for the 850 GHz module.

Chapter 6

A Blind ^{12}CO Redshift Survey of Bright Submillimeter Galaxies

Just because a man lacks the use of his eyes doesn't mean he lacks vision.

STEVIE WONDER

This chapter presents the results of a blind millimeter-wave redshift survey of the brightest unlensed submillimeter galaxies (SMGs) from the SCUBA-2 Cosmological Legacy Survey (CLS). The 14 brightest SMGs ($S_{850\mu m}$ >11 mJy) were selected from the Lockman Hole, AEGIS, and CDF-N fields. Each of the SMGs have been identified as single sources by the Submillimeter Array (SMA). Observations were made across 12 of the 14 SMGs with the IRAM NOEMA interferometer across two tunings with a combined 85 GHz bandwidth (two SMGs had CO redshifts from previous observations). These observations, presented in Sec. 6.2, revealed at least one strong emission line for each of the galaxies. Precise spectroscopic redshifts are assigned to each of these 12 SMGs, unambiguously in five cases with two or more detected lines, and guided by photometric redshifts for the seven single line cases.[22] Results of the survey are shown in Sec. 6.4, with a discussion of the results in Secs. 6.5 & 6.6. This survey is compared against similar surveys shown in Refs. 112 and 113.

6.1 Introduction

Hundreds of dusty, star-forming SMGs have been discovered in blank-field and submillimeter continuum surveys (see Refs. 114–120), while $\sim 10^4$ SMGs have been detected from the close to 10^3 deg^2 area mapped by *Herschel*-SPIRE in the 500, 350, and 250 μm bands.[121] At higher flux limits, the South Pole Telescope (SPT) has mapped a 2500 deg^2 region,[122] and *Planck* has mapped the entire sky,[123] finding many extreme or gravitationally lensed SMGs. Ongoing efforts in submillimeter

astronomy include searches for the most luminous star-forming galaxies from 100s of deg^2 in the Universe.[124,125] Note that some of the earliest discovered SMGs in $\sim$100 arcmin^2 surveys remain the brightest, most extreme known (e.g., SMM J02399 – Refs. 126, 127; GN20 – Refs. 128, 129; and COSMOS-AzTEC1 – Refs. 119, 130).

The redshift of unlensed SMGs is generally determined through a process of using weak counterparts in the rest-frame ultraviolet (UV) and optical regime to make spectroscopic determinations,[131,132] or by combining near- and mid-infrared (IR) photometry for photometric redshift estimates.[133,134] However, since the high extinction of SMGs means they only offer faint - if any - counterparts in the optical and near-IR bands, both the spectroscopic and photometric redshift distributions remain incomplete.[134] The largest spectroscopic SMG redshift survey to date was based on radio-identified SMGs (Ref. 132). Nonetheless, radio identification may be inaccurate,[135] and may bias the redshift distribution as radio emission may remain undetected in radio maps for sources at $z > 3$. A solution is an optical spectroscopic followup to the SMGs to remove the identification bias, as has been done for sources identified by ALMA.[134,136] Regardless, this method is unable to remove the spectroscopic bias.

An alternative to optical spectroscopic followups to determine the redshift of an SMG is through observations of ^{12}CO emission lines at cm or mm wavelengths. ^{12}CO is a tracer of H_2 molecular gas, fuel for star formation, and can therefore be related to the submillimeter continuum source. Thus observations do not require any additional multi-wave identification, circumventing the numerous problems inherent to optical spectroscopy of SMGs. However, to date the sensitivity of mm-wave facilities has limited the approach to followup of bright gravitationally lensed SMGs (See Refs. 120, 137–141)

The IRAM Plateau de Bure Interferometer (PdBI) was sensitive enough to detect ^{12}CO lines in unlensed SMGs (e.g. see Ref. 142). However, its 3.6 GHz bandwidth receivers limit this approach due to the large time requirement for blind searches of ^{12}CO lines in redshift space via multiple frequency tunings. Walter et al. (Ref. 143) observed the HDF-N field with the PdBI over the full 3mm window to a similar depth as the Bothwell et al. 2013 survey,[142] requiring 110 hrs on-source. In addition to blindly detecting two faint ^{12}CO emitting galaxies, they identified the redshift of the $S_{850\mu m}$ $\sim$5 mJy HDF850.1 as $z = 5.3$. The 8-GHz instantaneous, dual-polarization bandwidth of ALMA, coupled with its sensitivity, improves this approach, but still makes it a relatively expensive

Figure 6.1: Left: Antennae of the NOEMA interferometer sited in the French Alps. Right: Antennae of the SMA interferometer sited near the summit of Maunakea. Images taken from Refs. 145 and 146 respectively.

prospect to blindly obtain ^{12}CO redshifts for even the brightest SMGs with $S_{850\mu m} \sim 8$ mJy.

What follows below outlines a blind spectroscopic survey of bright SMGs using the 16-GHz bandwidth of IRAM NOEMA with the Polyfix receiver, primarily targeting the ^{12}CO line emission in the 3mm band. This survey targets some of the brightest unlensed SMGs ever discovered in the northern CLS fields with $S_{850\mu m} > 11$ mJy in a single SMA-identified source.[23] The faintness of most of these SMGs at near-IR/optical wavelengths precluded optical spectroscopic observations (e.g., Ref. 144), despite lying in these well studied fields.

Cosmological parameters used in this work are: $\Omega_m = 0.3$, $\Lambda = 0.7$, and H = 70 km s^{-1} Mpc^{-1}; at $z = 2.82$, this corresponds to an angular scale of 7.94 kpc arcsec^{-1}, or 0.48 Mpc arcmin^{-1}.

6.1.1 The NOEMA Interferometer

The Northern Extended Millimeter Array (NOEMA) interferometer is a series of 15-m diameter antennae sited at an altitude of 2500 m. Each antenna includes high-resolution, dual-polarization receivers for 70-116 GHz (Band 1), 127-179 GHz (Band 2), 200-276 GHz (Band 3), and 275-373 GHz (Band 4). The antennas of the NOEMA interferometer can be moved via rails to a maximum baseline 'width' of 1.7 km and 'height' of 368 m, providing a resolution of 0.2 arcsecs at 230 GHz. Included within the receiver cabin is a closed cycle cryostat, which cools crucial components of the receiver (such as the SIS junctions) to ulta-low temperatures (approximately 3 K)). The wideband correlator *PolyFix* can process up to ~31 GHz of instantaneous bandwidth for up to twelve antennae, accommodating both polarizations. Observations are performed by telescope operators and staff

astronomers, who also aid in data reduction and analysis.[145] The NOEMA interferometer is shown in the left panel of Figure 6.1.

6.1.2 The Submillimeter Array

The Submillimeter Array (SMA) is an interferometer consisting of a series of 8 radio dishes sited near the summit of Maunakea. As shown in the right panel of Figure 6.1, these 8 polarization-sensitive antennae provide a baseline of roughly 500 m across. Maunakea, rising $\sim$4 km above sea level, provides far greater atmospheric transmission across multiple observing bands in the range of 180-900 GHz. Like the NOEMA interferometer, the receiver electronics are housed in a closed cycle cryostat and cooled to $\sim$4 K. The SMA also includes wide-band correlators, capable of handling the demand of the several bands of each antenna with both polarizations.[147] Thus the SMA is a powerful tool for studying topics such as the birth of planets, stars, and galaxies.[146]

6.2 Observations

As highlighted above, the sources were identified with SCUBA-2 as part of a followup of 6 different extragalactic fields in the SCUBA-2 CLS. From the observations, the brightest sources in the northern 850 μm survey with $S_{850\mu m} > 11$ mJy in a single identified source were selected as targets for blind redshift followup with NOEMA Polyfix. Figure 6.2 shows cutouts of an example source (CDFN-1) at SCUBA-2 and *Spitzer* wavelengths, with a clear identification at the various wavelengths. Sources were observed with both NOEMA and SMA.

6.2.1 NOEMA Observations

The IRAM-NOEMA observations were taken in C or D configuration using the 10-12 antenna sub-arrays, with properties of the observing runs and resulting synthesized beam sizes summarized in Table 6.1. These observations utilized pointing centers defined by the SMA detections of each source at 850 μm. Flux calibration was achieved by observing various calibrators (3C273, 3C345, B0234+285, B1749+096). Data were processed using the most recent version of the GILDAS software. The cubes were resampled in 90 km s^{-1} channels, and imaged using the GILDAS suite *mapping*, adopting natural weighting. To obtain flux measurements, the visibilities were deconvolved using the CLEAN task with natural weighting, and the corresponding primary beam correction were

Table 6.1: Observation details and derived metrics for each of the sources in the fields.

source	RA	Dec	Beam	$S_{250\mu m}$	$S_{350\mu m}$	$S_{500\mu m}$	$S^{\dagger}_{850\mu m}$	SFR‡	z
	(GHz)	(hr)	(mJy)					($M_{\odot}$ yr^{-1})	
CDFN-1	12:35:55.889	+62:22:39.15	2x1.9”	30.3±3	41.0±4	47.8±6	17.0±1.9	2550±290	3.1493
CDFN-2	12:35:51.467	+62:21:47.38	5x4”	19.3±3	29.7±4	34.8±6	15.9±1.6	2390±240	4.4216
CDFN-4	12:37:30.736	+62:12:59.77	5.5x3”	48.7±3	55.0±4	46.8±6	14.9±0.9	2240±130	1.6204
CDFN-8	12:36:27.182	+62:06:05.82	2.2x3.1”	9.6±3	22.7±4	30.3±6	11.5±0.7	1730±110	4.1439
LOCK-1	10:46:45.083	+59:15:41.95	5x4”	27.2±3	36.6±4	30.0±6	12.3±1.1	1850±160	2.3195
LOCK-2	10:46:35.860	+59:07:48.15	6.4x5”	35.7±3	39.0±4	37.3±6	12.2±1.2	1830±180	2.2436
LOCK-4	10:48:03.624	+58:54:21.30	6x6”	58.4±3	70.0±4	54.7±6	14.1±1.5	2120±220	2.5545
LOCK-16	10:44:56.706	+58:49:59.78	4x5”	14.3±3	21.7±4	24.2±6	11.9±1.3	1790±190	2.7199
AEG-2	14:15:57.527	+52:07:12.40	3.2x2”	19.0±3	36.0±4	38.0±6	13.8±1.5	2070±230	3.6675
AEG-3	14:15:47.066	+52:13:48.38	3x2.1”	48.3±3	53.7±4	65.4±6	16.4±1.3	2460±190	4.0323
AEG-4	14:19:14.246	+53:00:33.58	3.4x2.2”	23.3±3	25.4±4	21.3±6	11.1±1.1	1670±170	2.6884
AEG-5	14:19:19.983	+52:56:09.05	2.5x3’	27.1±3	35.7±4	25.6±6	14.4±1.2	2160±180	3.2574

†SMA measurements.

‡using SFR = 150$\times S_{850}$.

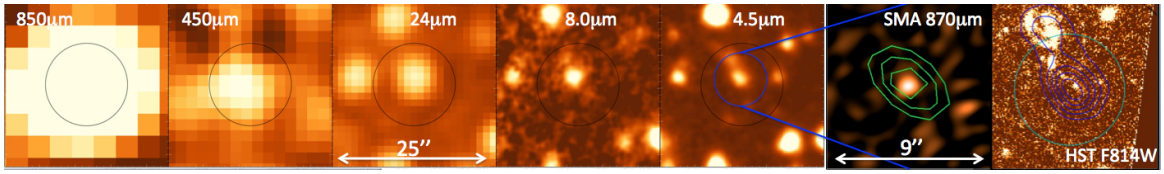

Figure 6.2: Sample multi-wave cutout of one of the sources: CDFN-1. **Left to Right**: five cutout images 25″ on a side of the longer wavelength data (850μm, 450μm, 24μm, 8μm, 4.5μm), highlighting the identification of the SMG with an IR-luminous component (black circle shows the 15″ SCUBA-2 beam size). **Second from Right**: a 9″×9″ zoom in from the SMA compact configuration 870μm map, with a $\sim 4''$ synthesized beam with PdBI ^{12}CO(4–3) contours overlaid. All of the SCUBA-2 flux (17 mJy) is recovered in a single compact component, unresolved with a 1.5″ SMA beamsize. No other significant sources are detected within the 15″ diameter of the SCUBA-2 beam. **Far Right**: 9″ cutout of the *HST*-ACS F814W image centred on the SMA detection, with IRAC ch-2 contours overlaid, shows CDFN-1 to be well identified with a faint tad-pole like $I_{AB} \sim 26$ galaxy, which is marginally detected in ground based imaging ($\mathcal{R} = 26.1$).

applied to the datacubes. Note that the primary beam corrections are negligible at the small $< 0.5''$ offset of the NOEMA position from the SMA position. Spectral scans for each of the sources is presented in Figures 6.3 to 6.5, each with a zoomed in image of the lowest detected CO transition.

6.2.2 SMA observations

SMA observations were obtained for all sources as part of a followup campaign of the brightest 100 sources in the SCUBA-2 CLS survey, and are detailed in Hill et al. 2019 (Ref. 23). These observations in the compact configuration (beam sizes $\sim 2''$) in good weather ($\tau_{225\mathrm{GHz}} \sim 0.08$) were obtained with the upper sideband (USB) tuned to 345 GHz, and combined with the lower sideband (LSB) for an effective bandwidth of ~ 4 GHz at 340 GHz, which yielded a final rms of ~ 1 mJy. The pointing centre was the same as that for the PdBI observations described above, with deviations being negligible.

6.3 Redshift Determination

In a blind redshift survey, the simplest method to unambiguously determine redshift is through the detection of either 2 CO lines or one CO line and 1 [CI] line in the given band of measurement. In the case that a galaxy lies at redshift z$>$ 3, it is expected that all sources will meet this criterion. However, galaxies at z$<$ 3 will exhibit only 1 line, presenting ambiguity in identifying the transition of the line and, therefore, the redshift. A method of probabilistically determining the redshift based on the spectral energy distribution (SED) of a given source has been developed as part of the

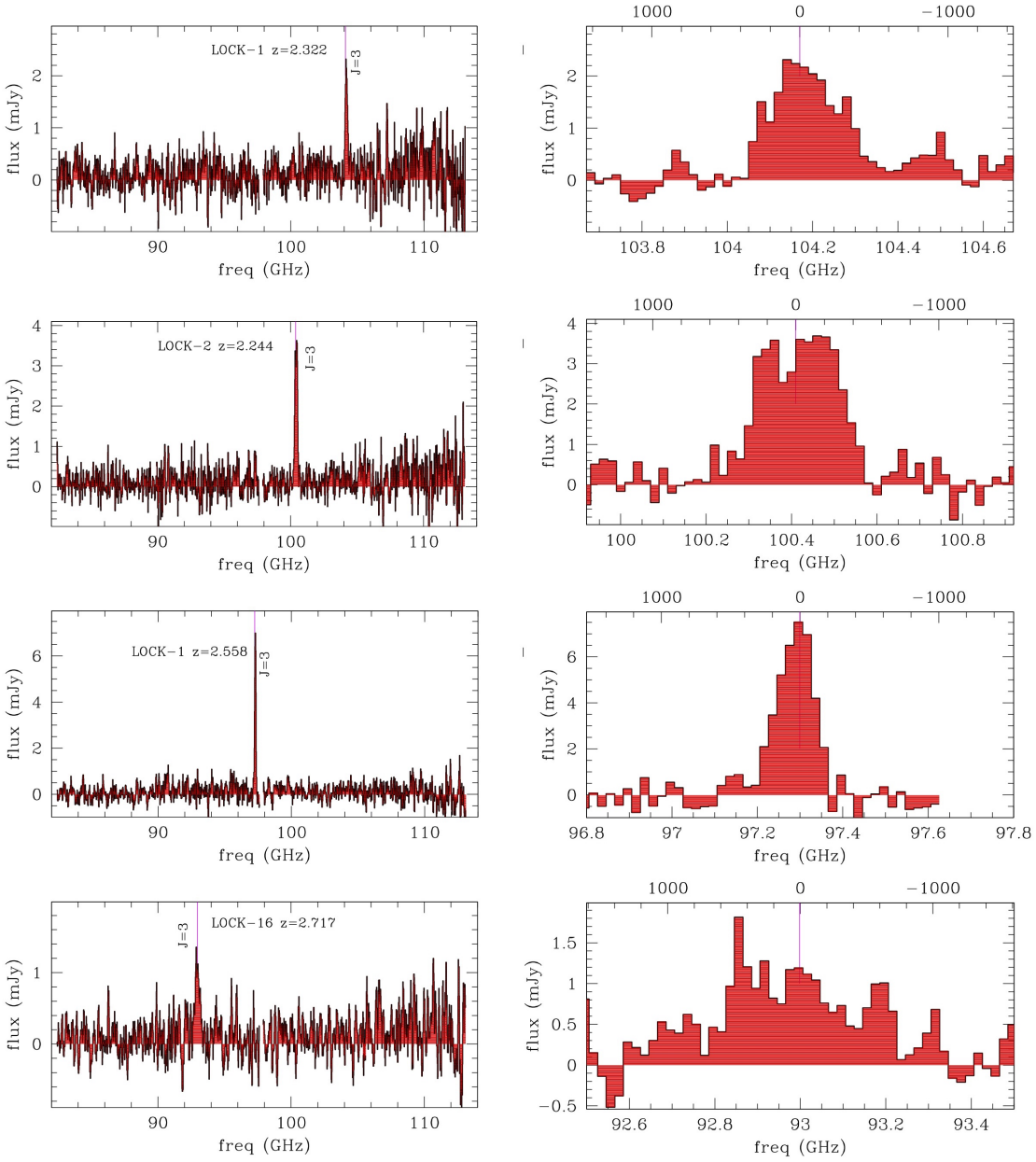

Figure 6.3: Spectral scans (left) and zoomed in lines of lowest transition of CO detected in the spectral scans for Lockman sources. ^{12}CO and $[CI]_{2-1}$ emission lines are marked, the former corresponding to ^{12}CO(5–4). For the single line identifications, all other possible redshifts have been fit, and no other significant lines are found to lie near the implied frequencies of other lines.

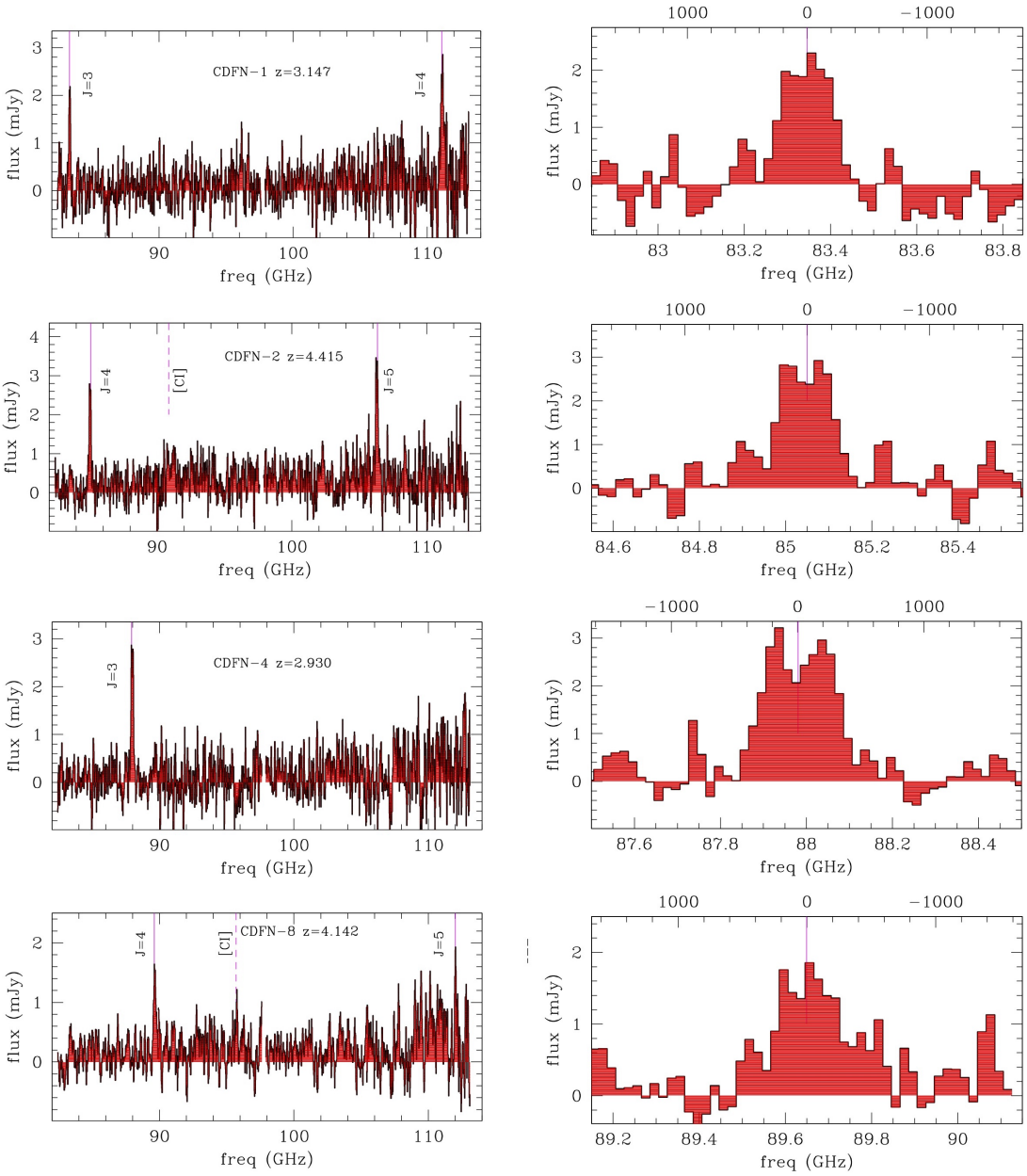

Figure 6.4: Spectral scans (left) and zoomed in lines of lowest transition of CO detected in the spectral scans for CDF-N sources. ^{12}CO and $[CI]_{2-1}$ emission lines are marked, the former corresponding to ^{12}CO(5–4). For the single line identifications, all other possible redshifts have been fit, and no other significant lines are found to lie near the implied frequencies of other lines.

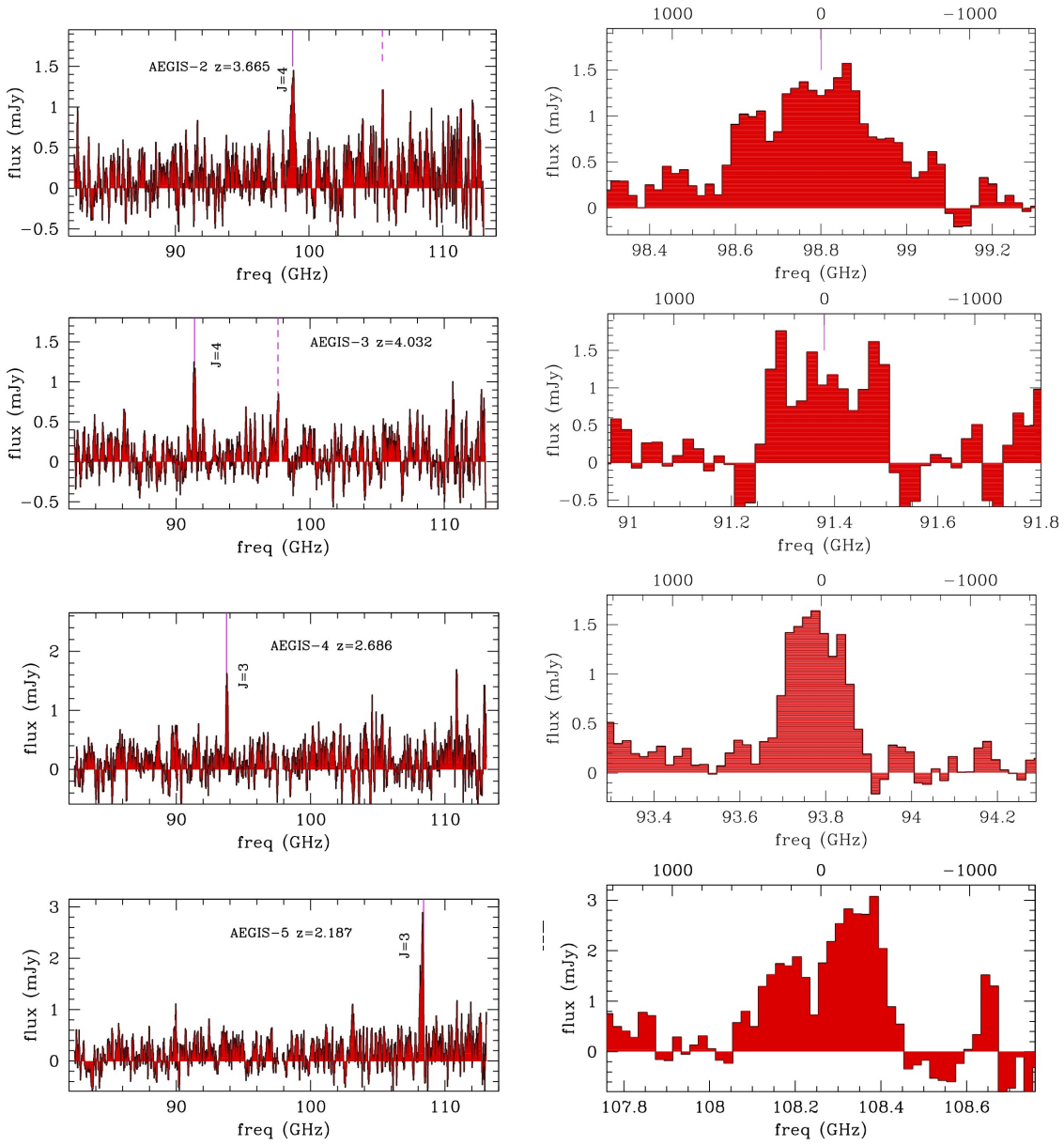

Figure 6.5: Spectral scans (left) and zoomed in lines of lowest transition of CO detected in the spectral scans for AEGIS sources. ^{12}CO and $[CI]_{2-1}$ emission lines are marked, the former corresponding to ^{12}CO(5–4). For the single line identifications, all other possible redshifts have been fit, and no other significant lines are found to lie near the implied frequencies of other lines.

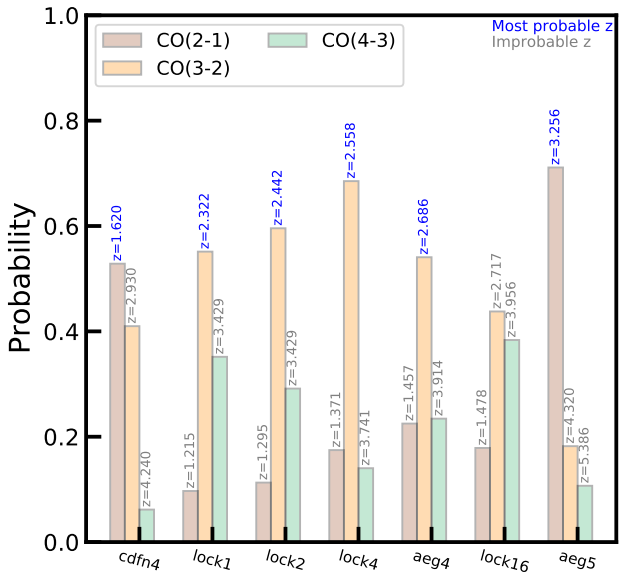

Figure 6.6: Quantized redshift possibilities and their probabilities for the seven sources with only one line detection, assuming the line is ^{12}CO. In some cases the probability is similar between two CO transitions, indicating that the SPIRE-based photo-z lies near midway between these two possible CO-redshifts.

MAGPHYS code.[148] This method has been used in cases where inability to identify lines introduces ambiguity (e.g. Ref. 22). Application of the method uses a fit of the SED to generate a photometric redshift, which is then applied to the observed line frequency to constrain the redshift of the line, aiding in identification.

Of the 12 sources included in this survey, seven measured spectra included a single measured line, which was assumed to be from a CO transition; the available transitions in this range are CO(2-1), CO(3-2), and CO(4-3). MAGPHYS was used to determine probablility distibution functions (PDFs) for each of these sources. Results of the analysis are presented in Figure 6.6. Each of the measured lines were assigned a redshift based on the most probable results. In the case where the probablity is similar between two lines, it is assumed that the photometric redshift lies between two possible CO transitions. The final redshift values, including both the unambiguous and ambiguous spectra, are presented in Table 6.1

6.4 Results

A composite of all spectral scans (2 tunings) towards Lockman, CDF-N, and AEGIS sources at a velocity resolution of 60 km s^{-1}, are shown in Figures 6.3 to 6.5. For the given frequency band of

NOEMA, the ^{12}CO and [CI] are the strongest lines.[149] In each of the spectra in Figures 6.3 to 6.5, ^{12}CO and $[CI]_{2-1}$ emission lines are marked, including those determined from a single measured CO line as detailed above. For these single line identifications, all other possible redshifts were fit, with no other significant lines found to lie near the implied frequencies of other lines.

Once identified, each of the lines were fit with a gaussian in order to provide values for the central frequency, ν_{obs}, and FWHM. The line luminosity, L'_{line}, for each line was calculated as[150]

$$L'_{line} = \frac{c^2}{2k_B}\left(\frac{D_L}{\nu_{obs}}\right)^2 \frac{F_{line}}{(1+z)^3}, \tag{6.1}$$

where c is the speed of light, k_B is the Boltzmann constant, D_L is the luminosity distance, and F_{line} is the integrated line strength. The line flux may then be used to determine parameters such as the gas mass, M_{gas} of the source in the case of CO lines:

$$M_{gas} = \alpha L'_{CO}, \tag{6.2}$$

where α is a conversion factor with standard values. Notice, however, that deviations in α occur due to difference in the physical conditions of the molecular gas.[151] A theoretical value of $\alpha = 0.8\,M_\odot\,(K\,km\,s^{-1}\,pc^2)^{-1}$ is typically applied to luminous infrared galaxies,[152,153] while a standard value based on the Milky Way galaxy[149] is $4.6\,M_\odot\,(K\,km\,s^{-1}\,pc^2)^{-1}$. For this work the former value is adopted over the latter.

It is crucial to note that Equation 6.2 utilizes $L'_{CO} = L'_{CO(1-0)}$ for consistency across all measured lines, meaning that a conversion is required. The process of this conversion, detailed in Carilli and Walter (2013),[149] is linear with the conversion factor, α_{CO}, varying depending on the CO transition. Dividing $L'_{CO(j-(j-1))}$ by the appropriate value of α_{CO} gives an equivalent value for $L'_{CO(1-0)}$. Values for α_{CO} also vary based on the type of source being analyzed. For SMGs, values for α_{CO} are 0.66, 0.46, and 0.39 for the CO(3-2), CO(4-3), and CO(5-4) transitions, respectively. Once L'_{line} values are converted, Equation 6.2 can be used to estimate M_{gas}. The measured and derived parameters based on analysis of the spectral lines are presented in Table 6.2.

Interestingly, there are deviations in M_{gas} calculated between lines from the same source, in particular CDFN-8. Ref. 142 showed a typical line flux ratio for CO emissions of $r_{53} = 0.62$ across

Table 6.2: Parameters derived from the lines measured for each of the sources.

Source	Line	Flux (Jy km/s)	FWHM (km/s)	$L'^{\dagger}$ K km s^{-1}pc^2	$L'^{\dagger}_{CO}$ K km s^{-1}pc^2	$M^{\dagger}_{gas}$ $M_{\odot}$
CDFN-1	CO(3-2)	1.085±0.148	473±65	5.44±0.74	8.2±1.1	6.59±0.90
CDFN-1	CO(4-3)	1.658±0.168	800±78	4.64±0.47	10.1±1.0	8.07±0.82
CDFN-2	CO(4-3)	1.593±0.150	471±65	7.69±0.72	16.7±1.6	13.4±1.6
CDFN-2	CO(5-4)	1.852±0.144	559±51	5.72±0.44	14.7±1.1	11.74±0.90
CDFN-2	[CI]	0.564±0.183	760±240	2.37±0.77	–	–
CDFN-4	CO(2-1)	2.000±0.177	703±68	8.90±0.79	10.47±0.88	9.51±0.80
CDFN-8	CO(4-3)	0.973±0.174	700±130	4.25±0.76	9.2±1.7	7.4±1.3
CDFN-8	CO(5-4)	0.529±0.100	280±150	1.48±0.28	3.79±0.72	3.03±0.57
CDFN-8	[CI]	0.242±0.068	400±200	0.75±0.19	–	–
LOCK-1	CO(3-2)	1.073±0.141	516±66	3.21±0.42	4.86±0.64	3.89±0.51
LOCK-2	CO(3-2)	2.446±0.161	665±57	8.01±0.53	12.13±0.80	9.70±0.64
LOCK-4	CO(3-2)	2.317±0.115	311±26	8.19±0.41	12.41±0.62	9.93±0.50
LOCK-16	CO(3-2)	1.483±0.235	1340±240	5.83±0.92	8.8±1.4	7.06±1.1
AEG-2	CO(4-3)	1.164±0.197	980±180	4.19±0.71	9.1±1.5	7.29±1.2
AEG-2	[CI]	0.301±0.131	760±240	1.28±0.95	–	–
AEG-3	CO(4-3)	1.283±0.187	590±130	4.74±0.91	10.3±2.0	8.2±1.6
AEG-3	[CI]	0.313±0.132	650±290	1.93±0.81	–	–
AEG-4	CO(3-2)	0.728±0.139	450±110	2.80±0.54	4.24±0.82	3.39±0.65
AEG-5	CO(4-3)	1.281±0.149	613±66	3.81±0.44	8.28±0.95	6.62±0.76

†Values $\times 10^{10}$.

a survey of 30 SMGs. CDFN-8, however, has a measured line ratio of $r_{53} \simeq 0.35$, almost half the typical value, while CDFN-2 has a measured line ratio of $r_{53} \simeq 0.74$.

A useful relation derived from the line luminosity is its relation to the FWHM, as it is a measure of the correlation between the gas mass and the galaxy dynamics.[22,138] Results from this survey show a median $L'_{CO(1-0)}$ of $(9.2\pm3.5)\times10^{10}$ K km s^{-1}pc^2 and FWHM of 590 ± 260 km s^{-1} (see Figure 6.7). Variations of $L'_{CO(1-0)}$ with the FWHM of CO lines are fit with a model of the form[22]

$$\log_{10} L'_{CO} = a \log_{10} (\mathrm{FWHM}/\mathrm{FWHM}_{\mathrm{med}}) + b, \tag{6.3}$$

where a=0.29 ± 0.08 and b=10.948 ± 0.002 from these results.

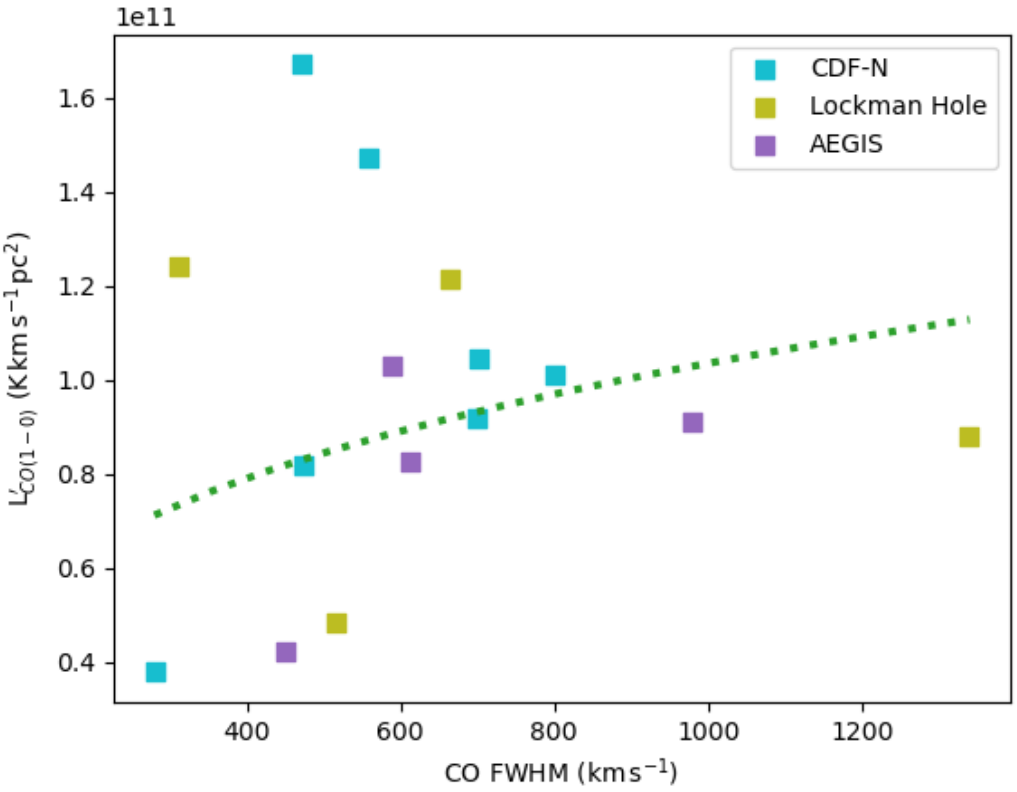

Figure 6.7: CO line full-width at half-maximum as a function of CO line luminosity, $L'_{CO}(1-0)$. The fit generated values of a=0.29 ± 0.08 and b=10.948 ± 0.002. Sources were converted from higher CO transitions to CO(1-0) using the method outlined in Carilli and Walters (Ref. 149).

As part of this survey, the redshift distribution of the SMGs was analyzed focusing on the brightest sources. The median redshift for this survey was found to be z= 3.0 ± 0.7, though there were considerable variations between each of the fields. Consequently, the fields were analyzed separately to highlight any further differences. These were in turn compared against the brightest sources, defined by $S_{850} > 10$ mJy. Comparison of the median redshift values are presented in Table 6.3.

Stach et al. (2019) reported a linear trend between S_{850} and redshift.[112] Continuation of this study has continued in other fields (e.g. Refs. 22, 113, 154). In each study a linear fit is applied to the relation between S_{850} and redshift, with the gradient presented as a means of constraining the variation between the two. Figure 6.8 shows the median redshift of each of the sources as a function of their 850 μm flux densities (S_{850}) distinguished by field, and includes the prescribed linear fit. Analysis of the redshift gradient includes the brightest sources ($S_{850} > 10$ mJy) from the AS2UDS and AS2COS surveys (Refs. 112 and 113, respectively). Measured values for the gradient

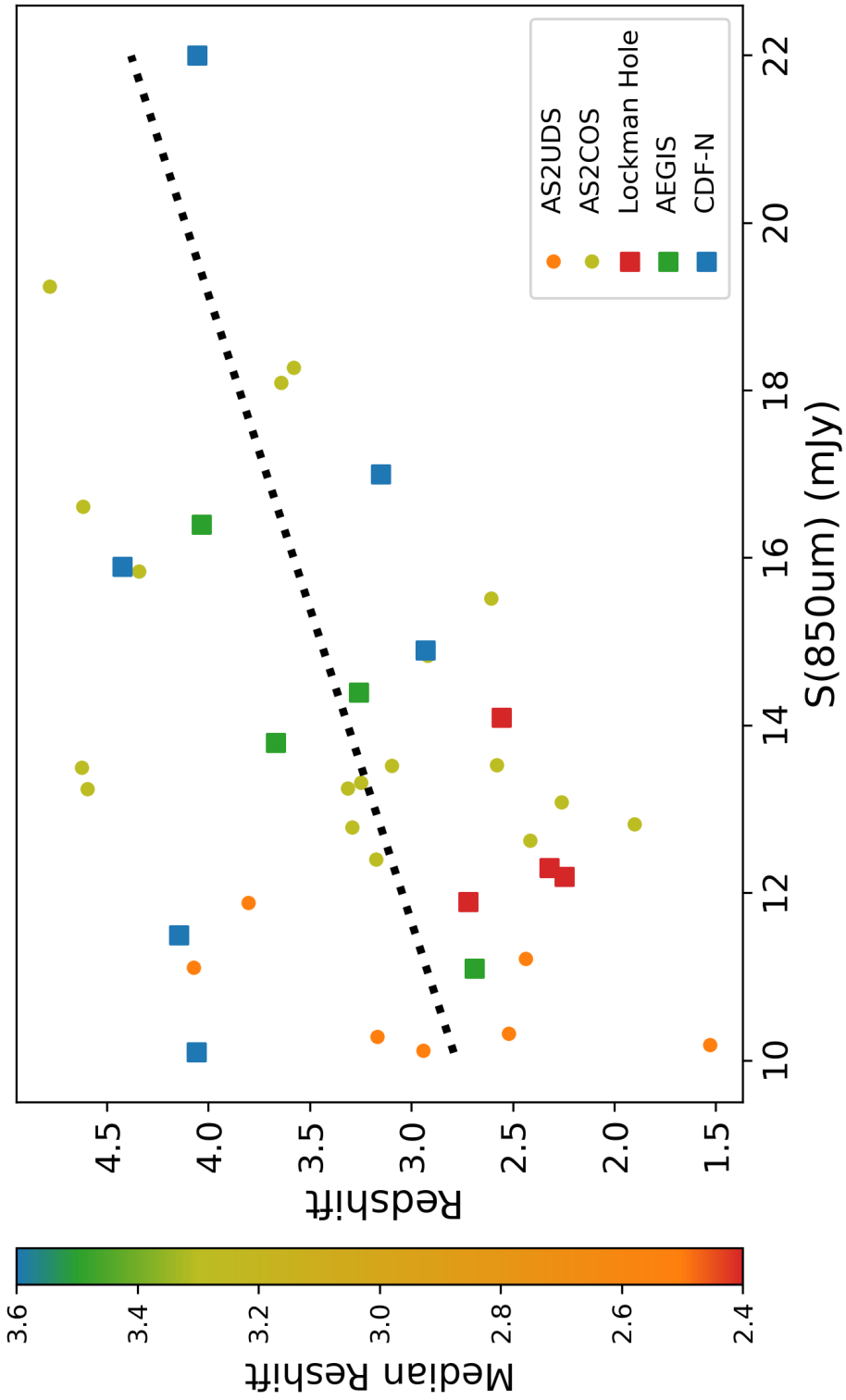

Figure 6.8: Median redshift of each of the sources as a function of their 850 µm flux densities (S_{850}) distinguished by field. Also included are the brightest sources ($S_{850} > 10$ mJy) from the AS2UDS and AS2COS surveys (Refs. 112 and 113, respectively). A linear fit to the combined sources yields a gradient of 0.11 ± 0.04. However, each field individually shows a unique gradient.

Table 6.3: Median redshift and measured gradient of the relation between 850 µm flux densities and redshift for each of the fields. Compare with Figure 6.8.

Field	z	Gradient mJy^{-1}
AS2COS	3.3±0.9	0.20±0.09
AS2UDS	2.5±0.9	0.35±0.25
AEGIS	3.5±0.5	0.24±0.07
CDF-N	3.6±0.6	-0.12±0.20
Lockman	2.4±0.2	0.03±0.15
Combined	3.0±1.0	0.11±0.04

are given in Table 6.3. As with the median redshifts for the fields, there is considerable variation in the gradient between each field. The total gradient across all the surveys, limited to the brightest sources, is 0.11±0.04.

6.5 Gas dynamics

As mentioned above, the L_{CO}–FWHM relation provides a mechanism for measuring the correlation between the gas mass and the galaxy dynamics.[138] The median relation valued of $L'_{CO(1-0)}$ and FWHM for this survey were found to be $(9.2\pm3.5)\times10^{10}$ K km s^{-1}pc^2 and 590±260 km s^{-1}, respectively. Values of $L'_{CO(1-0)}$ and FWHM have been measured in other surveys as: $(4.5\pm1.0)\times10^{10}$ K km s^{-1}pc^2 and 500±60 km s^{-1} from Bothwell (2013);[142] and $(6.7\pm0.5)\times10^{10}$ K km s^{-1}pc^2 and 540±40 km s^{-1} from Birkin (2021).[22] The greater line luminosities imply that the sources in this survey are more gas-rich than those from Bothwell and Birkin.

Figure 6.7 depicts the CO line luminosity as a function of FWHM. Note that the line luminosities values have been converted from their higher CO transitions (seen in Table 6.2) to the CO(1-0) transitions using the method defined by Carilli and Walters (see Ref. 149). These values were fit using the relationship defined in Equation 6.3, giving values of 0.29 ± 0.08 and 10.948 ± 0.002 for a and b, respectively. Similar values were obtained by Birkin et al. (2021),[22] where they measured a = 1.7±0.3 and b = 10.93±0.05. These values are roughly comparable, particularly for b, though there is some deviation in measured values for a in this fit. Under the assumption that line widths are representative of disc dynamics, the galaxy mass - reflected by $L'_{CO(1-0)}$ - should increase with the square of the rotational velocity - the CO FWHM. While the measurements made by Birkin et

al. (2021) seem to correspond to this relationship, the values from this survey do not match this relationship. Given that there is significant dither both between and within fields, this implies that the brightest sources may have line widths not directly reflected by disc dynamics.

In this survey roughly 60% of the sources display double-peaked profiles, which suggests a circumnuclear molecular toroid. As many of the sources have a large star formation rate (Table 6.1), such a stable molecular gas distribution would imply a high gas excitation. However, observed line ratios in this survey are low compared to well-studied nearby starburst galaxies NGC 253 and M 82.[155] An alternative is that the two line peaks may represent two disk components merging, individually unresolved. A ring-like rotating disk distribution of gas was strongly endorsed as an explanation for another similar double-peaked SMG, SMM J02399-0136 (Ref. 156), although it has been shown from multi-frequency, high-resolution line mapping observations that the system comprises a multiple merger.[127] With the information available from this survey, the dynamics indicate that several of the sources may represent merger systems and/or rotating disks.

6.6 Redshift Distribution

The median redshifts for each of the fields, including the brightest sources from the AS2UDS[112] and AS2COS[113] surveys, is presented in Table 6.3, where it is clear the median redshift of the sources varies between fields. Furthermore, the gradient of the redshift is shown to vary greatly between fields. This is counter to the results shown by Stach et al. (2019), Simpson et al. (2020), and Birkin et al (2020), where gradient values of 0.09 ± 0.02 mJy^{-1}, 0.06 ± 0.01 mJy^{-1}, and 0.07 ± 0.01 mJy^{-1} are respectively reported, which support a positive correlation between S_{850} and redshift proposed in the literature.[157–159] Previous explanations for this effect attribute this relationship to more massive galaxies forming earlier, referred to as downsizing.[160] However, when limited to the brightest sources ($S_{850} > 10$ mJy) this relationship appears to fail as each individual field exhibits a unique gradient.

As a followup to this finding, simulations were performed using a catalogue of submillimeter sources using Simulated Infrared Dusty Extragalactic Sky (SIDES).[161] SIDES is used to generate a catalogue of simulated galaxies in the infrared domain, including continuum and line features. A $7^\circ \times 7^\circ$ region was simulated, with information on parameters such as luminosity and flux density. As depicted in Figure 6.9, a series of $0.5^\circ \times 0.5^\circ$ representative 'fields' were selected at random

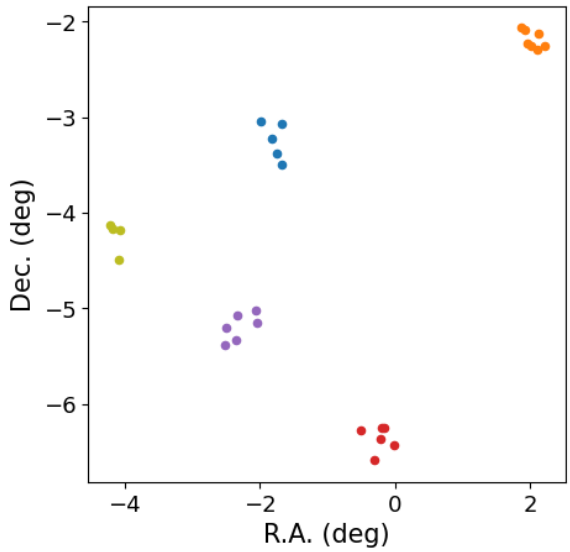

Figure 6.9: Sample fields used for a simulation. These particular fields correspond to the top left panel of Figure 6.10.

across the simulated region, and all but the brightest sources were removed, as well as any sources with redshift z<1. The gradient of each field, shown in Figure 6.10, was then measured and compared against the total. This process was repeated for multiple trials, with the results presented in Table 6.4. Finally, the entire dataset was analyzed for all 616 potential sources across the entire 49 $\deg^2$ field which met the above criteria (Figure 6.11). The measured gradient was found to be 0.036 ± 0.013 mJy^{-1}.

Across all the measured and simulated high-luminosity SMGs presented in this study, which includes portions of the AS2COS and AS2UDS surveys, values for the redshift gradient differ significantly from previous published work in almost all cases. Stach et al. (2019) suggest that the model employed by Béthermin et al (2015) (Ref. 162) tends to under-predict the median redshift. However, this accounted for a $\Delta z = -0.2$ offset between the model and survey results,[112] which is not sufficient to account for the deviations in the simulations. Furthermore, the fluctuations in the gradient seen in the simulations echo the variations presented in this survey, particularly CDF-N, which exhibited a negative gradient. Hoowever, the simulations show no appreciable difference in the median redshift between the measured fields, counter to what was observed in this survey.

Recall that the overall gradient for all the combined measurements was 0.11 ± 0.04 mJy^{-1}, this value, along with the combined value for each of the simulations approaches the ranges for previ-

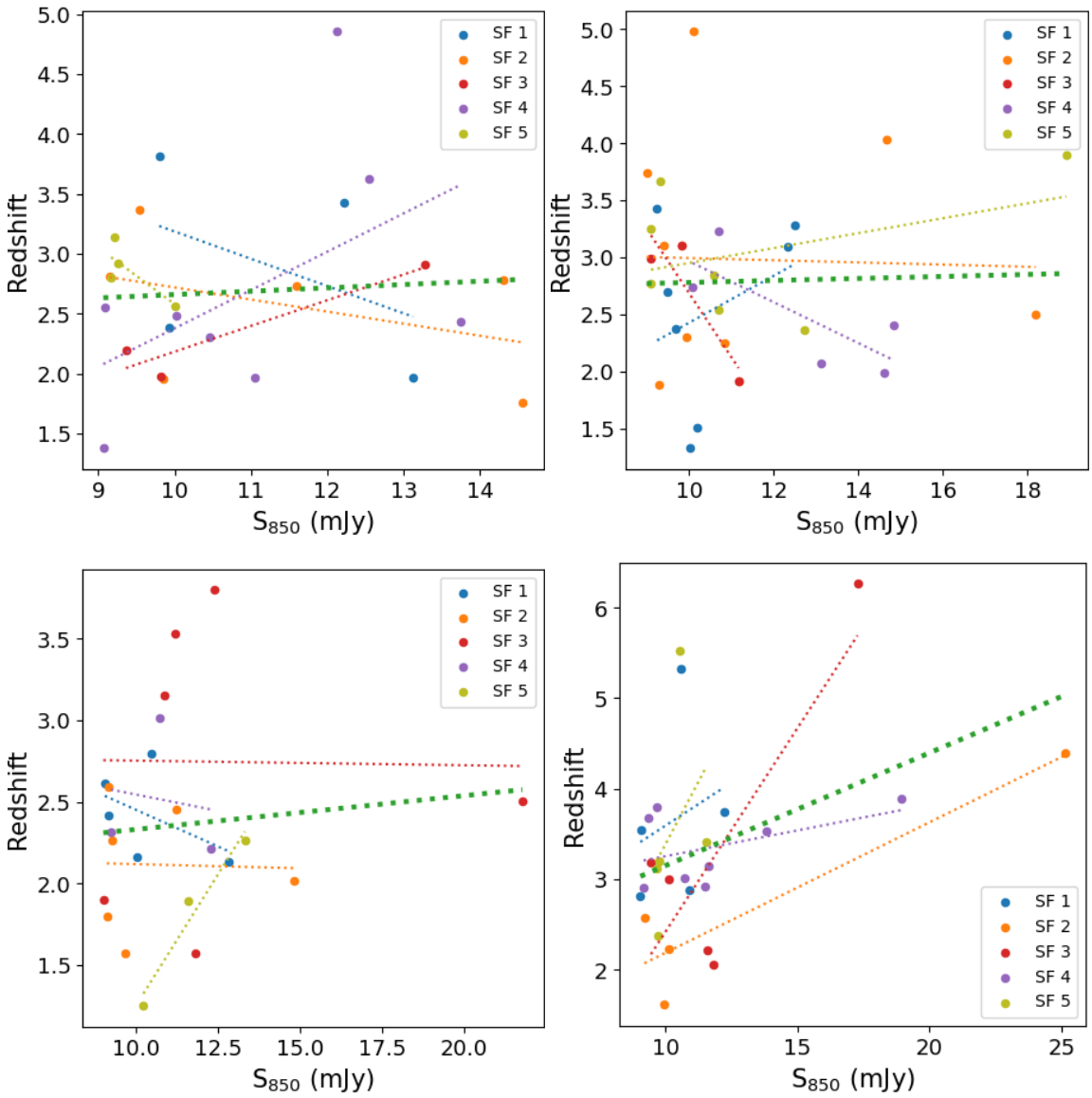

Figure 6.10: Median redshift of each source as a function of S_{850} distinguished by fields across four different simulations.

Table 6.4: Simulation results of the measured gradient of the relation between S_{850} and redshift for each of the fields. Compare with Figure 6.10.

Field	Simulation 1	Simulation 2	Simulation 3	Simulation 4
SF1	-0.23±0.33	0.21±0.26	-0.09±0.10	0.19±0.42
SF2	-0.10±0.11	-0.01±0.12	-0.01±0.09	0.14±0.04
SF3	0.21±0.07	-0.56±0.27	-0.003±0.099	0.45±0.19
SF4	0.32±0.23	-0.18±0.09	-0.04±0.28	0.06±0.05
SF5	-0.47±0.27	0.07±0.07	0.32±0.07	0.55±0.78
All	0.03±0.09	0.01±0.06	0.02±0.05	0.12±0.05

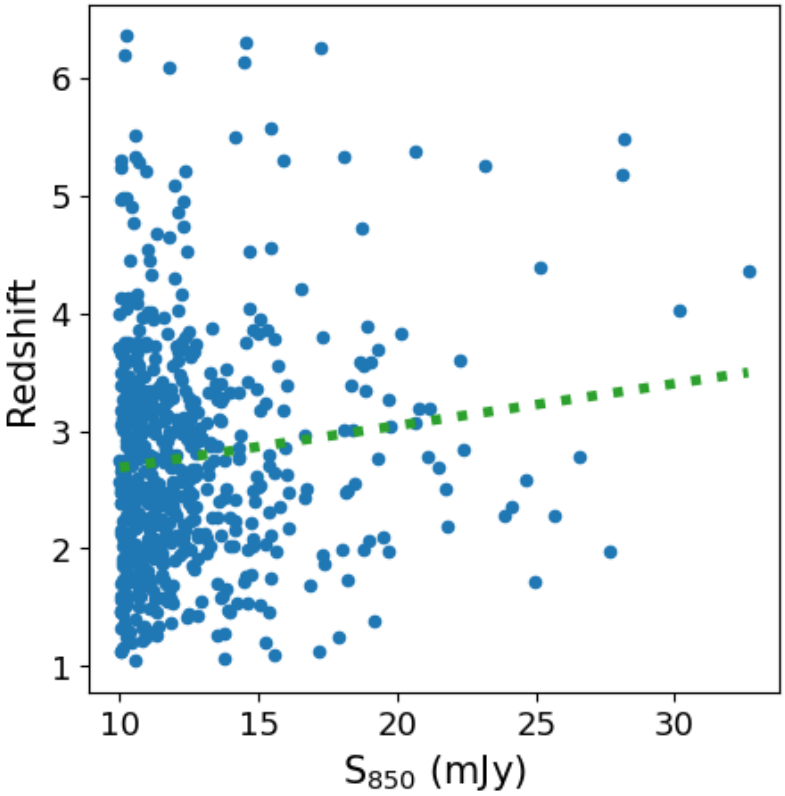

Figure 6.11: Median redshift of each source as a function of S_{850} for all potential sources across the entire simulated 49 deg^2 field. The measured gradient utilizing all 616 simulated bright sources ($S > 9$ mJy) at $z > 1$ was found to be 0.036 ± 0.013.

ously published values of the gradient. This implies that the variations seen in the gradient represent some form of structure in the Universe, with the homogeneity of the Universe dominating at larger fields and with a greater number of sources. Another explanation could be that the sources chosen for this survey represent extremes, with potentially 60% representing mergers and, as such, are not truly representative of the typical SMG found in other surveys. Likewise, the relative rarity of such bright SMGs means the data could potentially be skewed by a few bright mergers. Consideration needs to be made moving forward in defining the exact nature of these sources - be they merger systems and/or rotating disks, the field dependent nature of the redshift gradient and the potential impact of cosmological structure, and the variations in the median redshift seen for highly luminous sources.

6.7 Conclusion

This chapter presented the results of a blind survey using NOEMA to measure reliable redshifts for a sample of the 12 brightest sources identified by the SMA[23] in three of the of the SCUBA-2 CLS northern fields (Lockman Hole, AEGIS, and CDF-N). The project demonstrates the ability to efficiently derive redshifts and global properties of high-z galaxies using the PolyFix correlator and broad bandwidth recievers on NOEMA. Of the twelve sources targeted, each source had CO lines detected with sufficient signal-to-noise ratio, along with a measured continuum. Two CO lines were detected for five of the twelve targets, allowing for unambiguous redshifts. For the remaining sources with only one CO line detection, a technique relying on photometric results allowed the CO line to be reliably attributed to one of 3 possibilities. The derived spectroscopic redshifts are in the range $2.08 < z < 4.05$ with a median value of $z = 2.9 \pm 0.6$

A preliminary study of the differing sources and fields was presented. From the observations it was seen that many emission lines have broad widths between 500 and 1100 km/s, with a mean value for the CO FWHM of 700$\pm$300 km/s and a median of 800 km/s. Furthermore, roughly 60% of the sources display double-peaked profiles indicative of merger systems and/or rotating disks. Examination and comparison of the gradient of the redshift distribution with respect to S_{850} led to a combined measurement of 0.11 ± 0.04, which is in rough agreement with prior work.[22,112] However, each field showed varying degrees of deviation from both this overall gradient and the median redshift, an indicator of overall randomness to this constraint within a given field. This finding was confirmed against simulations.

The observations presented in this study have enabled the first systematic measurement of redshifts of high-z, 850 µm-selected galaxies using NOEMA. Measurements of a larger and complete sample of galaxies selected from the CLS will provide a useful database for exploring in detail the properties of these sources.

Chapter 7

Conclusion

Home is behind, the world ahead,
And there are many paths to tread
Through shadows to the edge of night,
Until the stars are all alight.

The Fellowship of the Ring

J.R.R. TOLKIEN

This dissertation highlighted the technological development of astronomical instrumentation via participation in the Cerro Chajnantor Atacama Telescope (CCAT) collaboration. The Prime-Cam instrument for CCAT-prime will include state-of-the-art, photon-noise-limited kinetic inductance detector (KID) arrays,[163] allowing for single frequency, dual polarization measurements in given atmospheric windows. A technique for designing two-octave MKIDs has been developed and applied to the 850 GHz module for Prime-Cam as part of this work. The integration and characterization of components necessitated the development of a cryogenic testbed with a suitable instrument suite. Results of the work include the finalization of the optical and mechanical design of the 850 GHz module; the design, development, and successful application of prototype MKID detectors for the 850 GHz; and a preliminary glimpse into potential issues arising from existing models for the relationship between 350 GHz flux densities and redshifts for the brightest SMGs.

7.1 Dissertation Summary

The first chapter presented the motivation for FIR/Submillimeter astronomy, as well as for the 850 GHz module of Prime-cam. Chapter 2 presented the optical and cryogenic design of the 850 GHz module for Prime-Cam, highlighting the challenges and success of the four-lens design. An outline of the relevant theory of MKIDs was given in Chapter 3, with particular focus on the respon-

sivity and sensitivity parameters one uses to model the performance of a detector. The cryogenic testbed for characterizing MKIDs is presented in Chapter 4, presenting preliminary results from the RF chain and designs of the the test box used to perform optical characterization of prototype MKIDs. Design and results from novel high-density, photon-noise-limited, multi-octave submillimeter MKIDs are presented in Chapter 5; these results confirm the multi-octave design is a success. Lastly, the results from a blind ^{12}CO redshift survey of bright SMGs is given in Chapter 6. These results highlight a potential discrepancy in the current understanding in the relationship between flux density and redshift for hyper luminous infrared galaxies (HyLIRGs).

7.1.1 Optical Design

The central goal for the 850 GHz module design is maximizing mapping speed while maintaining diffraction-limited image quality across the majority of the field of view (FoV). To maximize the mapping speed of the instrument module, a four-lens design was selected over a five-lens design, a decision which stems from a study of the trade-off between adding lenses to increase the field of view of the module with a reduction in throughput due to additional losses from the lenses. A consequence of this choice was a reduction of the FoV to 1.1° (as opposed to the 1.3° maximum), though this resulted in the highest Strehl ratio over the largest area of the FoV possible. The result is a system with a Strehl ratio > 0.8 across nearly the entire FoV. This is accomplished in part by allowing a maximum angle of incidence of 4°. In order to increase the mapping speed to match that of a module with a 1.3° FoV, the module must include roughly 45,000 MKIDs across three silicon feedhorn arrays, which corresponds to a pixel pitch of 1.45 mm and an Fλ spacing of 1.48. Since the value of Fλ is reduced from the baseline value of 2.0, the system will be less susceptible to the effects of field curvature. Thus the design is a robust solution to the complex parameter space and constraints described above.

This optical design has undergone a design review chaired by third-party researchers. From this design review, the decision to utilize a four-lens design rather than a three- or five-lens design was confirmed and upheld. While this design fails to achieve the desired instrumental field of view (1.3°) and introduces a loss to the throughput (and therefore the mapping speed), these losses can be mitigated by greatly increasing the pixel density on the focal plane. Overall, the study further justified the inclusion of a fourth lens for the optical design.

At present, the optical components are in queue for fabrication. Lenses and AR coatings will be manufactured by the University of Chicago,[35] and the infrared metal-mesh filters will be provided by Cardiff University.[47]

7.1.2 Detector Design

Inductors in LEKIDs are essentially a series of lines tracing back and forth, with kinetic inductance being proportional to the number of squares. A typical inductor consists of dark inductance around the arcs and optically active inductance under the feedhorn. The direction of the lines of the optically active inductor determine the polarization sensitivity of the detectors. Both kinetic and geometric inductance contribute to the total inductance of an MKID; an ideal detector should maximize kinetic inductance and minimize geometric inductance. In the case of a large inductance, such as for the multi-octave design presented in this dissertation, the capacitors are unable to be modified sufficiently to tune the resonant frequency across multiple octaves. This led to the development of a technique to modifiy the inductor such that a two octave design is achievable with minimal impact to the optical coupling and responsivity.

The technique of shorting inductor lines involves coupling adjacent lines into bundles. Lines which are shorted together provide the same optical coupling, but results in a decreased kinetic inductance as the effective number of squares has decreased. When N lines are shorted together, the result is a decrease in the kinetic inductance proportional to $1/N^2$, meaning this technique could be extended into more than two lines shorted together with careful planning. Since the geometric inductance of the detector is not impacted by shorting detectors, it is crucial for geometric inductance to be minimized as much as possible, else the effect of shorting inductor lines will be diminished by the increased inductance, risking deviations from the frequency schedule. This same effect using strictly capacitors would require a factor of 16 change in the capacitance and so far appears to be quite impossible based on our simulations, especially in light of parasitic capacitance.

The designs are based around two different inductor designs which are identical except for two lines being shorted together. Target values for the inductance are 200 nH and 50 nH, which assumes that the kinetic inductance dominates all other sources of inductance. Two different sets of interdigitated capacitors (IDCs) were designed which would allow for tuning across the entire planned readout band (two octaves), which have 5 μm and 12 μm widths. Using the two values for the

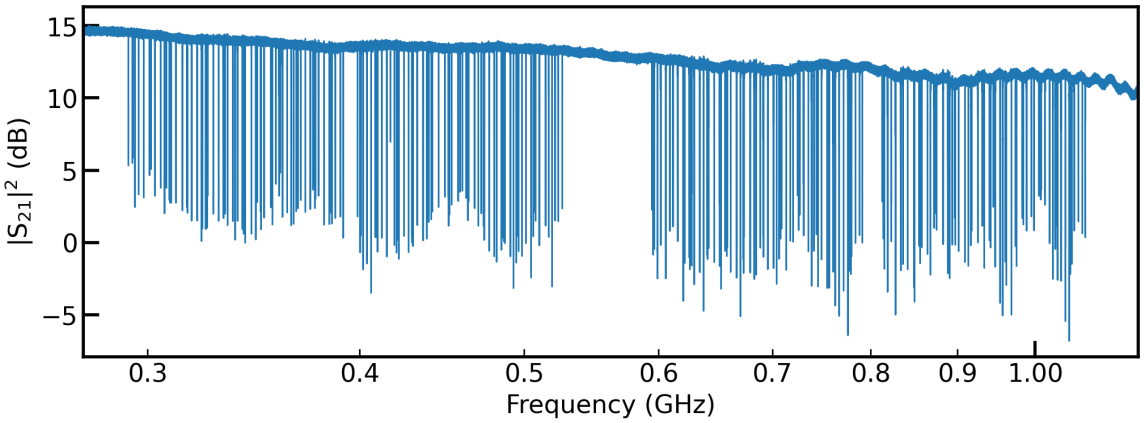

Figure 7.1: VNA sweep of a two octave array using the shorted inductor technique. These results confirm the efficacy of the multi-octave MKID design.

inductance and two sets of capacitors, the two octaves worth of resonators are easily obtained. Essentially, the line shorting provides a coarse tuning of the resonance, and the capacitors are relegated to fine tuning the resonators within the given band. The variations in the design are so simple, the sets of detectors are practically indistinguishable aside from a handful of lines shifted in the design software.

7.1.2.1 First Results

High yields were achieved in both the tested two octave arrays, which highlights the success of fabrication. Values for Q_i were greater than 100,000 in nearly all cases. Since Q_i depends greatly on the material properties of the film, this emphasizes the successful implementation of the pentalayer design. The measured properties matched with remarkable precision to the predictions provided by NIST, which were used in modelling and designing the arrays. These results imply that, should the need arise to increase the volume of the detectors to combat higher loading arise, a thicker film comprised of more layers could be accurately modelled and fabricated for future detectors.

7.1.3 Shorting Inductor Lines

Preliminary tests of detectors fabricated using shorted and non-shorted inductors confirmed the efficacy of this technique, as shown again in Figure 7.1. There is a significant band between the readout and parasitic resonances - nearly another octave. If the intervening band between the readout resonances and the parasitic resonances remain clear, it raises the potential for a design greater

than two octaves. However, as the complexity of the final arrays increase, it is expected that these resonances will shift to lower frequencies due to microstrip modes and the overall architecture of the array.

Thermal tests of the witness chips confirmed the results of the DC measurements used to characterize the film. The measured resonators exhibited high Q_i values, matched well with expected parameters based on simulations, and showed high stability at the expected bath temperature. The observed optical responsivity presented showed a sufficient and measurable shift in frequency in the expected loading regime. The detectors easily achieved the critical threshold of having optical responsivity at the relevant loading, far greater than the thermal responsivity at the expected bath temperature.

Analysis of the noise revealed that the desired sensitivity of at least 10^{-15} W/Hz$^{0.5}$ is achieved at the predicted loading. Furthermore, the NEP is photon noise dominated. However, the initial measurements revealed that the TLS noise is greater than expected. This is generally resolved through optimizing the interdigitated capacitors (IDCs) in the resonators, as this is where the electric field is able to interact the strongest with the TLS defects of the substrate. Narrowing the gaps, g, between fingers of width w increases the capacitance at the expense of increased TLS noise; larger gaps increase the overall size of the detector footprint. Literature suggests optimization to remove TLS noise should be straight forward.

The performance of the prototype detectors was remarkable, with one of the designs very nearly achieving all the specifications. The high volume resonator, with relatively minimal modifications, is being adopted as the final design for the 850 GHz detector array.

7.1.4 Survey of Bright Submillimeter Galaxies

This dissertation presented results of a blind millimeter-wave redshift survey of the brightest unlensed submillimeter galaxies (SMGs) from the SCUBA-2 Cosmological Legacy Survey (CLS), covering 12 of the brightest SMGs ($S_{850\mu m} > 11$ mJy) observed from the Lockman Hole, AEGIS, and CDF-N fields. Each of the SMGs have been identified as single sources by the Submillimeter Array (SMA). IRAM-NOEMA observations searched for the ^{12}CO and [CI] lines in these 12 SMGs, and SPIRE observations provided the results for photometric analysis in the 850 GHz band. Two CO lines were detected for five of the twelve targets, allowing for unambiguous redshifts. For

the remaining sources with only one CO line detection, a technique relying on photometric results allowed the CO line to be reliably attributed to one of 3 possibilities. The derived spectroscopic redshifts are in the range $2.08 < z < 4.05$ with a median value of $z = 2.9 \pm 0.6$

From the observations it was seen that many emission lines have broad widths between 500 and 1100 km/s, with a mean value for the CO FWHM of 700±300 km/s and a median of 800 km/s. Since the sources have high star formation rates, such a stable molecular gas distribution would imply a high gas excitation. However, observed line ratios in this survey are low compared to well-studied starburst galaxies. Furthermore, roughly 60% of the sources display double-peaked profiles indicative of merger systems and/or rotating disks. With the information available from this survey, the dynamics indicate that several of the systems potentially contain circumnuclear molecular toroids and/or are comprised of mergers.

Examination and comparison of the gradient of the redshift distribution with respect to S_{850} led to a combined measurement of 0.11 ± 0.04, which is in rough agreement with prior work.[22,112] However, each field showed varying degrees of deviation from this overall gradient, an indicator of overall randomness to this constraint within a given field. This finding was confirmed against simulations. One implication is that the variations seen in the redshift represent some form of structure in the Universe, with the homogeneity of the Universe dominating at larger fields and with a greater number of sources. Another explanation could be that the sources chosen for this survey represent extremes, with potentially 60% representing mergers and, as such, are not truly representative of the typical SMG found in other surveys; the relative rarity of HyLIRGs means the data could potentially be skewed by a few bright mergers. Consideration needs to be made moving forward in defining the exact nature of these sources - be they merger systems and/or rotating disks, the field dependent nature of the gradient and the potential impact of cosmological structure, and the variations in the gradient seen for highly luminous sources.

7.2 Future Directions

The first attempt at the two-octave detector design confirms first, that the shorting technique works, and second, that there is potential for a two-and-a-half or even three-octave design given the range between the readout and parasitic resonances. This could easily be performed by coupling up to three inductor lines together. Given the current configuration, one could imagine an MKID with

12 lines, 6 lines, and 4 lines with an inductance of 200 nH, 50 nH, and 22.2 nH. Resonances for these detectors could then be fine-tuned within the readout band using identical capacitors. As the capabilities for multiplexing MKIDs extends beyond two-octaves (see Refs. 19, 20), the demand for such detectors increases, especially considering applications where hardware demands are limited (i.e. space-based observatories).

Other areas of active study are methods to increase the sensitivity of MKIDs. This could be done through clever fabrication techniques to remove TLS noise as a common mode source,[164] or through novel geometries and materials for MKIDS.[109] As the field of MKID design is as of yet relatively young, there are a host of variables that await exploration, and several upcoming projects where these designs could be utilized. The application of the novel multi-octave MKID design presented in this work being such an example as it is applied to the 850 GHz module of Prime-Cam.

A potential candidate for the application of research and development in MKID arrays is the proposed 660 GHz module for Prime-Cam. This module will benefit from the existing developments into the optical and mechanical design for the 850 GHz module, but allows for further research into exploring lower noise designs for high-frequency detectors under high loading with multi-octave multiplexing. For example, one might explore different film depositions of TiN,[165] or even other material candidates such as aluminum-doped manganese (AlMn).[166,167] Another direction could be the development of better models to simulate parasitic resonances and nonlinearities[73] in MKID arrays for expanding the multi-octave design - allowing for expansion of the readout band and potentially removing or reducing parasitic capacitance and minimizing the impact of nonlinearities. One could also delve into multichroic receivers and on-chip spectrometers.[168] Overall, the parameter space of MKIDs is wide open with many diverse opportunities for exploration and application.

7.3 Conclusion

This dissertation presents the recent and ongoing work dedicated toward the development of the 850 GHz module of Prime-Cam for the CCAT collaboration. The optical design is mature and has undergone a design review and has been finalized, along with the mechanical design. There is a clear path forward to predict the systematic uncertainties of the system as the module is assembled, tested and deployed. This will be work done in tandem with ongoing efforts to provide astronomical forecasts for how data obtained from the deployment from Prime-Cam will be analyzed. Also

presented in this work is the development and successful application of a two-octave MKID design.

Much of the technology developed throughout this work will benefit future missions, such as the proposed Origins Space Telescope,[169] or the recently announced Simons Observatory to be built in the UK which will incorporate MKIDs rather than the transition-edge sensors used in the other SO observatories.[170] Continuation of this work will provide the requisite maturation of technology necessary for future infrared missions, and ensure Canadian involvement in collaborations for the future development of astronomical instrumentation for both terrestrial and spaceborne observatories. With the instrumentation and test kit accumulated for this body of work, there is sufficient room for exploration of future novel technological advances and instrumentation.

Bibliography

[1] Lutz, D. Far-infrared surveys of galaxy evolution. *Annual Review of Astronomy and Astrophysics*, 52(1):373 – 414, 2014.

[2] E. Hubble. A relation between distance and radial velocity among extragalactic nebulae. In *Proceedings of the National Academy of Sciences of the United States of America*, volume 15, pages 168 – 173, Mar. 1929.

[3] Turon, C. ESA Space Science Programme, Cosmic Vision 2015-2025, for astrophysics. *Proceedings of the International Astronomical Union*, 2(14):530–531, 2006.

[4] Kouveliotou, C. et al. Enduring Quests-Daring Visions (NASA Astrophysics in the Next Three Decades), 2014.

[5] Farrah, D. et al. Review: far-infrared instrumentation and technological development for the next decade. *Journal of Astronomical Telescopes, Instruments, and Systems*, 5(2):1 – 34, 2019.

[6] NASA: Cool Cosmos. IR Atmospheric Windows. `http://coolcosmos.ipac.caltech.edu/cosmic$_$classroom/ir$_$tutorial/irwindows.html`.

[7] Dyson, J. E. and Williams, D. A. *The Physics of the Interstellar Medium*. 1997.

[8] M. Planck. *Über eine Verbesserung der Wienschen Spektralgleichung*, pages 175–178. Vieweg+Teubner Verlag, Wiesbaden, 1978.

[9] Prime Collaboration. CCAT-prime Collaboration: Science Goals and Forecasts with Prime-Cam on the Fred Young Submillimeter Telescope, 2022.

[10] Stacey, G. et al. CCAT-Prime: science with an ultra-widefield submillimeter observatory on Cerro Chajnantor. In Heather K. Marshall and Jason Spyromilio, editors, *Ground-based and Airborne Telescopes VII*, volume 10700, pages 482 – 501. International Society for Optics and Photonics, SPIE, 2018.

[11] Niemack, M. Designs for a large-aperture telescope to map the cmb 10x faster. *Appl. Opt.*, 55(7):1688 – 1696, Mar. 2016.

[12] Chapman, S. C. et al. CCAT-prime: the 850 GHz camera for prime-cam on FYST, 2022.

[13] Parshley, S. et al. The optical design of the six-meter CCAT-prime and Simons Observatory telescopes. In Heather K. Marshall and Jason Spyromilio, editors, *Ground-based and Airborne Telescopes VII*, volume 10700, pages 1292 – 1304. International Society for Optics and Photonics, SPIE, 2018.

[14] Vavagiakis, E. M. et al. Prime-Cam: a first-light instrument for the CCAT-prime telescope. In Jonas Zmuidzinas and Jian-Rong Gao, editors, *Millimeter, Submillimeter, and Far-Infrared*

Detectors and Instrumentation for Astronomy IX, volume 10708, pages 187 – 202. International Society for Optics and Photonics, SPIE, 2018.

[15] Chapman, S. C. et al. A 350 micron camera module for the Prime-Cam instrument on CCAT-prime. In Jonas Zmuidzinas and Jian-Rong Gao, editors, *Millimeter, Submillimeter, and Far-Infrared Detectors and Instrumentation for Astronomy X*, volume 11453, page 1145305. International Society for Optics and Photonics, SPIE, 2020.

[16] Elbaz, D. et al. Starbursts in and out of the star-formation main sequence. *A&A*, 616:A110, 2018.

[17] Day, P. K. et al. A broadband superconducting detector suitable for use in large arrays. *Nature*, 425(6960):817 – 821, Oct. 2003.

[18] Sinclair, A. K. et al. CCAT-prime: RFSoC based readout for frequency multiplexed kinetic inductance detectors. In Jonas Zmuidzinas and Jian-Rong Gao, editors, *Millimeter, Submillimeter, and Far-Infrared Detectors and Instrumentation for Astronomy XI*, volume 12190, page 121900W. International Society for Optics and Photonics, SPIE, 2022.

[19] Sinclair, A. K. et al. CCAT: detector noise limited performance of the RFSoC-based readout electronics for mm/sub-mm/far-IR KIDs. In Jonas Zmuidzinas and Jian-Rong Gao, editors, *Millimeter, Submillimeter, and Far-Infrared Detectors and Instrumentation for Astronomy XII*, volume 13102, page 131022E. International Society for Optics and Photonics, SPIE, 2024.

[20] Xie, M. et al. CCAT: multirate DSP for sub-mm astronomy: polyphase synthesis filter bank on FPGA for enhanced MKID readout. In Jonas Zmuidzinas and Jian-Rong Gao, editors, *Millimeter, Submillimeter, and Far-Infrared Detectors and Instrumentation for Astronomy XII*, volume 13102, page 1310213. International Society for Optics and Photonics, SPIE, 2024.

[21] Burgoyne, J. R. et al. CCAT: FYST prime-cam readout software: a framework for massively scalable KID arrays. In Jorge Ibsen and Gianluca Chiozzi, editors, *Software and Cyberinfrastructure for Astronomy VIII*, volume 13101, page 131013C. International Society for Optics and Photonics, SPIE, 2024.

[22] Birkin, J. E. et al. An ALMA/NOEMA survey of the molecular gas properties of high-redshift star-forming galaxies. *Monthly Notices of the Royal Astronomical Society*, 501(3):3926–3950, Dec. 2020.

[23] Hill, R. et al. The SCUBA-2 web survey: I. Observations of CO(3–2) in hyper-luminous QSO fields. *Monthly Notices of the Royal Astronomical Society*, 485(1):753–769, Feb. 2019.

[24] Parshley, S. et al. CCAT-prime: a novel telescope for sub-millimeter astronomy. In Heather K. Marshall and Jason Spyromilio, editors, *Ground-based and Airborne Telescopes VII*, volume 10700, pages 1744 – 1758. International Society for Optics and Photonics, SPIE, 2018.

[25] Huber, A. I. et al. CCAT-prime: optical and cryogenic design of the 850 GHz module for Prime-Cam. In Jonas Zmuidzinas and Jian-Rong Gao, editors, *Millimeter, Submillimeter, and Far-Infrared Detectors and Instrumentation for Astronomy XI*, volume 12190, page 121901D. International Society for Optics and Photonics, SPIE, 2022.

[26] Nikola, T. et al. CCAT-prime: the epoch reionization spectrometer for primce-cam on FYST. In Jonas Zmuidzinas and Jian-Rong Gao, editors, *Millimeter, Submillimeter, and Far-Infrared Detectors and Instrumentation for Astronomy XI*, volume 12190, page 121900G. International Society for Optics and Photonics, SPIE, 2022.

[27] Choi, S. K. et al. Sensitivity of the prime-cam instrument on the ccat-prime telescope. *Journal of Low Temperature Physics*, 199:1089 – 1097, 2020.

[28] Hubmayr, J. et al. Millimeter-wave kinetic inductance detectors with no 1/f noise. In Jonas Zmuidzinas and Jian-Rong Gao, editors, *Millimeter, Submillimeter, and Far-Infrared Detectors and Instrumentation for Astronomy X*, volume 11453, page 114531D. International Society for Optics and Photonics, SPIE, 2020.

[29] Golec, J. E. et al. Design and fabrication of metamaterial anti-reflection coatings for the Simons Observatory. In Ramón Navarro and Roland Geyl, editors, *Advances in Optical and Mechanical Technologies for Telescopes and Instrumentation IV*, volume 11451, pages 1115 – 1122. International Society for Optics and Photonics, SPIE, 2020.

[30] Goldsmith, P. F. *Quasioptical systems : Gaussian beam quasioptical propagation and applications*. Wiley, 1 edition, 1998.

[31] Griffin, M. J., Bock, J. J., and Gear, W. K. Relative performance of filled and feedhorn-coupled focal-plane architectures. *Appl. Opt.*, 41(31):6543–6554, Nov. 2002.

[32] Dicker, S. R. et al. Cold optical design for the large aperture Simons' Observatory telescope. In Heather K. Marshall and Jason Spyromilio, editors, *Ground-based and Airborne Telescopes VII*, volume 10700, pages 1064 – 1076. International Society for Optics and Photonics, SPIE, 2018.

[33] Gallardo, P. A. et al. Systematic uncertainties in the Simons Observatory: optical effects and sensitivity considerations. In Jonas Zmuidzinas and Jian-Rong Gao, editors, *Millimeter, Submillimeter, and Far-Infrared Detectors and Instrumentation for Astronomy IX*, volume 10708, pages 658 – 673. International Society for Optics and Photonics, SPIE, 2018.

[34] Gudmundsson, J. E. et al. The Simons Observatory: modeling optical systematics in the Large Aperture Telescope. *Appl. Opt.*, 60(4):823–837, Feb. 2021.

[35] Golec, J. E. et al. Simons Observatory: broadband metamaterial antireflection cuttings forlarge-aperture alumina optics. *Appl. Opt.*, 61(30):8904–8911, Oct. 2022.

[36] Bluefors. LD Dilution Refrigerators, 2022. www.bluefors.com/.

[37] Born, M. and Wolf, E. *Principles of Optics: Electromagnetic Theory of Propagation, Interference and Diffraction of Light*. Cambridge University Press, 7th edition, 1999.

[38] van den Bos, A. Aberration and the strehl ratio. *J. Opt. Soc. Am. A*, 17(2):356–358, Feb. 2000.

[39] Zemax. OpticStudio, 2022. www.zemax.com/.

[40] Bentley, J. L. and Olson, C. *Field Guide to Lens Design*. Field Guides. SPIE, 2012.

[41] Seidel, L. Zur dioptrik. ueber die entwicklung der glieder 3ter ordnung, welche den weg eines ausserhalb der ebene der axe gelegenen lichtstrahles durch ein system brechender medien bestimmen, von herrn dr. l. seidel. *Astronomische Nachrichten*, 43(19):289–304, 1856.

[42] Mahajan, V. N. *Aberration Theory Made Simple*. SPIE tutorial texts. SPIE Optical Engineering Press, 1991.

[43] Peatross, J. and Ware, M. *Physics of Light and Optics*. available at optics.byu.edu, 2015.

[44] Sasián, J. *Introduction to Aberrations in Optical Imaging Systems*. Cambridge University Press, 2013.

[45] Wheeler, J. et al. Broadband kinetic inductance detectors for far-IR observations. In Jonas Zmuidzinas and Jian-Rong Gao, editors, *Millimeter, Submillimeter, and Far-Infrared Detectors and Instrumentation for Astronomy XI*, volume 12190, page 1219006. International Society for Optics and Photonics, SPIE, 2022.

[46] CryoElec LLC. Cryogenic Low Noise Amplifiers, 2022. https://www.cryoelec.com/.

[47] Ade, P. A. R. et al. A review of metal mesh filters. In Jonas Zmuidzinas, Wayne S. Holland, Stafford Withington, and William D. Duncan, editors, *Millimeter and Submillimeter Detectors and Instrumentation for Astronomy III*, volume 6275, page 62750U. International Society for Optics and Photonics, SPIE, 2006.

[48] Crowley, K. T. et al. Studies of systematic uncertainties for Simons Observatory: detector array effects. In Jonas Zmuidzinas and Jian-Rong Gao, editors, *Millimeter, Submillimeter, and Far-Infrared Detectors and Instrumentation for Astronomy IX*, volume 10708, page 107083Z. International Society for Optics and Photonics, SPIE, 2018.

[49] Bryan, S. A. et al. Development of calibration strategies for the Simons Observatory. In Jonas Zmuidzinas and Jian-Rong Gao, editors, *Millimeter, Submillimeter, and Far-Infrared Detectors and Instrumentation for Astronomy IX*, volume 10708, page 1070840. International Society for Optics and Photonics, SPIE, 2018.

[50] Huber, A. I. Exploring the challenges of a far-infrared post-dispersed polarising fourier transform spectrometer. Master's thesis, University of Lethbridge, 2021.

[51] Sinclair, A. K. *In-Flight Performance of the BLAST-TNG Balloon-Borne Far-Infrared Telescope and Development of a Reconfigurable Readout on the RFSoC Platform for Frequency Multiplexed Superconducting Detector Arrays*. PhD thesis, Arizona State University, 2021.

[52] Vavagiakis, E. M. et al. CCAT-prime: design of the Mod-Cam receiver and 280 GHz MKID instrument module. In Jonas Zmuidzinas and Jian-Rong Gao, editors, *Millimeter, Submillimeter, and Far-Infrared Detectors and Instrumentation for Astronomy XI*, volume 12190, page 1219004. International Society for Optics and Photonics, SPIE, 2022.

[53] Simon, S. M. *Cosmic Microwave Background Polarimetry with ABS and ACT: Instrumental Design, Characterization, and Analysis*. PhD thesis, Princeton U. (main), Sep. 2016.

[54] Koopman, B. et al. Optical modeling and polarization calibration for CMB measurements with ACTPol and Advanced ACTPol. In Wayne S. Holland and Jonas Zmuidzinas, editors, *Millimeter, Submillimeter, and Far-Infrared Detectors and Instrumentation for Astronomy VIII*, volume 9914, page 99142T. International Society for Optics and Photonics, SPIE, 2016.

[55] Noroozian, O. et al. Crosstalk reduction for superconducting microwave resonator arrays. *IEEE Transactions on Microwave Theory and Techniques*, 60(5):1235 – 1243, 2012.

[56] Wang, Y. et al. Simons Observatory Focal-Plane Module: In-lab Testing and Characterization Program. *Journal of Low Temperature Physics*, 209(5):944–952, Dec. 2022.

[57] Ulbricht, G., De Lucia, M. and Baldwin, E. Applications for microwave kinetic induction detectors in advanced instrumentation. *Applied Sciences*, 11(6), 2021.

[58] Schlaerth, J. et al. Applications for microwave kinetic induction detectors in advanced instrumentation. *Applied Sciences*, 151:684–689, 2008.

[59] Maloney, P. R. et al. MUSIC for sub/millimeter astrophysics. In Wayne S. Holland and Jonas Zmuidzinas, editors, *Millimeter, Submillimeter, and Far-Infrared Detectors and Instrumentation for Astronomy V*, volume 7741, page 77410F. International Society for Optics and Photonics, SPIE, 2010.

[60] Zmuidzinas, J. Superconducting Microresonators: Physics and Applications. *Annual Review of Condensed Matter Physics*, 3(1):169–214, 2012.

[61] Tinkham, M. *Introduction to Superconductivity*. Dover Publications, 2004.

[62] Jhabvala, C. A. et al. Atomic layer deposition josephson junctions for cryogenic circuit applications. *Journal of Low Temperature Physics*, 200:331–335, Sep. 2020.

[63] Marder, M. P. *Condensed Matter Physics*. Wiley, 2 edition, 2010.

[64] Ashcroft, N. W. and Mermin, N. D. *Solid State Physics*. Harcourt College Publishers, 1976.

[65] McCarrick, H. *Design and performance of kinetic inductance detectors for cosmic microwave background polarimetry*. PhD thesis, Columbia University, 2018.

[66] Noroozian, O. *Superconducting Microwave Resonator Arrays for Submillimeter/Far-Infrared Imaging*. PhD thesis, California Institute of Technology, 2018.

[67] Mauskopf, P. D. Transition edge sensors and kinetic inductance detectors in astronomical instruments. *Publications of the Astronomical Society of the Pacific*, 130(990):082001, Jun. 2018.

[68] Mattis, D. C. and Bardeen, J. Theory of the anomalous skin effect in normal and superconducting metals. *Phys. Rev.*, 111:412–417, Jul. 1958.

[69] Gao, J. *The Physics of Superconducting Microwave Resonators*. PhD thesis, California Institute of Technology, 2008.

[70] Doyle, S. et al. Lumped Element Kinetic Inductance Detectors. *Journal of Applied Physics*, 151:530–536, Apr. 2008.

[71] Mazin, B. A. et al. Multiplexable kinetic inductance detectors. *AIP Conference Proceedings*, 605(1):309–312, Feb. 2002.

[72] Göppl, M. et al. Coplanar waveguide resonators for circuit quantum electrodynamics. *Journal of Applied Physics*, 104(11):113904, Dec. 2008.

[73] Swenson, L. J. et al. Operation of a titanium nitride superconducting microresonator detector in the nonlinear regime. *Journal of Applied Physics*, 113(10):104501–104501–9, Mar. 2013.

[74] Gordon, S. *Highly multiplexed superconducting detectors and readout electronics for balloon-borne and ground-based far-infrared imaging and polarimetry*. PhD thesis, Arizona State University, 2019.

[75] Noroozian, O. et al. Two-level system noise reduction for Microwave Kinetic Inductance Detectors. *AIP Conference Proceedings*, 1185(1):148–151, Dec. 2009.

[76] de Visser, P. J. et al. Number fluctuations of sparse quasiparticles in a superconductor. *Phys. Rev. Lett.*, 106:167004, Apr. 2011.

[77] Flanigan, D. et al. Photon noise from chaotic and coherent millimeter-wave sources measured with horn-coupled, aluminum lumped-element kinetic inductance detectors. *Applied Physics Letters*, 108(8):083504, Feb. 2016.

[78] Barry, P. *On the development of SuperSpec; a Fully Integrated On-chip Spectrometer for Far-infrared Astronomy*. PhD thesis, Cardiff University, 2014.

[79] Hubmayr, J. et al,. Photon-noise limited sensitivity in titanium nitride kinetic inductance detectors. *Applied Physics Letters*, 106(7):073505, Feb. 2015.

[80] Gao, J. et al. Experimental evidence for a surface distribution of two-level systems in superconducting lithographed microwave resonators. *Applied Physics Letters*, 92(15):152505, Apr. 2008.

[81] Barends, R. et al. Reduced frequency noise in superconducting resonators. *Applied Physics Letters*, 97(3):033507, Jul. 2010.

[82] Gao, J. et al. A semiempirical model for two-level system noise in superconducting microresonators. *Applied Physics Letters*, 92(21):212504, May 2008.

[83] Sonnet Software. Sonnet, 2024. www.sonnetsoftware.com/.

[84] Caspers, F. RF engineering basic concepts: S-parameters. In *CERN Yellow Report CERN-2011-007*, pages 67–93. CERN, 2011.

[85] Pozar, D. M. *Microwave engineering; 4th ed.* Wiley, Hoboken, NJ, 2012.

[86] Dassault Systemes. CST Studio Suite, 2023. www.3ds.com/.

[87] COAX CO., LTD. Semi-rigid coaxial cables, 2022. www.coax.co.jp/en/semi.

[88] Neric, M. et al. Design and prototyping of new flexible stripline based transmission lines as alternatives to semi-rigid coaxial cables. In *30th International Symposium on Space Terahertz Technology*, pages 69–71, 2019.

[89] Arsenovic, A. et al. scikit-rf: An open source python package for microwave network creation, analysis, and calibration [speaker's corner]. *IEEE Microwave Magazine*, 23(1):98–105, 2022.

[90] Thomas, C. N., Withington, S., and Goldie, D. J. Electrothermal model of kinetic inductance detectors. *Superconductor Science and Technology*, 28(4):045012, Feb. 2015.

[91] Jiang, F., Claude, S., and Garcia, D. Hybrid cryogenic low noise amplifier for the meetkat array. In *2014 16th International Symposium on Antenna Technology and Applied Electromagnetics (ANTEM)*, pages 1–2, 2014.

[92] Mini-Circuits. ZKL-1R5+ Datasheet, 2022. https://www.minicircuits.com/pdfs/ZKL-1R5+.pdf.

[93] Stanley, M. et al. Characterizing Scattering Parameters of Superconducting Quantum Integrated Circuits at Milli-Kelvin Temperatures. *IEEE Access*, 10:43376–43386, 2022.

[94] Sipola, H. et al. Multiplexed readout of kinetic inductance bolometer arrays. *Review of Scientific Instruments*, 90(7):074702, Jul. 2019.

[95] AMD Xilinx. Zynq UltraScale+ RFSoC Data Sheet: DC and AC Switching Characteristics DS926 (v1.10). `docs.xilinx.com/`, 2021. (Accessed: 28 Jun 2022).

[96] Advanced Micro Devices, Inc. RF Sampling, 2022. www.xilinx.com/.

[97] van Rantwijk, J. et al. Multiplexed readout for 1000-pixel arrays of microwave kinetic inductance detectors. *IEEE Transactions on Microwave Theory and Techniques*, 64(6):1876–1883, 2016.

[98] McHugh, S. et al. A readout for large arrays of microwave kinetic inductance detectors. *Review of Scientific Instruments*, 83(4):044702, Apr. 2012.

[99] Paiella, A. et al. Kinetic inductance detectors and readout electronics for the olimpo experiment. *Journal of Physics: Conference Series*, 1182(1):012005, Feb. 2019.

[100] Bisigello, L. et al. Calibration scheme for large kinetic inductance detector arrays based on readout frequency response. *Journal of Low Temperature Physics*, 184(1):161–166, Jul. 2016.

[101] Huber, A. I. et al. CCAT: design and performance of densely packed, high-frequency, dual-polarization kinetic inductance detectors for the Prime-Cam 850 GHz module. In Jonas Zmuidzinas and Jian-Rong Gao, editors, *Millimeter, Submillimeter, and Far-Infrared Detectors and Instrumentation for Astronomy XII*, volume 13102, page 1310203. International Society for Optics and Photonics, SPIE, 2024.

[102] Duell, C. J. et al. CCAT: nonlinear effects in 280 GHz aluminum kinetic inductance detectors. In Jonas Zmuidzinas and Jian-Rong Gao, editors, *Millimeter, Submillimeter, and Far-Infrared Detectors and Instrumentation for Astronomy XII*, volume 13102, page 131021O. International Society for Optics and Photonics, SPIE, 2024.

[103] Doyle, S. et al. Optimisation of Lumped Element Kinetic Inductance Detectors for use in ground based mm and sub-mm arrays. *AIP Conference Proceedings*, 1185(1):156–159, Dec. 2009.

[104] Austermann, J. E. et al. Millimeter-wave polarimeters using kinetic inductance detectors for toltec and beyond. *Journal of Low Temperature Physics*, 193:120 – 127, 2018.

[105] Vissers, M. R. et al. Improving the yield of CCAT MKID arrays with post-measurement lithographic corrections. In Jonas Zmuidzinas and Jian-Rong Gao, editors, *Millimeter, Submillimeter, and Far-Infrared Detectors and Instrumentation for Astronomy XII*, volume PC13102, page PC131020Z. International Society for Optics and Photonics, SPIE, 2024.

[106] Steinbach, B. A. et al. Thermal kinetic inductance detectors for ground-based millimeter-wave cosmology. *Journal of Low Temperature Physics*, 193(3):88–95, Nov. 2018.

[107] Wiener, N. Generalized harmonic analysis. *Acta Mathematica*, 55(none):117 – 258, 1930.

[108] A. Khintchine. Korrelationstheorie der stationären stochastischen prozesse. *Mathematische Annalen*, 109(1):604–615, Dec. 1934.

[109] Pan, Z. et al. Noise optimization for mkids with different design geometries and material selections. *IEEE Transactions on Applied Superconductivity*, 33(5):1–8, 2023.

[110] de Visser, P. J. et al. The non-equilibrium response of a superconductor to pair-breaking radiation measured over a broad frequency band. *Applied Physics Letters*, 106(25):252602, Jun. 2015.

[111] Baselmans, J. J. A. et al. Ultra-sensitive thz microwave kinetic inductance detectors for future space telescopes. *A&A*, 665:A17, 2022.

[112] Stach, S. M. et al. An ALMA survey of the SCUBA-2 Cosmology Legacy Survey UKIDSS/UDS field: source catalogue and properties. *Monthly Notices of the Royal Astronomical Society*, 487(4):4648–4668, Jun. 2019.

[113] Simpson, J. M. et al. An ALMA survey of the brightest sub-millimetre sources in the SCUBA-2–COSMOS field. *Monthly Notices of the Royal Astronomical Society*, 495(3):3409–3430, May 2020.

[114] Smail, I. et al. The nature of faint submillimetre-selected galaxies. *Monthly Notices of the Royal Astronomical Society*, 331(2):495–520, Mar. 2002.

[115] Borys, C. et al. The Hubble Deep Field North SCUBA Super-map—I. Submillimetre maps, sources and number counts. *Monthly Notices of the Royal Astronomical Society*, 344(2):385–398, Sep. 2003.

[116] Greve, T. R. et al. A 1200-μm MAMBO survey of ELAISN2 and the Lockman Hole – I. Maps, sources and number counts. *Monthly Notices of the Royal Astronomical Society*, 354(3):779–797, Nov. 2004.

[117] Coppin, K. et al. The SCUBA Half-Degree Extragalactic Survey – II. Submillimetre maps, catalogue and number counts. *Monthly Notices of the Royal Astronomical Society*, 372(4):1621–1652, Oct. 2006.

[118] Bertoldi, F. et al. COSBO: The MAMBO 1.2 millimeter imaging survey of the COSMOS field*. *The Astrophysical Journal Supplement Series*, 172(1):132, Sep. 2007.

[119] Scott, K. S. et al. AzTEC millimetre survey of the COSMOS field – I. Data reduction and source catalogue. *Monthly Notices of the Royal Astronomical Society*, 385(4):2225–2238, Mar. 2008.

[120] Weiß, A. et al. First redshift determination of an optically/ultraviolet faint submillimeter galaxy using co emission lines. *The Astrophysical Journal*, 705(1):L45, Oct. 2009.

[121] Oliver, S. J. et al. Hermes: Spire galaxy number counts at 250, 350, and 500 μm*. *A&A*, 518:L21, Jul. 2010.

[122] Mocanu, L. M. et al. Extragalactic millimeter-wave point-source catalog, number counts and statistics from 771 deg^2 of the SPT-SZ survey. *The Astrophysical Journal*, 779(1):61, Nov. 2013.

[123] Planck Collaboration et al. Planck 2013 results. XXVIII. The Planck Catalogue of Compact Sources. *A&A*, 571:A28, 2014.

[124] Fu, H. et al. Planck 2013 results. XXVIII. The Planck Catalogue of Compact Sources. *Nature*, 498:338–341, 2013.

[125] Ivison R. J. et al. Herschel-atlas: A binary HyLIRG pinpointing a cluster of starbursting protoellipticals. *The Astrophysical Journal*, 772(2):137, Jul. 2013.

[126] Ivison, R. J. et al. A hyperluminous galaxy at z = 2.8 found in a deep submillimetre survey. *Monthly Notices of the Royal Astronomical Society*, 298(2):583–593, Aug. 1998.

[127] Ivison, R. J. et al. Gas, dust and stars in the SCUBA galaxy, SMM J02399-0136: the EVLA reveals a colossal galactic nursery. *Monthly Notices of the Royal Astronomical Society*, 404(1):198–205, Apr. 2010.

[128] Pope, A. et al. The Hubble Deep Field-North SCUBA Super-map – IV. Characterizing submillimetre galaxies using deep Spitzer imaging. *Monthly Notices of the Royal Astronomical Society*, 370(3):1185–1207, Jul. 2006.

[129] Younger, J. D. et al. The physical scale of the far-infrared emission in the most luminous submillimeter galaxies. *The Astrophysical Journal*, 688(1):59, Nov. 2008.

[130] Younger, J. D. et al. The physical scale of the far-infrared emission in the most luminous submillimetre galaxies - II. Evidence for merger-driven star formation. *Monthly Notices of the Royal Astronomical Society*, 407(2):1268–1276, Sep. 2010.

[131] Chapman, S. C. et al. A median redshift of 2.4 for galaxies bright at submillimetre wavelengths. *Nature*, 422(6933):695–698, Apr. 2003.

[132] Chapman, S. C. et al. A redshift survey of the submillimeter galaxy population. *The Astrophysical Journal*, 622(2):772, Apr. 2005.

[133] Wardlow, J. L. et al. The LABOCA survey of the Extended Chandra Deep Field-South: a photometric redshift survey of submillimetre galaxies. *Monthly Notices of the Royal Astronomical Society*, 415(2):1479–1508, Jul. 2011.

[134] Simpson, J. M. et al. An ALMA survey of submillimeter galaxies in the Extended Chandra Deep Field South: The redshift distribution and evolution of submillimeter galaxies. *The Astrophysical Journal*, 788(2):125, May 2014.

[135] Hodge, J. A. et al. An ALMA survey of submillimeter galaxies in the Extended Chandra Deep Field South: Source catalog and multiplicity. *The Astrophysical Journal*, 768(1):91, Apr. 2013.

[136] Danielson A. L. R. et al. An ALMA Survey of Submillimeter Galaxies in the Extended Chandra Deep Field South: Spectroscopic Redshifts. *The Astrophysical Journal*, 840(2):78, May 2017.

[137] Swinbank, A. M. et al. Intense star formation within resolved compact regions in a galaxy at z = 2.3. *Nature*, 464(7289):733–736, Apr. 2010.

[138] Harris, A. I. et al. Blind detections of CO J = 1–0 in 11 H-ATLAS galaxies at z = 2.1–3.5 with the GBT/Zpectrometer. *The Astrophysical Journal*, 752(2):152, Jun. 2012.

[139] Vieira, J. D. et al. Dusty starburst galaxies in the early universe as revealed by gravitational lensing. *Nature*, 495(7441):344–347, Mar. 2013.

[140] Zavala, J. A. et al. Early Science with the Large Millimeter Telescope: observations of dust continuum and CO emission lines of cluster-lensed submillimetre galaxies at z=2.0–4.7. *Monthly Notices of the Royal Astronomical Society*, 452(2):1140–1151, Jul. 2015.

[141] Strandet, M. L. et al. The redshift distribution of dusty star-forming galaxies from the SPT survey. *The Astrophysical Journal*, 822(2):80, May 2016.

[142] Bothwell, M. S. et al. A survey of molecular gas in luminous sub-millimetre galaxies. *Monthly Notices of the Royal Astronomical Society*, 429(4):3047–3067, Jan. 2013.

[143] Walter, F. et al. The intense starburst HDF 850.1 in a galaxy overdensity at z≈5.2 in the Hubble Deep Field. *Nature*, 486(7402):233–236, Jun. 2012.

[144] Hayward, C. C. et al. Observational constraints on the physical nature of submillimetre source multiplicity: chance projections are common. *Monthly Notices of the Royal Astronomical Society*, 476(2):2278–2287, Feb. 2018.

[145] IRAM Collaboration. NOEMA. `https://iram-institute.org/science-portal/noema/`, 2024.

[146] Smithsonian Astrophysical Observatory. The Submillimeter Array. `https://lweb.cfa.harvard.edu/sma/index.html`, 2024.

[147] Ho, P. T. P., Moran, J. M., and Lo, K. Y. The submillimeter array. *The Astrophysical Journal*, 616(1):L1, Oct. 2004.

[148] Battisti, A. J. et al. MAGPHYS+photo-z: Constraining the Physical Properties of Galaxies with Unknown Redshifts. *The Astrophysical Journal*, 882(1):61, Sep. 2019.

[149] Carilli, C. L. and Walter, F. Cool gas in high-redshift galaxies. *Annual Review of Astronomy and Astrophysics*, 51(Volume 51, 2013):105–161, 2013.

[150] P.M. "Solomon and P.A." Vanden Bout. Molecular gas at high redshift. *Annual Review of Astronomy and Astrophysics*, 43:677–725, 2005.

[151] Burgoyne, J. R. Unveiling the evolution of a galaxy hosting a hyper-luminous quasar at redshift 2. Master's thesis, University of British Columbia, 2021.

[152] Scoville, N. Z. et al. Dust and gas in the core of Arp 220 (IC 4553). *Astrophysical Journal*, pages L5–L9, 1991.

[153] Downes, D. and Solomon, P. M. Rotating nuclear rings and extreme starbursts in ultraluminous galaxies. *The Astrophysical Journal*, 507(2):615, Nov. 1998.

[154] Dudzevičiūtė, U. et al. Tracing the evolution of dust-obscured activity using sub-millimetre galaxy populations from STUDIES and AS2UDS. *Monthly Notices of the Royal Astronomical Society*, 500(1):942–961, Oct. 2020.

[155] Nakajima, T. et al. A molecular line survey toward the nearby galaxies NGC 1068, NGC 253, and IC 342 at 3 mm with the Nobeyama 45 m radio telescope: Impact of an AGN on 1 kpc scale molecular abundances. *Publications of the Astronomical Society of Japan*, 70(1):7, Feb. 2018.

[156] Genzel, R. et al. Spatially resolved millimeter interferometry of smm j02399–0136: A very massive galaxy at z = 2.8*. *The Astrophysical Journal*, 584(2):633, Feb. 2003.

[157] Archibald, E. N. et al. A submillimetre survey of the star formation history of radio galaxies. *Monthly Notices of the Royal Astronomical Society*, 323(2):417–444, May 2001.

[158] Dannerbauer, H. et al. Properties of millimeter galaxies: Constraints from k-band blank fields*. *The Astrophysical Journal*, 573(2):473, Jul. 2002.

[159] Younger, J. D. et al. Evidence for a population of high-redshift submillimeter galaxies from interferometric imaging. *The Astrophysical Journal*, 671(2):1531, Dec. 2007.

[160] Cowie, L. L. et al. New Insight on Galaxy Formation and Evolution From Keck Spectroscopy of the Hawaii Deep Fields. *AJ*, 112:839, Sep. 1996.

[161] Béthermin, M. et al. pySIDES: Simulated Infrared Dusty Extragalactic Sky in Python. Astrophysics Source Code Library, record ascl:2204.016, Apr. 2022.

[162] Béthermin, M. et al. The influence of wavelength, flux, and lensing selection effects on the redshift distribution of dusty, star-forming galaxies. *A&A*, 576:L9, Apr. 2015.

[163] Austermann, J. et al. Millimeter-wave polarimeters using kinetic inductance detectors for toltec and beyond. *Journal of Low Temperature Physics*, 193(3-4):120 – 127, Nov. 2018.

[164] Foroozani, N. et al. Dual-resonator kinetic inductance detector for distinction between signal and $1/f$ frequency noise. *Phys. Rev. Appl.*, 21:014009, Jan. 2024.

[165] Vissers, M. R. et al. Proximity-coupled Ti/TiN multilayers for use in kinetic inductance detectors. *Applied Physics Letters*, 102(23):232603, Jun. 2013.

[166] Jones, G. et al. High quality factor manganese-doped aluminum lumped-element kinetic inductance detectors sensitive to frequencies below 100 GHz. *Applied Physics Letters*, 110(22):222601, May 2017.

[167] Lisovenko, M. et al. Characterization of the superconducting microwave properties of aluminum manganese. *Journal of Low Temperature Physics*, 209(5-6), Sep. 2022.

[168] Shirokoff, E. et al. MKID development for SuperSpec: an on-chip, mm-wave, filter-bank spectrometer. In Wayne S. Holland, editor, *Millimeter, Submillimeter, and Far-Infrared Detectors and Instrumentation for Astronomy VI*, volume 8452, page 84520R. International Society for Optics and Photonics, SPIE, 2012.

[169] Hailey-Dunsheath, S. et al. Kinetic inductance detectors for the Origins Space Telescope. *Journal of Astronomical Telescopes, Instruments, and Systems*, 7(1):1 – 17, 2021.

[170] OJEU — The Official Journal Of the European Union. UK Simons Observatory (SO:UK) Consortium - Sm — ojeu.com. https://ojeu.com/ojdblnk/view-notice.php?id=3403475, 2024.